DIFFRACTION STUDIES OF CUBIC STABILISED

ZIRCONIA CONSIDERED

AS A GLASS

Yu Chen

A thesis submitted for the Degree of Doctor of Philosophy in Monash
University

Monash University, Clayton, Victoria 3168, Australia

June, 1999

DEDICATION

For

My Parents

ACKNOWLEDGEMENTS

STATEMENT OF ORIGINALITY

This thesis contains no material which has been previously accepted for the award of any other degree or diploma in any university or institute, and, to the best of my knowledge contains no material previously published or written by any other person, except where due reference is made in the text of the thesis.

Yu Chen
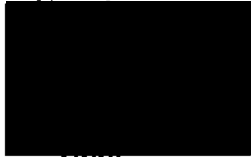
June, 1999

ABSTRACT

Cubic stabilized zirconia (CSZ) is a material with many diverse technological applications due to its high oxygen ion transport property at elevated temperatures. A great deal of study has gone into understanding the structure/function mechanism in CSZ, but many discrepancies and misunderstandings remain. In this thesis, the microstructure of CSZ has been investigated from a viewpoint of the orientational glass.

CSZ was treated as an orientational glass (OG) with reorientable quadrupoles consisting of microdomains embedded in an elastic matrix. In many ways, it exhibits the properties of structural glasses, as most orientational glasses do.

XRD studies on 12 mole % Y-CSZ revealed that 220 and 111 reflection peaks are broadened at temperatures below 650°C, and that reflection peaks under Mo radiation are split into doublets or triplets at temperature below 1000°C. The results can be explained very well using the microdomain-orientational glass model. The microdomains in Y-CSZ are conceived with probable structures of β or γ phases like those in Sc-CSZ. Cation ordering in those microdomains accounts for the splitting of the reflection peaks under Mo radiation.

Electron diffraction studies have been conducted in concentration series and temperature series on single-crystal, ion-beam thinned samples of Y-CSZ . The diffuse scattering features of the "bow-ties", "mushrooms" and "smoke-rings" were attributed to the microdomains from our concentration series (9.5 to 24 mole% Y_2O_3). The "cross-shaped" diffuse scatter was shown to arise from the antiferroelastic pairing of the reorientable elastic defects on $\{100\}$ planes. Probably the most important result is that an increase in dopant causes a decrease in the brightness of the "forbidden" $1\bar{1}2$ -type tetragonal diffuse spots. This suggests that they arise from the distorted cubic material between the domains, with the superposed stresses from the adjacent domains (considered as reconstructively reorientable defects) imparting a net local tetragonal distortion to the cubic matrix at low temperature, with small regions of $\langle 1\bar{1}2 \rangle$ –oriented planes diffracting randomly and independently, resulting in no net distortion overall.

Limiting our experiments to one concentration value, considered to reside solely in the "equilibrium" cubic phase (12 mole % Y_2O_3), we demonstrated that above about 1000°C, the $11\bar{2}$ spots vanish, indicating the arrest of the cubic region by the microdomains has ceased, with a low value for the Edwards-Anderson order parameter for the reorientable defects (domains).

Neutron diffraction data recorded from various reflecting positions in reciprocal space as a function of temperature showed that the diffuse scattering originated from microdomains or "defect aggregates". One set of neutron diffraction data recorded in the present series was internally consistent with the mode-coupling hypothesis that the reorientable rotating species (microdomains) undergo a phase transition near our proposed Leutheusser temperature T_L of ~650°C, which triggers a partial structure arrest of the tetragonally distorted cubic matrix material.

The structural arrest above, signalled by the "square-root" cusp behavior of the quasi-elastic intensity near 1.2,1.2,1.8 is symptomatic of non-ergodicity in the material, which ultimately causes the arrest of the mobile "single (oxygen) vacancy" defect as signalled by the similarity of the corresponding diffraction behavior at 1.6,1.6,1.0 to that of the cubic matrix. As the temperature falls toward T_g, the correlation length grows and the arrest becomes stronger. This scenario appears to support our suggestion that the data furnishes consistent, independent evidence for a glassy on-off ion conductivity mechanism in stabilized zirconia.

TABLE OF CONTENTS

CHAPTER 1

INTRODUCTION

Pure bulk zirconia (ZrO_2) possesses three polymorphs at ordinary pressures— monoclinic, tetragonal and cubic. The cubic variety is stable from~2370°C to the melting point at ~ 2680°C. When cooled to room temperature, pure zirconia is shattered to powder by the tetragonal-to-monoclinic phase transformation, which involves a large volume change and which makes zirconia unsuitable as a structural engineering material. Stabilized zirconia, however, can be retained metastably for long periods in the high-temperature cubic phase at room temperature by addition of approximately 15 (cation) mole % of the oxide of several metals with valency lower than four. Those include CaO, MgO, Y_2O_3 and all the rare-earth oxides.

Cubic stabilized zirconia (CSZ) is a well-known ceramic structural engineering material with widespread use as a high-temperature solid electrolyte with applications in the sensor or fuel cell fields. Because of its commercial importance, a great deal of study has gone into understanding the structure/function mechanism in CSZ, but many discrepancies and misunderstandings remain. Many contradictions arise between the various published studies of its mechanical and transport properties and reports persist of subtle irreproducibilities during individual investigations. Some idea of the present state of confusion regarding CSZ is conveyed in the review by Yashima et al. (1996). An attempt is made in this thesis to link the microstructure of CSZ with its engineering performance, but only recently has some agreement begun to appear on what the microstructure actually is. A survey of structural investigations undertaken into CSZ (stabilized by various dopants) using X-rays, neutrons and electrons reveals widely differing opinions and these are canvassed in the literature review (chapter 2).

In essence, the aim of this thesis is to show that cubic stabilized zirconia may be considered structurally to be an orientational glass, which is the elastic analogue of a magnetic spin glass, and , by extension, that it displays many of the familiar properties of ordinary structural glasses, even though CSZ does not appear amorphous at first sight. The point here is that crystallographically CSZ may be cubic on average, but that ordering of cation and/or oxygen vacancies produces a random array of interacting elastic defects on a mesoscopic scale (i.e., on a scale of tens of Ångstroms) with

emergent glassy properties. This thesis represents an attempt to interpret theoretically the existing data on CSZ and use the results of several recently published papers on orientational glasses to guide and interpret further diffraction experiments conducted using electrons, X-rays and neutrons.

Each of these techniques delivers slightly different diffraction information on the material. Of the commercially available zirconias, the predicted critical behavior occurs in CSZ at accessible temperatures if the dopant is yttrium sesquioxide (Y_2O_3). Electron diffraction, however, will not differentiate between Zr and Y on the cation lattice because of the similarity of their electron scattering factors, but symmetry breaking due to the ordering of the associated oxygen ion vacancies is sensitively detected (chapter 5). X-ray diffraction from powder samples will not detect any difference between Y and Zr atoms using Cu radiation, but strong contrast becomes available if a molybdenum (Mo) X-ray target is used since the anomalous absorption which results allows differentiation of the Y and Zr ions (chapter 6). Oxygen ions have a low scattering cross-section for X-rays and electrons, but are a large fraction of the scatter for neutrons; about 70% of that for Y and Zr, which are of similar strength (chapter 7). Hence some insight is afforded into the oxygen lattice as well as that of the metal ions, but the diffraction phenomena are complicated, principally because the microstructure of CSZ is also complicated, as the structure background reported in chapter 2 suggests.

What is novel about the experiments undertaken in this thesis is that most of the different diffraction patterns reported are part of a concentration series, usually with Y_2O_3 molar concentrations of 9.6%, 12%, 15%, 18% and 24% in order to detect trends among the patterns with increase in dopant and that many of the patterns are also part of a temperature series, with patterns recorded at relatively closely-spaced intervals in temperature, in the region where the critical phenomena are predicted to occur. For yttria-doped zirconia, a consistent set of diffraction effects was obtained at the temperatures required by the theory. We concluded that appearance of the diffraction patterns at the predicted temperatures is evidence for a "glassy sequence" of phase transformations and that these events are what control the conductivity of oxygen ions through CSZ considered as an electrolyte.

As chapter 2 demonstrates, all the phase diagrams and diffraction patterns of the variously doped zirconias are rather similar, and should be attributable to the same

physical phenomena. This indicates that much of the confusion in the literature arises from the onset of these hitherto-unrecognized transitions in CSZ and to glassy irreversibility.

Although the temperature of the predicted sequence of transitions found in yttria-doped zirconia turns out to be accessible in an electron-microscope heating stage, modern thermodynamics has little to say about the prediction of absolute values of temperature for spin-glass-like theories. The differing glass temperatures T_g for zirconia alloys with different dopants, therefore, has only served to add to the confusion. To say that a stabilized zirconia glassy "melt" gradually freezes into a rigid glass over some range of temperature between about 900°C and 400°C appears to contradict the idea of a melting point for pure zirconia of about 2680°C and that for the stabilized alloys only a few hundred degrees lower. What is meant here, of course, is that a certain part of the CSZ microstructure freezes and melts at various temperatures, at least enough to permit conductivity of oxygen ions by a vacancy process. In chapter 3 the theory is developed which predicts the sequence of events to be expected in such a glassy ion conduction process and a relationship suggested between the temperatures of this sequence . Familiar non-diffraction experiments suggesting that CSZ is a glass are reported in chapter 4. The experimental work reported in this thesis is interpreted in terms of the results of two modern theories of the glass transition and these are outlined in chapter 3. One is a static equilibrium transition, which is used chiefly to interpret the appearance of certain "forbidden" spots in electron diffraction patterns. These patterns are displayed at the end of chapter 5. The other is a dynamical theory in which a sudden qualitative change in the transport properties of a glassy material is detected at a temperature well above that of the familiar calorimetric glass transition T_g, due to the arrest of certain density fluctuations in the conducting "liquid" portion of the microstructure. The central analytical quantity calculated in this density-fluctuation mode-coupling theory (MCT) is a reciprocal (Fourier) space correlation function $F(k,t)$ which is a measure of the correlation between the instantaneous value of the kth Fourier component of the microscopic density and its initial value. The long-time value for this correlation function is proportional to the Edwards-Anderson (EA) order parameter, whose non-zero value signals a spin-glass-type state. In glassy materials below the transition temperature the EA order parameter appears as a kind of static Debye-Waller function

which grows with fall in temperature. Its characteristic insensitivity to wavenumber in the mode-coupling regime is displayed experimentally in chapter 6, where a simple calculation is carried out to compare its experimental behaviour with that expected if the effective Debye-Waller factor were due solely to thermal vibrations. The neutron diffraction results given in chapter 7, where diffraction effects from differing microstructural features are identified and correlated with the sequence of events to be expected in a real glass, not merely a spin glass analogue. Throughout the experimental chapters and (especially) in chapter 5 where the most relevant results of the applicable new theories are presented, reference is often made to more-or-less ordered crystalline regions a few tens of Ångstroms across which Allpress and Rossell (1975) originally called microdomains, coherently intergrown with the f.c.c. lattice. They will also be referred to interchangeably in the thesis as "interacting mesoscopic rotors" or "reorientable elastic defects".

Notationally, Y-CSZ and YSZ mean the same thing and (e.g.) YSZ-12 means cubic zirconia stabilized by the addition of 12 mole % Y_2O_3. Throughout the thesis the words "low" or "lower" temperature will mean a temperature range below some phase transformation, rather than ultra-low temperature.

LITERATURE REVIEW OF DIFFRACTION STUDIES IN ZIRCONIA

2.1   Zirconia Polymorphs, Stabilization, and Phase Transformation

Pure zirconia, ZrO_2, has three temperature dependent polymorphs cubic c, tetragonal t, and monoclinic m.

The cubic phase assumes the fluorite structure and is stable from 2370°C to the melting point, ~ 2680 °C (Carter and Roth, 1968). In this structure (space group Fm3m, see Fig.2.1) each cation is in eight-fold coordination with the anions, while the anions are in four-fold coordination with cations. The structure can be thought to be made up of cubes where the anion is located at the corners of each cube and the cation occupies the centre of alternate cubes.

Cubic
Fm 3m

O
Zr
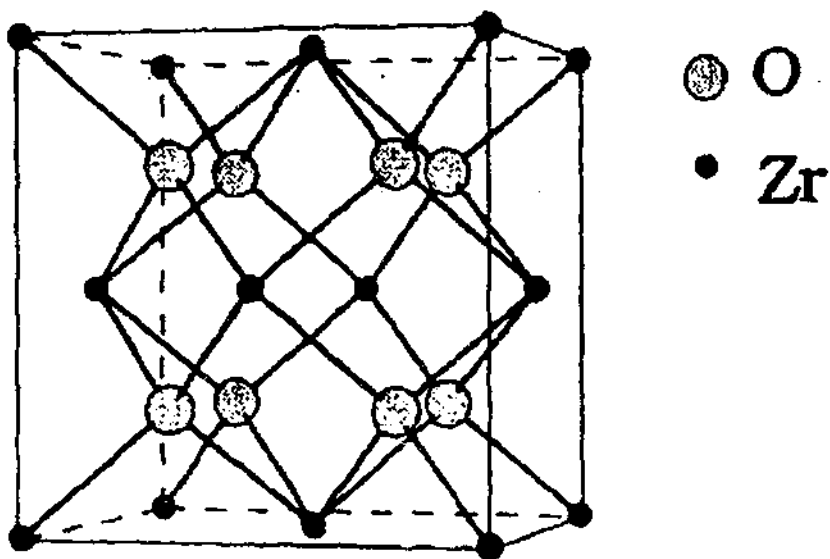
Fig. 2.1.   The cubic zirconia fluorite structure.

The tetragonal form of pure ZrO_2 is stable between 1170°C and 2370°C. Teufer (1962) indexed the high temperature XRD pattern of the tetragonal form on a body

centred tetragonal cell with space group $P4_2/nmc$. However it has been convenient to also index the t zirconia on a face-centred tetragonal (fct) cell (see Fig.2.2). This allows comparison between the face-centred cubic fluorite structure and the tetragonal form of zirconia. The t-phase is related to the fluorite structure by a tetragonal distortion of the oxygen sublattice. This distortion takes the form of slight displacements of alternate rows of O-atoms along $\langle 001 \rangle$. This displacement produces a rumpling effect as compared to the fluorite lattice, producing two sets of Zr-O bonds (Howard et al., 1988). As a result of this distortion the O-atom occupies the *2mm* site, with one variable positional parameter z (the Zr-atom is fixed in relation to the c structure). The displacement is a shear-type displacement with a 110 shear plane. Negita (1989) reported that the cubic to tetragonal transition is of ferroelastic type.

Tetragonal
$P\,4_2/nmc$
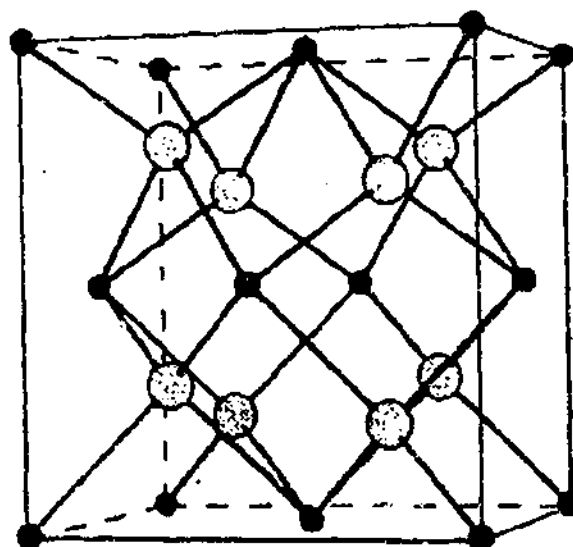
Fig. 2.2 Tetragonal Zirconia structure, shown here on the f.c.t. cell for comparison with the c-ZrO_2 structure (Fig. 2.1). The f. c. t. cell is related to the b.c.t. cell by a 45° rotation of the a-axis, about the c-axis.

The monoclinic form of ZrO_2 (space group $P2_1/c$) exists below 1170°C. In the monoclinic structure (see Fig. 2.3a) the Zr-O distances range from 2.05 to 2.28Å, putting the Zr in a seven-fold coordination as opposed to an eight fold coordination in the c- and t- structures (Smith and Newkirk, 1965). The next nearest oxygen gives a Zr-O bond-length of 3.58 Å and it can not be considered in the coordination sphere of

the Zr atom. Fig. 2.3b shows the ZrO_7 polyhedron. It can be seen that Zr-atom is in a four-fold coordination with the O2 oxygen atoms while in a three fold coordination with O1 oxygen atoms. The average Zr-O1and Zr-O2 distances are 0.207 nm and 0.221 nm respectively (Smith and Newkirk, 1965). The transformation of tetragonal to monoclinic zirconia is believed to be martensitic in nature. Crystallographically, the lattice correspondence which occurs between t- and m-ZrO_2 is for the c axis of t-ZrO_2 to be parallel to the c axis of m-ZrO_2. For pure zirconia the non-vanishing components of the symmetrical unconstrained transformation strain tensors, e^T, defined with respect to the tetragonal lattice are (Rühle et al., 1984):

$$e_{11}^T = \frac{a_m}{a_t}\cos\beta - 1 = -0.00149$$

$$e_{22}^T = \frac{b_m}{b_t} - 1 = 0.02442$$

$$e_{33}^T = \frac{c_m}{c_t} - 1 = 0.02386$$

$$e_{13}^T = e_{31}^T = \tan\beta = 0.08188$$

The data clearly show that the shear component is the dominant term in the strain tensors, and that the volume increase at room temperature from t-phase to m-phase is about 4.7%. It is well established that high temperature c- and t-phases of ZrO_2 can be stabilized to room temperature by the incorporation of trivalent or divalent oxides (CaO, Sc_2O_3, Y_2O_3, etc.). For divalent oxides, the minimum dopant amount to stabilize cubic structure to room temperature is variable, depending on the sample preparation and the thermal history. A reported lower boundary of single cubic phase region in thr ZrO_2 - CaO phase diagram at 1325°C is 15 mole% (Hellmann and Stubican, 1983). For trivalent oxides, the most commonly reported minimum dopant amount to stabilize cubic structure to room temperature is about 8 mole % (Scott, 1975; Ruh et al., 1977, 1984).
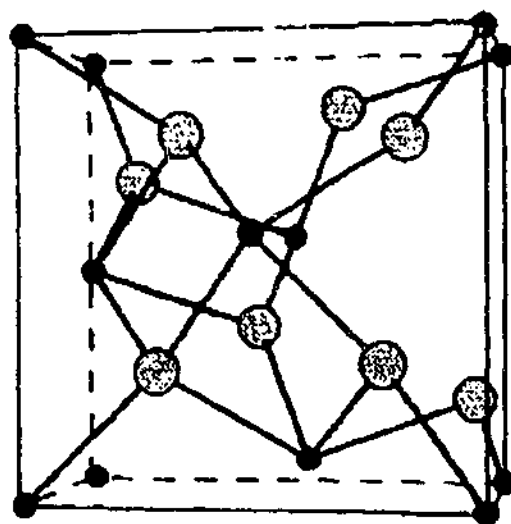
Monoclinic
$P2_1/c$

Fig.2.3. a) the monoclinic Zirconia structure, shown here on a face centred cell, for comparison with the c-ZrO_2 structure (Fig.2.1), b) the ZrO_7 group as it occurs in the monoclinic structure. Note the 3-fold coordination of Zr with the O1 oxygen atoms and the 4-fold coordination with the O2 oxygen atoms.

The nature of stabilization in the c-phase is still uncertain. As is well known, Pauling (1960) provided a set of semiempirical "rules" based on radius ratio r_{cation}/r_{anion} considerations for predicting crystal structures of inorganic materials. For AX_2 compounds, those solids with large cations and radius ratios approaching 1 should have the fluorite structure, whereas those with small cations and radius ratios <0.4 should have tetrahedral coordination and crystallize with one of the silica structures; intermediate-sized cations should form AX_2 compounds with the rutile structure. Although exceptions are known, Pauling's rules do derive from fundamental aspects of chemical bonding and are widely applicable. For ZrO_2, however, the compilation of Shannon and Prewitt (1969) shows that the radius ratio for ZrO_2 in eight-fold coordination is 0.59, much lower than for other stable oxides and fluorides with the fluorite structure (CeO_2 0.68, UO_2 0.70, ThO_2 0.75, CaF_2 0.84, etc.) but larger than for compounds with the rutile structure. (In sixfold coordination, ZrO_2 would have a radius ratio of 0.51, compared with that for TiO_2 itself of 0.43.) Pauling's "rules" predicted the instability of c-form of pure ZrO_2. Based on Pauling's "rules", Etsell and Flengas (1970) proposed that dopant cations with radii larger than that of Zr^{4+} will

increase the average cation radii so such dopant cations should be considered effective to stabilize the c-form of ZrO_2. However, stabilisation of c-ZrO_2 with scandia does not follow this argument strictly since the radius of Sc^{3+} in eight-fold coordination is very close to that of Zr^{4+}.

The incorporation of aliovalent oxides into the lattice inevitably introduces oxygen vacancies to maintain charge balance, which can range in concentration from ~4% to ~10% depending on the concentration and valence of the dopant cation. Ruh and Garrett (1967) reported that when ZrO_2 is heated in reducing environments and loses oxygen, the c-phase in the resulting nonstoichiometric ZrO_{2-x} has a larger stability field. It was assumed that the alloying effect on the stabilization of c-forms depends primarily on the number of oxygen vacancies and is independent of what has caused the vacancies (Hillert, 1991). Heuer and Rühle (1984) attributed the stabilization of c-ZrO_2 by oxygen vacancies in doped or oxygen-deficient ZrO_2 to the formation of stronger covalent bonds by local structural relaxation around oxygen vacancies. It is well recognized that the c-forms of doped ZrO_2 are metastable at lower temperature and likely a stabilization by kinetics rather than by thermodynamics beomes possible (Yashima et al., 1996). It seems to us that vacancies alone are not able to offer the kinetic stabilizing effect since they are highly mobile. It is the dopant cations that delivered the kinetic stabilization owing to their extremely slow diffusion in the lattice at lower temperatures. The effect of different radii of host cation and dopant cation on the stabilization of c-ZrO_2 will be brought into discussion later in this thesis.

Phase diagrams of zirconia systems have been investigated extensively by numerous researchers, however; there are many contradictions and discrepancies. In addition to those contradictions and discrepancies, there existed common misunderstandings on the metastable phase boundaries. Yashima et al. (1996) reported that the variety of metastable states accounts for all the contradictions and discrepancies , and that the sluggish kinetics, mainly slow diffusion of cations, and diffusionless phase transformation are the two major factors to lead to difficulties in the study of the zirconia systems and the intricacy of metastable phases. There are two kinds of phase transformations recognized in zirconia-containing systems; one is diffusional transformation and the other is the cation-diffusionless transformation according to

Yashima et al. (1996). The former is applicable to precipitation of t-phase, precipitation of intermediate- or ordered-phases, such as $CaZr_4O_9$ (ϕ_1), $Zr_3Y_4O_{12}$ (δ), and the eutectoid decomposition. The latter is mainly applicable to the occurrence of "non-transformable" tetragonal phases, t' (Heuer and Rühle, 1984). In cation-diffusionless transformation, the parent and the transformed phases have the same composition (dopant concentration). A good example demonstrating the contradictions and discrepancies occurring in zirconia-containing system is the controversial phase which was labelled the t''-phase, tetragonal without tetragonality, by Yashima et al. (1993).

2.2 Long-Range Order: The Fluorite-Related Superstructures in Stabilised Zirconia Alloys

Superstructure phases of narrow homogeneity range often appear at relatively low temperatures within a defect fluorite phase field. Large numbers of these are known in many systems, and there are many structural forms. Superstructure phases are particularly numerous in the systems PrO_{2-x}, TbO_{2-x}, CeO_{2-x}, and their conformity to the "homologous series" formula M_nO_{2n-2} is clearly demonstrated (Rossell, 1984).

Like other fluorite-related systems, zirconia-containing systems exhibit long-range ordered phases, e.g., $CaZr_4O_9$ (Allpress et al., 1975), $Zr_3Sc_4O_{12}$, $Zr_5Sc_2O_{13}$ (Thornber et al., 1968) $Zr_3Y_4O_{12}$ (Scott, 1977). The ordering processes in defect fluorite zirconia alloys have been believed to be the cause of the deterioration of the ionic conductivity with time (Tien et al., 1963; Carter and Roth, 1968).

As mentioned before, most of the ordering processes are involved with slow cation diffusion. The sizes of dopant cations play a decisive role in the ordering process. Yttria and Scandia are both trivalent oxides, and the radius of Sc^{3+} in eightfold coordination is 0.095nm, while the radius of Y^{3+} is 0.110nm (Shannon and Prewitt, 1969). Later in the survey it will be disclosed that ordering processes in the Sc_2O_3-ZrO_2 system are much quicker and there are more ordered phases in the Sc_2O_3-ZrO_2 system in comparison with the Y_2O_3-ZrO_2 system. Calcia is a divalent oxide and the radius of Ca^{2+} in eightfold coordination is 0.12nm. The ordering process in CaO-ZrO_2

has long been an interest to many researchers (Tien et al., 1963; Carter and Roth, 1968; Allpress and Rossell, 1975; Rossell et al., 1991). To set the stage for later discussion, ordered phases reported in CaO-ZrO$_2$, Sc$_2$O$_3$-ZrO$_2$, Y$_2$O$_3$-ZrO$_2$ systems are reviewed next.

2.2.1 The CaO-ZrO$_2$ System

In the ZrO$_2$-rich region (ZrO$_2$ mole percentage more than 50%), there are two fluorite-related superstructure phases CaZr$_4$O$_9$ (ϕ_1) and Ca$_6$Zr$_{19}$O$_{44}$ (ϕ_2) known to exist in this system (Michel, 1973; Hudson and Moseley, 1976; Duran et al., 1987; Hellman and Stubican, 1984). It is believed that they have the same structures as those of CaHf$_4$O$_9$ and Ca$_6$Hf$_{19}$O$_{44}$ (Allpress, Rossell and Scott, 1975). ϕ_1 is monoclinic, space group C2/c, z = 16, and ϕ_2 is rhombohedral, space group R $\bar{3}$c, z =2 (Allpress, Rossell, and Scott, 1975). Marxreiter et al. (1990) and Lin and Sellar (1994) reported the lattice parameters of CaZr$_4$O$_9$: a = 1.7793(7)nm, b = 1.4557(7)nm, c = 1.2072(5)nm and β = 119.42(3)°, which are slightly different from those reported by Duran et al.(1987) and Hellmann et al. (1983) in "a" value. The lattice parameters of Ca$_6$Zr$_{19}$O$_{44}$ have been reported by Duran et al.(1987) to be a_H = 1.8274nm and c_H = 1.7742nm.

The relations between the fluorite structure and the ordered phases are (Allpress, Rossell, and Scott, 1975),

for ϕ_1:

$$a = [222]_f, \; b = [\bar{2}20]_f, \; c = \frac{1}{2}[\bar{3}\bar{3}2]_f$$

for ϕ_2:

$$u = \frac{1}{2}[\bar{2}33]_f, \; v = \frac{1}{2}[3\bar{2}3]_f, \; w = \frac{1}{2}[33\bar{2}]_f \; \text{(Rhombohedral cell)}.$$

In both ϕ_1 and ϕ_2 phases, oxygen vacancies appear to be a $\frac{1}{2}\langle 111 \rangle_f$ pair, with a cation in the middle. These pairs form finite groups in ϕ_1, four vacancies separated by three different $\frac{1}{2}\langle 111 \rangle_f$ vectors, and the vacancy groups are not chained together. In ϕ_2, the

oxygen pairs form helical chains in which vacancies and the hafnium ions alternate along the chain (Allpress, Rossell, and Scott, 1975). Cations in ϕ_2 are completely ordered in such a way that calcium ions form helical chains which extend along the hexagonal c axis and successive ions are related by $\frac{1}{2}\langle 110 \rangle_f$ vectors, and that all the calcium ions (the larger cation) have the eightfold coordination of the ideal fluorite structure, while hafnium ions are six-, seven-, or eightfold coordinated. Cations in ϕ_1 are less ordered than those in ϕ_2 in such a way that calcium ions occur in chains, with neighbours separated by $\frac{1}{2}\langle 110 \rangle_f$ vectors, but the chains have a much more irregular structure than those in ϕ_2 in that they change direction more frequently and tend to "wander" through the structure (Allpress, Rossell, and Scott, 1975). Oxygen vacancies in both ϕ_1 and ϕ_2 are not the next neighbour of calcium ions, according to Allpress, Rossell, and Scott (1975).

Hellmann and Stubican (1983) determined the upper limits of stability for ϕ_1 and ϕ_2 to be 1235± 15°C and 1355± 15°C, respectively. Duran et al. (1987) reported that the two ordered phases ϕ_1 and ϕ_2 are unstable below 1100°C, but they can persist metastably at lower temperatures. A ZrO_2-CaO phase diagram of Duran et al. (1987) is presented in Fig.2.4 for reference. Duran et al. (1987) synthesized the ordered phases in the ZrO_2-CaO using two different methods. Method one was to anneal quenched samples with the correct composition (20 mole % CaO for ϕ_1 and 24 mole % CaO for ϕ_2 soaked eight hours at 1780°C) for a long time between 950° and 1400°C. Method two was to anneal reactive powder mixtures with the right compositions for a long time in the same temperature range as in method one. They found that ordered phases were formed much faster or at lower temperatures from the reactive powder mixtures than from the quenched samples during annealing processes. They concluded that the ordering of the cations is probably required in the process of ordering.

Although both ordered phases ϕ_1 and ϕ_2 will only be formed by long time annealing at right temperatures, ϕ_1 is less difficult to prepare than ϕ_2 (Stubican and Ray, 1977). This may be related to the high degree of cation-ordering in ϕ_2 (Hellman and Stubican, 1983).
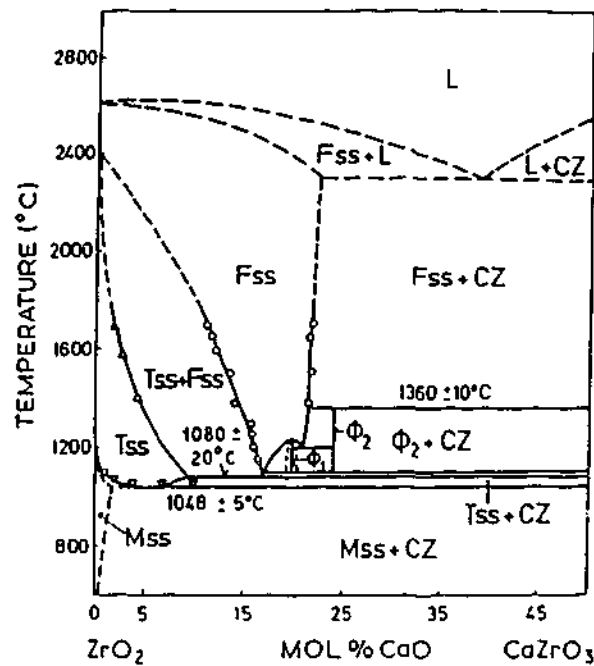
Fig. 2.4. Phase equilibrium diagram for the ZrO_2 -rich region of the system ZrO_2 - CaO, after Duran et al. (1987).

Discrepancies exist regarding the homogeneity, and the decomposition of ϕ_1 phase. Hellmann and Stubican (1983) reported that is a line phase in the phase diagram and peritectoidally decomposes to fluorite solid solution and a ϕ_2 compound above $1235\pm 15°C$. Duran et al. (1987) suggested that ϕ_1 could not be a line phase in the system, and that a very small homogeneity range must exist for this phase.

Reportedly ϕ_1 has a homogeneity region around 20 mole % CaO; it can appear in a ZrO_2-CaO sample with much lower calcium content by nucleation, and microdomain formation (Rossell, 1984; Rossell et al., 1991).

2.2.2 ZrO_2 - Sc_2O_3 System

Three ordered phases β, γ, and δ have been reported to exist in the ZrO_2 rich region of Sc_2O_3-ZrO_2 System (Lefevre, 1963; Spiridonov et al., 1970; Thornber et al., 1970). They are all rhombohedral with lattice parameters $a=5.085$Å, $\alpha=88°48'$ for β- phase, $a=5.068$Å, $\alpha=90°19'$ for γ- phase $a=7.949$Å, $\alpha=72°33'$ for δ- phase (Lefevre, 1963).

2-9

Spiridonov et al. (1970) studied the system in the region 0 to 40 mol% Sc_2O_3 using high-temperature X-ray diffraction (XRD), dilatometry, differential thermal analysis (DTA), and electrical conductivity measurements. Their results revealed the rhombohedral $Sc_2Zr_7O_{17}$ phase (β) in the region 11 to 13% Sc_2O_3, the rhombohedral $Sc_2Zr_5O_{13}$ phase (γ) from 16 to 21% Sc_2O_3, and the rhombohedral $Sc_4Zr_3O_{12}$ phase (δ) from 30 to 40% Sc_2O_3. Ruh et al. (1977) reported similar results to those of Spiridonov et al. (1970) but slightly different in stating that the ordered phases have wider single phase regions, 9 to 13% Sc_2O_3 for β-phase, 15 to 23% Sc_2O_3 for γ-phase, and 24 to 40% Sc_2O_3 for δ-phase. A phase diagram of ZrO_2 - Sc_2O_3 proposed by Ruh et al. (1977) is shown in Fig. 2.5.

The β-phase transfers to cubic at 600°C, the γ-phase transfers to cubic at 1100°C, and the δ-phase exhibits no transformation. X-ray diffraction features peak separations when the disordered cubic phase undergoes a transition to the ordered phases of β, γ (Lefevre, 1963).
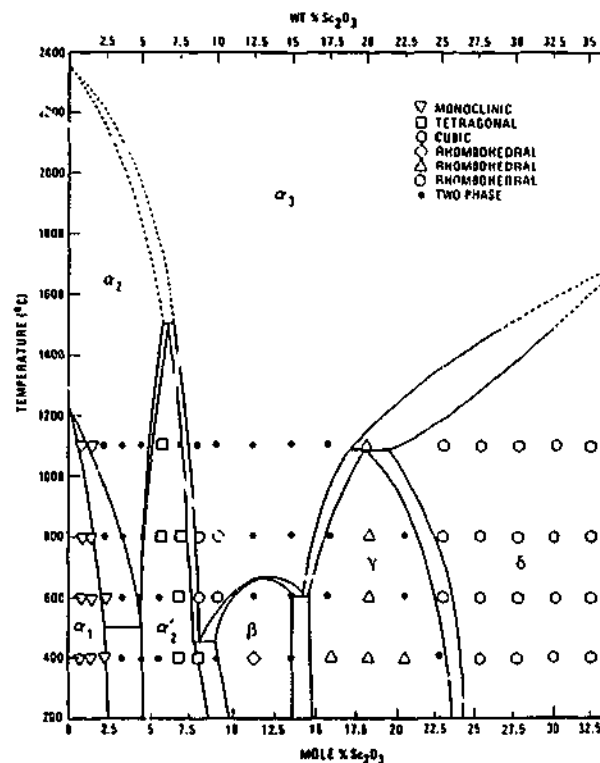
Fig. 2.5. Phase equilibrium diagram for the system ZrO_2 - Sc_2O_3 . After Ruh et al. (1977).

Using samples prepared by the coprecipitation of the hydrated oxides and heat treatment at 1600°C, Thornber et al. (1970) observed β, γ, and δ as line phases. By

2-10

contrast, these phases existed as monophase over composition ranges when they were prepared by arc-melting techniques. They proposed that the latter states may be metastable.

Thornber, Bevan and Graham (1968) determined the structures of γ-phase ($Sc_2Zr_5O_{13}$) and δ-phase ($Sc_4Zr_3O_{12}$) with a Hagg-Guinier focusing X-ray powder camera and Cu $K\alpha_1$ radiation. The space group in both cases is $R\bar{3}$, and the lattice parameters of γ-phase and δ-phase in hexagonal representation are a=9.53(2)Å, c= 17.44(2) Å and a=9.37(8) Å, c=8.71(0) Å, respectively. It is noted that the c-value of δ phase reported by Thornber et al. (1968) is half of that reported by Lefevre (1963). Both these structures are derived from the fluorite-type parent MO_2 by ordered omission of oxygen atoms. The observed rhombohedral distortion is the result of lattice relaxation. Fig. 2.6 shows the structural relationship among fluorite, γ and δ.

Both are rhombohedral distortions of the fluorite lattice, one of the four [111] directions becoming the unique inversion triad axis. Relative to the MO_2 composition of fluorite there are six oxygen positions in the hexagonal unit cell which are not occupied. These 'vacancies' are distributed two to each threefold axis so that the special metals lying on these are alternately 6- and 8- coordinated as shown in Fig.2.6. For the δ-phase these special metals are all 6-coordinated: no oxygen atoms occur in the threefold axis, so that the ideal structure has half the c dimension of the ideal γ-phase shown in Fig.2.6, and its ideal composition is M_7O_{12}. In the fluorite structure all oxygen positions in the threefold axis are occupied.

Phase transitions and the microstructure of the β-phase ($Sc_2Zr_7O_{17}$) were examined by Sakuma and Suto (1986). In the two ZrO_2-Sc_2O_3 alloys with scandia content of 10.5 and 12.5 mole %, the β-phase was found in both quenched and furnace-cooled samples. Their x-ray diffraction patterns of the samples showed a feature of peak-spliting for the 1 1 1, 2 2 0 and 3 1 1 reflections in the cubic fluorite structure. TEM examination on the microstructures of the samples with β-phase revealed a herring-bone appearance. They concluded that the transformation of fluorite solid solution to β is induced during cooling from the high-temperature cubic phase region by martensitic transformation, and that a herring-bone appearance is a characteristic microstructure developed by martensitic transformation.

They observed a higher upper limit temperature for the β-phase, which was 800°C, than both Ruh et al. (1977) and Spiridonov et al. (1970) did.

The detailed structure of the β-phase has not been reported. Incomplete structural stodies on the β-phase made by Thornber et al. (1970) suggests that it is related to fluorite structure by a disorder-order process in which one of the cubic [111] directions becomes unique, resulting in a complex rhombohedral supercell.

All three ordered phases β, γ and δ are formed by purely oxygen vacancy pair ordering. Because of the similar ionic radii of scandium and zirconium, ordering would only be expected on the basis of charge differences, and no evidence to suggest metal ordering was obtained (Thornber et al., 1968).
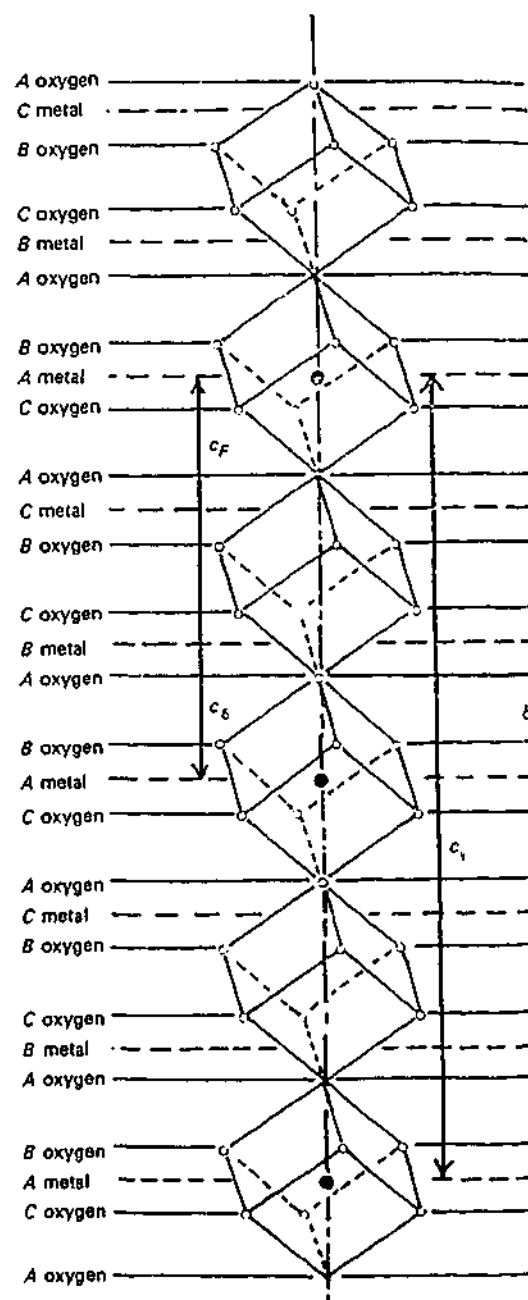
Fig. 2.6. The stacking sequence of metal and oxygen layers, and the atoms in the vicinity of a threefold rotation axis chosen to pass through A atom sites for the γ-phase, after Thornber et al. (1968). The c dimensions of the idealized γ-structure, fluorite and δ are also shown. In fluorite all oxygen sites in this axis are occupied; in δ all are vacant.

Comparing with other zirconia based systems, ZrO_2-Sc_2O_3 system has more ordered phases; it has comparatively fast ordering processes. All of these are attributed to the non-requirement of cation ordering, owing to similar radii of the host cation Zr^{4+} and dopant cation Sc^{3+}.

2.2.3 Y_2O_3-ZrO_2 System

In the zirconia-rich region of ZrO_2-Y_2O_3 system, only one fluorite-related ordered phase, $Zr_3Y_4O_{12}$ (δ), has been reported (Scott, 1977; Stubican et al., 1978; Pascual and Duran, 1983). A metastable rhombohedral phase developed in ZrO_2- 3.1 and 4.0 mole % Y_2O_3 alloys with microscopic features like those of the rhombohedral β-phase in ZrO_2-Sc_2O_3 was reported by Sakuma et al. (1985), but it was ignored by the other investigators. The structure of δ-phase has been determined by Thornber, Bevan and Graham (1968). It is rhombohedral, space group $R\,\overline{3}$. The structure of $Zr_3Y_4O_{12}$ was determined by Scott (1977) using X-ray powder diffraction technique. The lattice parameters reported are: $a = 0.97345(5)$ nm, $c = 0.91092(6)$ nm, $z = 3$ (hexagonal representation). Anion vacancies are ordered in $Zr_3Y_4O_{12}$ (δ), to give a rhombohedral cell. Cations are only partially ordered in $Zr_3Y_4O_{12}$ (δ) with Zr in the octahedrally coordinated cation sites and Zr + 2Y randomly in the sevenfold coordinated sites, in other words, the smaller cation Zr^{4+} coordinates anions and larger dopant cation Y^{3+} preferentially coordinates the vacancy pair. The conclusion of partial- ordering of cation and dopant cations in sevenfold coordination in $Zr_3Y_4O_{12}$ (δ), made by Scott is conflicting with what Allpress, Rossell & Scott (1975), Thornber, Bevan and Graham (1968) obtained from $Zr_3Yb_4O_{12}$ (δ), and $CaZr_4O_9$ in which they claimed that the

smaller Zr4+ cations tend to be six-, or sevenfold coordinated and the larger dopant cations, such as Yb, Ca, tend to be eightfold coordinated.

$Zr_3Y_4O_{12}$ (δ) can be prepared by solid-state reaction of the component oxides $3ZrO_2 + 2Y_2O_3$, at 1300°C for three months (Scott, 1977), or by annealing sintered or quenched samples at 1150°C more than three months (Pascual and Duran, 1983).

$Zr_3Y_4O_{12}$ (δ) is stable below 1382±5°C (Stubican 1988). The equilibrium phase diagram of ZrO_2 -Y_2O_3 , after Stubican (1988), is shown in Fig. 2.7.

Although no β-phase is reported in ZrO_2 -Y_2O_3 system, presence of the β-phase in HfO_2 -Y_2O_3 system (Duclot et al., 1970) suggests that it may exist in ZrO_2 -Y_2O_3, in a way either it is difficult to be detected or it is difficult to be prepared. It seems to us the former is most likely.
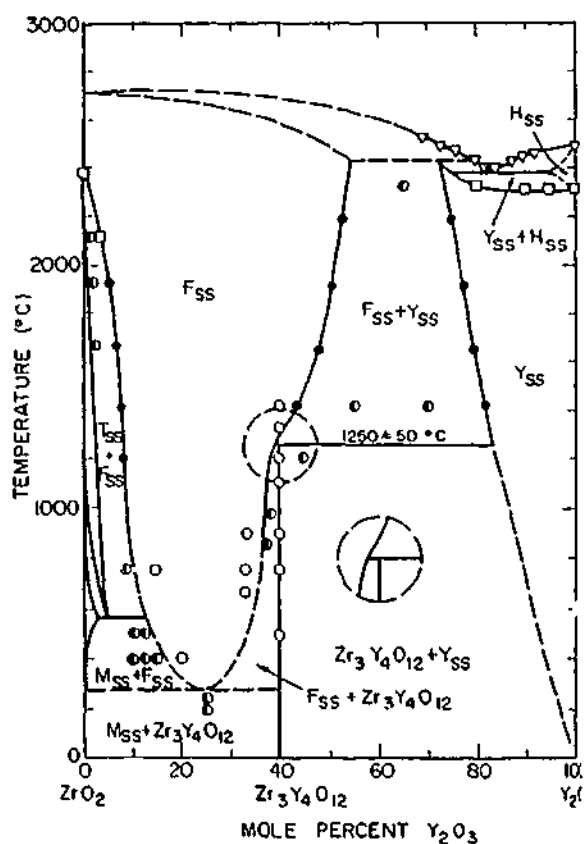
Fig. 2.7. Phase diagram for the system ZrO_2 -Y_2O_3 , after Stubican (1988).

To end the literature survey on ordered phases in Zirconia based systems, we summarize some important features of the ordering process in these systems in table 2.1. To assist a better understanding, systems involving Yb, Er, and Dy are included in the table. Attention is drawn to the number of ordered phases, the radii of the dopant cations, the requirements of cation ordering, and the kinetic process of ordering.

2-14

Table 2.1 shows that the ordering process in the ZrO_2-M_2O_3 (MO) is considerably influenced by the dopant cation size. For the same valency, the larger the dopant cation radius is, the slower the ordering process, and the fewer ordered phases. In the case of Dy^{3+}, the ordered phase can only be able to be nucleated without growth (Thornber, et al., 1970).

Table 2.1 Ordering Phases in ZrO_2 Rich Region of ZrO_2-M_2O_3(MO)

	Sc^{3+}	Yb^{3+}	Er^{3+}	Y^{3+}	Dy^{3+}	Ca^{2+}	Zr^{4+}
Radius in MO_8 (7) (nm)	0.087	0.098	0.100	0.102	0.103	0.112	0.084
Ordered phases reported	β (1) γ (2) δ (2), (3)	δ (3)	δ (3),	δ (4)	(3)	$\phi1$ (5) $\phi2$ (5)	
Cation ordering	Not found	Suggested	Zr on octahedral sites, 2Zr+4Er randomly in 7-coordinated sites (6)	Zr on octahedral sites, 2Zr+4Y randomly in 7-coordinated sites		complete order with Ca on sites of 8-fold coordination and Zr on sites of 6- and 7-fold coordination (6)	
Anion ordering	Suggested	Suggested	Suggested	Suggested		Suggested	
Disorder-Order transition	Fast	Sluggish	Sluggish	Very sluggish	Extremely sluggish	Very sluggish	

(1) Sakuma & Suto, 1986. (2) Thornber et al., 1968. (3) Thornber et al., 1970. (4) Scott, 1977. (5) Allpress, Rossell and Scott, 1975. (6) Rossell, 1984. (7) Shannon & Prewitt, 1970.

2.3　　　　　Defect Fluorite Structure

It has been widely accepted that doped c-ZrO_2 does not take a perfect fluorite structure, but structures with atoms displaced from their ideal fluorite positions (Heuer et al., 1984; Rossell, 1984). Also given the dopant cation concentration (in MO, M=divalent or $MO_{1.5}$, M=trivalent) around 12 to 40%, and vacancy concentrations in the range of 5 - 20%, interaction among the defects is inevitable. Probing into the defect structure of doped c-ZrO_2 has long been a great interest to many researchers worldwide because it may help to understand the ionic conductivity in this group of materials. X-ray, neutron, and electron scattering techniques are most commonly used for this purpose. The following literature survey will proceed alternately following these techniques.

2.3.1.   Electron Diffraction

Using electron diffraction technique, Allpress and Rossell (1975) probed the defect fluorite-type phases $Ca_xM_{1-x}O_{2-x}$(M = Zr, Hf; x = 0.1-0.2). They found that except for strong reflections characteristic of a fluorite-type subcell there were weak diffuse patterns, the arrangement of these diffuse maxima was relatively insensitive to variations in lime content in the range x = 0.1-0.2, and that it was not affected by the method of preparation (arc-melting, solar-melting, or sintering of the component oxides). It was also reported that the effect of annealing the samples for a short period at low temperatures (e.g., 1 week at 1000°C) was merely to sharpen the diffuse maxima to some extent. However when samples containing 20 mole % lime (x = 0.2) were annealed for relatively long period, 1000 hours in ZrO_2-20 mole % CaO case, the diffuse scattering maxima were replaced by complex arrays of sharp spots, and eventually the whole diffraction pattern was purely from the ordered structure of monoclinic phase ϕ_l when the samples were annealed a long time, 3600 hours in ZrO_2-20 mole % CaO case. By comparing the features in diffraction patterns of defect fluorite phases with those in patterns from annealed specimens, the authors suggested that the defect fluorite-type solid solutions contain domains of ordered phase ϕ_l embedded coherently in a number of specific orientations within the cubic matrix. The dopant concentration influences the population of the domains but not the size of the

domain and each domain is about 30 Å in diameter. Their calculations based on this model agree with the observed diffraction data.

How those microdomains are formed during a quench remains unknown if you consider that cation ordering occurs in the ϕ_l phase and that the diffusion coefficient of Ca in ZrO_2-CaO is very small. One speculation is that the microdomain structures could well exist (in a state of dynamic fluctuation) at high temperature (Rossell, 1984).

The same approach was used to study the diffuse patterns in ZrO_2-Y_2O_3 by Rossell (1984). Using the only superstructure phase reported in the ZrO_2-Y_2O_3 system, the author calculated the electron diffraction patterns for a material consisting of microdomains of $Zr_3Y_4O_{12}$ (δ) in all eight orientations coherent with a fluorite matrix. Unfortunately, the geometric proportions of the diffuse features did not match those of the observed patterns. Although β-phase was not reported in the system, the author believed that the β-phase may be of significance in this case.

Suzuki, Tanaka, and Ishigame (1985, 1987) studied the yttria doped zirconia by electron diffraction. The diffuse scattering patterns in 10, 20-30, and 40-50 mole % Y_2O_3-ZrO_2 alloys were interpreted in terms of the microdomains of the ordered structures. However, such microdomains were defined in terms of modulated oxygen-ion displacements in [001] directions. The modulation is expressed by a square transverse wave whose wavenumber vector $\underline{q} = \dfrac{\pi}{a_0}\langle 110 \rangle$, and with anti-phase boundaries parallel to {112} planes at intervals of five times the 112 spacings. These modulated structures result in micro-domains of several nm in diameter. No cation ordering is reported to cause the domain structures.

Following Suzuki, Tanaka, and Ishigame (1987), Miida et al. (1994) extended the APS model to one in which the antiphase boundaries consist of various planes belonging to the [111] zone axis so that a diffuse scattering intensity distribution in reciprocal space (shown in Fig.2.8. a) is formed and such a distribution can interpret the diffuse spot and diffuse circular patterns obtained from CaO- and $Tb_2O_{3.5}$ - stabilised zirconias (shown in Fig.2.8. b & c).
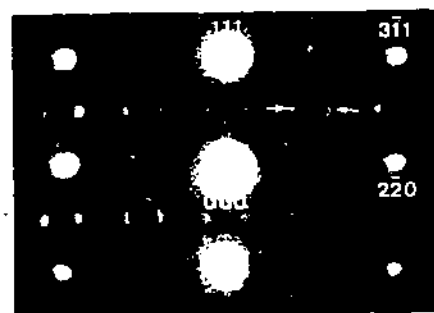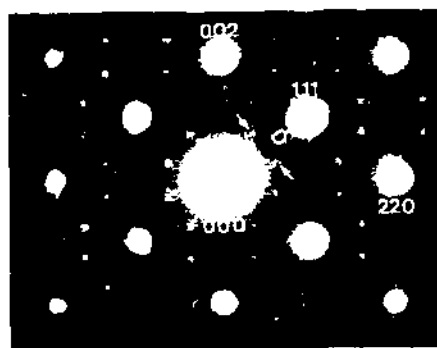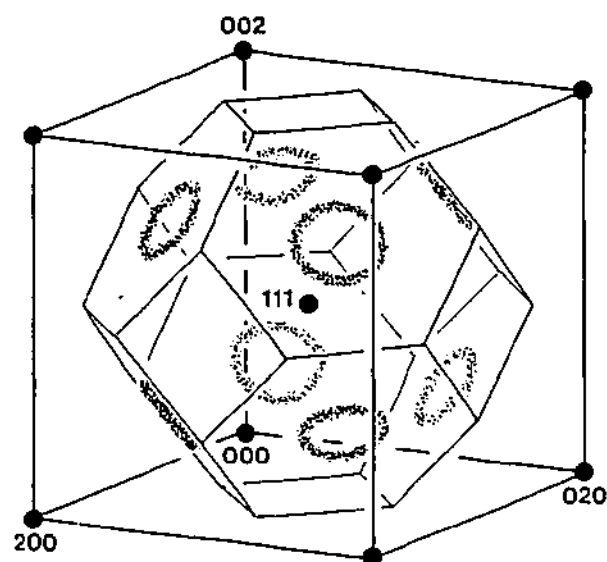
Fig. 2.8. a) Schematic intensity distribution in reciprocal space for the diffuse scattering. b), c) Diffuse spot and diffuse circular patterns obtained from CSZ containing 19 mole % CaO at [1$\bar{1}$0]and [1$\bar{1}$$\bar{2}$] zone axes, respectively. The letter D indicates the separation of the split spots. After Miida et al. (1994).

The split spots seen in Fig. 2.8 (b) and (c) were interpreted as a result of the right-angle intersection of the Ewald sphere with the circular diffuse contour, and the diffuse circle with two intensity maxima around $\frac{3}{2}, \frac{\bar{1}}{2}, \frac{1}{2}$ as a result of a skew ($\sim$ 18.5°) intersection of the Ewald sphere with the circular diffuse contour.

Recently, Dai et al. (1996a) proposed a diffuse scattering distribution model in reciprocal space which is similar to the one suggested by Miida et al.(1994). Local ordering (short-range ordering) was believed to the cause for the diffuse scattering. The calculated correlation length of oxygen vacancy ordering was approximately 0.82

nm, and oxygen vacancies were suggested to be linked by position vectors $r_{(200)}$, and $r_{(310)}$ in the anion sublattice Dai et al. (1996b).

Withers et al., (1991, 1992) published electron diffraction patterns of ZrO_2-Ln_2O_3 in a wide dopant concentration range with Ln = Pr, Nd, Sm, Tb, Gd, Dy, and Ho. The diffuse scattering patterns show C-type or pyrochlore-type solid solution features, and vary with the dopant type. No rules were found in terms of the radii of the dopant cations. The authors believed that the defect fluorite solid solutions are best regarded a genuinely intermediate between the two-member structures (fluorite and pyrochlore/C-type) and of commensurately modulated fluorite type.

It is well known that at the lower solubility limit of the fluorite-type solid solution region, $11\bar{2}$ reflection spots, which are not allowed in f.c.c. lattice and are not the result of double diffraction, always appear in electron diffraction patterns (Suzuki et al., 1985; Zhou et al., 1991; Miida et al., 1994; McClellan et al., 1994).

To study the diffusionless cubic-to-tetragonal phase transition and microstructural evolution in sintered zirconia-yttria ceramics, Zhou et al. (1991) reported that the displacement of oxygen ion along $\langle 001 \rangle$ directions is responsible for the appearance of $\{112\}$ reflections in the ZrO_2-Y_2O_3 with Y_2O_3 content ranging from 4 to 8 mole % or more. When Y_2O_3 content was below 8 mole %, domain structure was able to be observed in dark-field images. When Y_2O_3 was higher than 8 mole %, domain structure was unable to be observed, but the $\{112\}$ spots are still visible.

To interpret the $\{112\}$ reflections in the 9.9 mole % Y_2O_3-stabilised ZrO_2 single crystals, McClellan et al. (1994) studied the structure of the cubic phase using convergent-beam electron diffraction technique, and concluded that the forbidden reflections were caused by distortion of the oxygen sublattice of the cubic structure from $F3\bar{m}3$ relative to the cation sublattice by displacements along $\langle 111 \rangle$ directions. As a consequence of the distortion, the space group of the crystal is $P\bar{4}3m$ rather than $F3\bar{m}3$.

Yashima et al (1994) ascribed the $\{112\}$ reflections at lower limit of the fluorite-type solid solution region to a tetragonal phase t'' without tetragonality. A space group $P4_2/nmc$ was assigned to the t'' phase. A direct interpretation of those forbidden spots will be given in chapter 5.

2-19

2.3.2 X-ray Diffraction

Morinaga, Cohen, and Faber (1979, 1980) studied the defect fluorite structures of $Zr(Ca, Y)O_{2-x}$ single crystal using X-ray diffraction technique. They suggested that there are displacements of oxygen ions from the ideal fluorite structure along $\langle 100 \rangle$ directions similar to those that occur on the cubic to tetragonal transition in pure ZrO_2 below 1273 K, and that there are small displacements of the cations in $\langle 111 \rangle$ direction in the yttria-stabilised zirconia. To interpret the diffuse scattering, the author proposed that oxygen-ion displacements preferentially along $\langle 100 \rangle$ direction plus short-range ordering with dopant cations as next neighbour to the oxygen vacancies may account for the presence of diffuse diffraction maxima.

Welberry et al. (1992) used a position-sensitive detector (PSD) system to make measurements of the diffuse X-ray scattering on a cubic Y_2O_3-stabilised zirconia, $Zr_{0.61}Y_{0.39}O_{1.805}$. Two features were observed. By the help of computer simulation technique, the authors believed that one feature, in the form of sets of dark planes normal to $\langle 110 \rangle$, occurs because of size-effect-like strains induced along $\langle 110 \rangle$ intermetal vectors, and another feature, in the form of bow-tie-shaped regions of scattering, originates from the same basic strains but the symmetry of these requires that displacements in $[110]$ direction are out of phase with those in the $[1\bar{1}0]$. Later the authors (Welberry et al., 1993) further explained that the size-effect-like strains are caused by a mechanism in which cations move apart if one or other of the bridging oxygen atoms is missing. In their model, the diffuse spots arise from short-range ordering of the oxygen vacancies, and the short-range ordering is such as to avoid nearest-neighbour $\frac{1}{2}\langle 100 \rangle$ pairs, next-nearest $\frac{1}{2}\langle 110 \rangle$ pairs, and third-nearest $\frac{1}{2}\langle 111 \rangle$ pairs across empty cubes of oxygen atoms, but allows third-nearest $\frac{1}{2}\langle 111 \rangle$ pairs across cubes of oxygen atoms containing the cations.

A computer model of the distribution of oxygen vacancies in cubic stabilized zirconia has been directly synthesize by applying modulation waves to the fluorite-type

average structure by Welberry, Withers and Mayo (1995). When the modulations were applied to $\frac{1}{2} \langle 111 \rangle$ pairs of sites in each of four different orientations within the cube surrounding each cation site, the authors found that the calculated diffraction patterns showed good qualitative agreement with the form of the observed patterns. It was suggested that vacancy pairs oriented along a given $\langle 111 \rangle$ direction produce a strain field that extends to large distances in the plane normal to that direction so that like-oriented vacancy pairs repel each other and that unlike-oriented vacancy pairs do not interact strongly. It was claimed that rings of diffuse intensity of different radii and different degrees of diffusion may be interpreted in terms of the amount of strain induced by such vacancy-pair defects and concentration of defects demanded by the composition.

Proffen et al. (1996a) studied the neutron and X-ray diffuse scattering of calcium-stabilized zirconia, and reported that the defect structure consists of two types of defects: microdomains based on a single oxygen vacancy with relaxed neighbouring ions and microdomains based on a pair of oxygen vacancies separated by $(\sqrt{3}) \frac{a}{2}$ along $\langle 111 \rangle$. All the microdomains are oriented in $\langle 111 \rangle$ directions and within the cubic matrix of CSZ. It was concluded that all observed diffuse data can be explained by the superposition of diffuse maxima located in symmetrically equivalent $[1\bar{1}0]$ zones corresponding to satellite vectors of $\pm (0.4\ 0.4\ \pm 0.8)$ (Proffen et al., 1996b).

Li et al. (1993a, b, c) studied the defect structures of zirconia polymorphs using X-ray-absorption spectroscopy (XAS) technique. They reported that charge-compensating oxygen vacancies caused by Y doping are preferentially located next to Zr ions, leaving eightfold oxygen coordination for the Y ions, and that the distortion of cation lattice in cubic solid solutions is very severe in the local atomic environment.

2.3.3   Neutron Scattering

Carter and Roth (1968) proposed , in a neutron investigation of $Zr(Ca)O_{2-x}$, that oxygen atoms are relaxed around oxygen vacancies and placed along the $\langle 111 \rangle$

directions by about 0.02 nm. They found a strong modulated background and diffuse satellites for the samples that had been annealed at 1370.

Steele and Fender (1974) examined the yttria-stabilized zirconia by Bragg neutron diffraction and the diffuse scattering of long wavelength (0.7 nm) neutrons. To interpret the high values of temperature factors (B_{cation}, B_{anion}) obtained from the refinement of the structure using a least square method, the authors proposed a model in which six nearest-neighbour oxygen ions surrounding an anion vacancy are relaxed and displaced toward the vacancy in $\langle 100 \rangle$ direction by 0.036 nm, and four nearest cations are displaced toward the vacancy in $\langle 111 \rangle$ direction by 0.018 nm, among which two of the four cations are Y ions.

Faber, Muller and Cooper (1978) studied the defect structures of single crystals of $Zr_{0.85}Ca_{0.15}O_{1.85}$ and $Zr_{0.82}Y_{0.18}O_{1.91}$ using neutron diffraction technique. Reflections forbidden by f.c.c were observed and local tetragonal distortions in oxygen sublattice were suggested to cause the forbidden reflections.

Andersen et al. (1986) and Osborn et al. (1986) found that there are two principal contributions to the observed neutron diffuse scattering intensity in YSZ, which consists of forbidden (odd, odd, even) reflections and diffuse peaks located at $\Gamma_{fluorite} \pm$ (0.4, 0.4, $\pm$0.8). The first arises from tetrahedral distortions in small vacancy free regions of the crystal which decrease in volume as the dopant level increases. The second arises from correlated vacancies and their associated relaxed ions in the remainder of the crystal. A defect cluster consisting of a vacancy pair plus relaxation of nearest-neighbour oxygen atoms towards the vacancy along $\langle 100 \rangle$ directions and relaxation of the cations away from vacancy along $\langle 111 \rangle$ directions was proposed by Andersen et al. (1986). With this model the authors obtained reasonable agreement between the calculated and observed intensity distributions. Hull et al. (1988) extended the work of Andersen et al (1986) and Osborn et al. (1986) to high temperatures. They found a dynamic behaviour of the defect clusters with temperature.

Hackett (1987) detailed his studies on the defect structure of yttria-stabilised zirconia using neutron scattering technique. Extending the observation reported in Andersen et

al. (1986) and Osborn et al. (1986), he also suggested that dynamic single oxygen vacancies with relaxed neighbour ions exist along with the vacancy clusters, and that the single vacancies are responsible for the high ionic conductivity found in the stabilised zirconia alloys.

Neder, Frey and Schulz (1990), based on their investigation results on the CaO-stabilised zirconia using neutron scattering technique, shared the same view of the defect structure of stabilised zirconia alloys as that of Andersen et al. (1986), Osborn et al. (1986). But they thought that the dopant cation Ca is the next neighbour of the vacancy. Later, Proffen, Neder, and Frey (1996) modified the previously published structure by saying that all cations next to the oxygen vacancy are most likely zirconium.

To summarise, a pronounced feature in diffraction studies of the defect c-ZrO_2 is the ubiquitous appearance of diffuse intensity in addition to the sharp Bragg reflections expected from an ideal fluorite structure. The diffuse intensity appears in X-ray and neutron diffraction from single crystals but is more obvious in electron diffraction. This is because the amplitude of scattered radiation in the electron case is typically 10^3-10^4 times that for X-rays or neutrons, giving an enormous gain in intensity (Rossell, 1984). There are several common points regarding the diffraction patterns from differing defect fluorite phases revealed in the literature.

(a) When the composition of the stabilized zirconia is at the lower concentration limit of the single cubic phase region, there are forbidden spots indexed odd, odd, even. These spots gradually disappear when the composition moves towards the upper limit of the region.

(b) For a given diffraction technique, the patterns from a given orientation exhibit remarkably similar diffuse features, which differ mainly in size relative to fluorite reflections in different materials.

(c) In any given system, the diffuse pattern does not vary if the composition is changed within broad limits.

(d) Most reported diffuse scattering patterns are presented in $\langle 110 \rangle$ zone projection or the zeroth layer of $\langle 110 \rangle$ zone.

(e) There are several models for the defect structure of stabilised cubic zirconia. They can be divided into two types, one is related to microdomains in f.c.c matrix. The other is related to short range ordering consisting of single vacancy or vacancy clusters, and displacements of ions around oxygen vacancies.

Several of these authors, however, have been confronted recently with criticism of their description of the differing varieties of CSZ. Withers et al (1999) have suggested that the complex ordering scheme described by Dai et al. (1996 a, b) is unlikely to be correct since the zirconia alloy systems involve more than one sublattice. Similarly the "doubly-disordered" model for CSZ given by Morinaga et al. (1979, 1980), with random occupation of the (zirconium) cation sites by the dopant cation and corresponding random occupation of the anion sites by oxygen vacancies and short-range order (SRO) describable by Cowley-Warren SRO parameters has come under criticism by Welberry and Butler (1994). They showed how Morinaga et al's X-ray data may be reinterpreted in favour of microdomain-type long-range order in the light of strong chemical evidence for cationic order evident in high-resolution electron micrographs of Ca-CSZ (Rossell et al., 1991). So, if a crystallographically coherent but inhomogeneous model like those of Hull et al. (1988) and Allpress and Rossell (1975) is accepted as the more likely candidate for the microstructure of CSZ, then deductions from single-crystal interpretations of diffraction data (e.g., McClellan et al's 1994 convergent beam electron diffraction determination of the space group) cannot be correct.

In this thesis, the static microstructural working model adopted is that of Allpress and Rossell (1975), where, as stated earlier, microdomains in the mesoscopic size range (a few tens of Ångstroms) containing all (or most) of the dopant and accompanying immobile vacancies are embedded in a distorted cubic ZrO_2 matrix containing little (or no) dopant cations. The microdomains are composed of one or more "neighbouring" line phases (or recognizable versions of them) which, being of lower symmetry, can fit coherently onto the average cubic lattice in a certain number of equivalent cystallographic directions in a random distribution. This Allpress-Rossell picture for CSZ is the basis of our theoretical justification for glassy behaviour, to be described in the next chapter. Conduction of oxygen ions is considered to take place through the

ZrO_2 matrix by means of a small "equilibrium" number of mobile vacancies in the matrix. This description of Ca-CSZ is also very similar to that of Proffen et al. (1996).

The dynamic model we consider operative for CSZ in this thesis is that of Hull et al. (1988), where a distribution of coherently intergrown "aggregates" containing the dopant ions and the immobile vacancies plays the role of Allpress-Rossell's (1975) microdomains, a relatively vacancy-free distorted cubic region plays the role of the matrix and a single vacancy mobile at high temperatures is considered responsible for the ionic conduction. Although applied to Y-CSZ in Hull et al's case, this description is also very similar to the models of Allpress-Rossell (1975) and of Proffen et al (1996) for Ca-CSZ. The high-temperature neutron diffraction experiments described in chapter 7 are based on Hull et al's (1988) model.

CHAPTER 3

GLASS THEORY AND MODEL

3.1 Temperature Ranges of Glassy Phenomena

The theory of glass formation and behavior has been an extremely busy field in the last fifteen years, with new viewpoints, experiments and glassy substances appearing in the literature at an enormous rate. It is extremely difficult to keep abreast of all the reported developments which currently are presented dealing with spin glasses, structural glasses (or window glasses; real glasses), orientational glasses and other grossly disordered materials both organic and inorganic. It is far from obvious that any of them offers a uniquely clear view of the behavior of glasses at or below T_g, the glass transition temperature, although some aspects of the rapidly-growing literature appear to support growing agreement between theory and experiment, but only over a limited range of temperatures. For this reason, the present discussion will be limited to developments with some degree of experimental foundation, and which bear most immediately on the experimental results presented in this thesis.

One of the difficulties apparent in developing theories to describe glassy behavior is the wide temperature range of the phenomena, even for one well-characterized glassy substance. In a structural glass it is generally established that a glass transition can be detected experimentally at a low temperature (T_g) by calorimetric or dilatometric means and that at a higher temperature, T_m, the glass will melt. In between, the glass is said to undergo supercooling, a metastable condition in which the glass begins to display recognizably glassy attributes on cooling above T_g. Probably the most remarkable of these is a rapid increase in the glass viscosity of approximately twelve orders of magnitude while being cooled between T_m and T_g. The detectable event at T_g is widely considered to be a dynamical phenomenon rather than an equilibrium phase transformation, since the numerical value of T_g usually varies logarithmically with the speed of cooling in the super-cooling regime. The glass is considered in this dynamical interpretation to "fall out of equilibrium" at T_g and that the transition reflects the inability of the glass to adjust to equilibrium as T_g approaches since its capacity to adjust structurally has been frozen. It is also sometimes claimed that a "hidden" equilibrium

phase transition exists at some temperature below T_g which can never be reached due to the enormous increase in the glass viscosity experienced by the melt, so that such a glass can be considered to be a non-equilibrium material forever suspended above its critical point. If such an equilibrium transition could be reached however, it has been conjectured that it would provide a resolution of "Kauzmann's Paradox", in which the residual entropy of the glass would suddenly drop to zero, thereby avoiding a contravention of the third law of thermodynamics (Kauzmann, 1948). At present, the existence of this transition is an open question. Certain simple approximate " scaling relations" have been known for a long time. For a wide variety of glasses both organic and inorganic, it is approximately true that $T_g(K) \approx \dfrac{2}{3} T_m(K)$, where both the glass temperature and the melting temperature are expressed in degrees Kelvin (Kauzmann, 1948; Sakka and McKenzie, 1971). This is known as the "two-thirds rule", so for a glass with T_g near 500°C, melting would appear near 900°C.

Another more controversial phase transformation is sometimes claimed to take place at a temperature T_L, which we will call the Leutheusser temperature (Leutheusser, 1984), where a relatively sudden change takes place in the transport properties (i.e. diffusion and viscosity) of a glass, which is believed to be due to coupling between density fluctuation modes in the material. This "mode coupling" behavior is considered to begin at $T_L(K)$ where

$$T_L(K) \approx 1.2 - 1.3 T_g(K),$$

so that a material with T_g near 500°C will experience on cooling a sharp preliminary increase in rigidity as the temperature falls below about 700°C.

3.2   Mode Coupling and Fragile Liquids

The strength of the calorimetric signal at T_g in a glass-forming material is strongly dependent on the type of glass to be formed on freezing. The signal is weakest in the category of network-type glass formers such as SiO_2 or BeF_2 and strongest (at least among those at present under frequent investigation in the literature) in organic or ionic glass formers such as potassium calcium nitrate (CKN) or O-terphenyl, neither of which is an engineering material. This deduction correlates well with a distinction drawn between glass-forming liquids into two types: strong and fragile. It is considered that strong glass-formers possess a network structure even in the liquid state and undergo a gradual increase in viscosity as the temperature falls resulting in Arrhenius-type behavior in the viscosity as a function of temperature. The network structure is not considered to undergo any sudden change near the glass transition. This is the reason for calling such a glass former "strong". In fragile glass formers, however, Arrhenius plots of the viscosity suggests a two-stage process in which the density fluctuations (accessible via neutron diffraction), the viscosity and the diffusion process undergo relatively sudden qualitative change at T_L, so that the viscosity-temperature graph displays a sharp change in curvature near this temperature (see Fig. 3.1).

Fig. 3.1 Viscosity temperature relation (after Angell, 1988).

Mode Coupling Theory

This characteristic two-step behaviour of fragile glasses is attributed to a coupling between density fluctuation modes in the viscous liquid in the treatments of Leutheusser (1984) and of Bengtzelius, Götze and Sjogren (1985) which are now outlined.

The fundamental quantity in the mode coupling theory (MCT) is the normalized correlation function, $\Phi(k,t)$

$$\Phi(k,t) = F(k,t)/S(k) \qquad (3.1)$$

Here, $F(k, t)$ is the density autocorrelation function (which can be accessed via inelastic neutron scattering) and $S(k)$ is the equal-time autocorrelation function or static structure factor, which is accessible using X-ray or electron diffraction. (Chapter 1)

The measured correlation functions (or their frequency spectra) display a "stretching" feature characteristic of supercooled fragile glass formers in which the distribution of relaxation times is described (approximately) in the following way

$$\Phi(t) \propto \exp(-t/\tau)^{\beta} \qquad (3.2)$$

where $\beta<1$ and τ is the characteristic relaxation time at temperature T. Such a stretched exponential gives a reasonable account of the long-time decay of the correlation function, sometimes known as the α-relaxation. This glassy relaxation process may be detected experimentally as a peak in the corresponding dynamical susceptibility $\omega S(k,\omega)$ and shifts to lower frequencies as the temperature falls. For Y-CSZ, its appearance has been noted as peak in ε^{*}, the dielectric loss factor (Chen and Sellar, 1996).

In terms of the normalized autocorrelation function Φ, the MCT in its simplest form may be expressed as the solution $\Phi(k,t)$ of the generalized Langevin equation

$$\ddot{\Phi}(k,t) + \gamma(k)\dot{\Phi}(k,t) + \Omega^{2}\Phi(k,t) + \int_{0}^{t} M(k,t-t^{'})\Phi(k,t^{'})dt^{'} = 0 \qquad (3.3)$$

the first three terms of which may be considered to be those of an equation for a damped simple harmonic oscillator (in this case the autocorrelation function) with a fourth term added representing relaxational memory effects. The undamped oscillator frequency Ω is given by $\Omega^{2} = \upsilon_{0}^{2}k^{2}/S(k)$ and $\upsilon_{0}^{2} = \dfrac{k_{B}T}{m}$, where υ_{0} is the thermal velocity.

Taking the Laplace transform $\Phi(k,z)$ of the autocorrelation function

$$\Phi(k, z) = i\int_0^\infty \exp(izt)\Phi(k, t)dt \qquad (3.4)$$

where Im $Z > 0$,

a relatively simple expression for Φ is obtained

$$\Phi(k, z) = -1/\{z - \Omega^2(k)/[z + M(k, z)]\} \qquad (3.5)$$

For the ideal case, in which the couplings to currents and to fluctuations of the energy are ignored, the memory kernel $M(k, t)$ may be approximated as

$$M(k, t) = \sum_{k_1} v^{(1)}(k, k_1)\Phi(k_1, t) + \frac{1}{2}\sum_{k_1, k_2} v^{(2)}(k, k_1, k_2)\Phi(k_1, t)\Phi(k_2, t) + \cdots \qquad (3.6)$$

The "vertex terms" $v^{(j)}$ are expressible as function of $S(k)$ and are therefore dependent on temperature and density.

In the comparatively straightforward representation above, the theory in its simplest form retains only pair products of the microscopic density and the memory function reduces to a function quadratic in $\Phi(k, t)$, providing a non-linear feedback mechanism. When the foregoing two equations above are solved simultaneously, it is found that the correlation functions do not necessarily decay to zero in the limit of long times, tending instead towards a positive value known as the Edwards-Anderson (EA) order parameter, to be introduced in the next section. Such behavior in the correlation function for a glassy material indicates that the material retains some memory of its earlier states and is therefore "non-ergodic", whereas a zero value for the EA order parameter would indicate that the dynamical system visits every available state equally, or "ergodically". The ideal freezing process described above has therefore been described as an ergodic/non-ergodic transition and is identified with the MCT, considered, as we have seen, to occur in some materials at a temperature T_L above the glass transition T_g. Considerable controversy still surrounds the MCT and its predictions. It is generally considered, however, to offer a reasonable qualitative description of the dynamical phenomena occurring in supercooled liquids at temperatures about 25% higher than T_g (K). For a derivation of the equations described above and recent reviews of the MCT see Götze and Sjogren (1992).

The "simplest" version of the MCT described above is incomplete, however, as we have noted. It predicts the complete glassy freezing of the large-scale collective structure rearrangements in the supercooled liquid and that the α-relaxations cease completely at T_L. In fact, the familiar calorimetric glass transition at T_g plays no role whatever in the

simple form of the MCT as recently developed, which ignores the possibility of locally activated processes leading to jump diffusion of atoms between sites in the disordered matrix, so that α–relaxation can continue below T_L rather than halting altogether at T_L as predicted by the simple ("ideal") MCT theory outlined above. Some mechanism of this kind must be in operation in real glasses, including fragile ones, since the experimentally detected α–oscillations are not observed to undergo sudden and total structural arrest. Two other key predictions should mentioned, however, which are deduced from the non-linear feedback mechanism. These are that the structural arrest process is wave-number independent and that all other two-point correlation functions between quantities related to the density fluctuations will exhibit variations at T_L due to the MCT, so that as well as diffraction phenomena, dynamical critical behavior should be observable in such thermal and mechanical properties as the specific heat and coefficient of expansion of a glassy specimen. The application of the MCT to describe mode-coupling behavior in CSZ will be given in later chapters.

3.3   Spin Glasses, Orientational Glasses and Structural Glasses

There is at present no established theory available to describe the behavior of structural glasses or liquids cooled into the supercooling range. A great deal of theoretical effort in the last twenty-five years has concentrated on an analogous topic whose connection with "real" glasses may seem tenuous at first. This topic refers to the class of disordered magnets known as spin glasses. It involves the thermodynamic and kinetic study of the collective behavior of localized (atomic) electron spin dipoles belonging to certain magnetic atoms randomly substituted on the lattice of a non-magnetic host metal, e.g., an 1 mole % random solid solution alloy Fe (which is magnetic) in a matrix of Au (which is not). The net magnetization of such an alloy displays metastability and irreversibility somewhat like that of structural glasses, and hence has been called a random magnet or spin glass (SG). In the geometry of spin glasses, since the magnetic interactions of the randomly-placed magnetic atoms is oscillatory as a function of distance in the lattice (e.g. as in the RKKY Ruderman/Kittel/Kasuya/Yosida interaction), magnetic disorder arises among the spins due to the fact that pairs of spins which are differing distances apart in the non-magnetic matrix will be neither completely in a state of mutual ferro-magnetic

exchange nor completely in a state of mutual antiferro-magnetic exchange when all their disordered pairwise interactions are added. If we characterize them as disordered Ising-type spins (i.e., as localized magnetic dipoles, each situated on a randomly-placed dopant atom, modeled as small arrows with up-down, plus-minus reflection symmetry as in Fig. 3.2a), then below some temperature, they will freeze into a glassy configuration like that in Fig .3.2b. If a snapshot of a structural glass can be said to look like a snapshot of a liquid then the snapshot of an SG can be said to resemble that of a paramagnetic i.e., a ferromagnetic material held at high temperature, where thermal fluctuations have overcome the ordering effect of the exchange energy, so that no long-range magnetic order remains.

Ising - type exchange (Schematic)

Figure 3.2a   Ising Antiferromagnetism

Figure 3.2b   Ising Spin Glass

Figure 3.2c   Ising Ferromagnetism

The Hamiltonian (total energy function) of a ferromagnetic in the Ising picture is given by

$$H\ (Ising\ ) = -\sum_{ij} J_{ij} \underline{S}_i \cdot \underline{S}_j \qquad (3.7)$$

where $\underline{s}_i$ is the (vector) magnetic dipole at lattice point i and J_{ij} is the exchange coupling term, positive for ferromagnetism and negative for antiferro-magnetism. Note that the Ising model itself, though crude as a model for magnetic materials, is purely deterministic, with no randomness of exchange, so that the metal described possesses only one type of exchange coupling term J and that this J is uniform throughout the lattice, i.e.

$$H\ (Ising\ ) = -J\sum_{ij} \underline{S}_i \cdot \underline{S}_j \qquad (3.8)$$

In a spin glass, however, the Hamiltonian representing the sum of the potential energy due to all pairs of magnetic spins at their random positions on the lattice of the non-magnetic host includes random exchange couplings between all the pairs, due to the oscillatory magnetic interaction potential. In 1975, Edwards and Anderson made the observation that, regardless of chemical or physical source, the random character of the Hamiltonian for all types of metal-alloy spin glasses (e.g., Fe-Au) could be usefully summarized by the following expression

$$H(SG) = -\sum_{ij} J_{ij} \underline{S}_i \cdot \underline{S}_j \qquad (3.9)$$

where J_{ij} is now approximated by a normally-distributed random variable instead, as before, of some oscillatory function gradually reducing in magnitude with distance in the lattice. The new "effective coupling constant" J_{ij} becomes a phenomenological variable, mathematically tractable but no longer specifically related to any real random magnetic system. As we shall see, J_{ij} remains, however, a very useful parameter in the classification and discussion of glassy behavior in stabilized zirconia. An accessible and up-to-date reference for spin glasses and related materials is the book by Fischer and Hertz (1991).

Two further fundamental points regarding behavior seemingly common to all SG materials should be mentioned in this introduction, to be referred to later in discussions of the observed behavior of stabilized zirconia. These are the related properties of disordered ferro- and antiferro-magnetism and of frustration. In brief, if in a real magnetic material the exchange interaction is oscillatory, then the individual randomly-placed magnetic dipoles, while able to flip, may not be able to satisfy all their energy

minimizing exchange requirements on account of the conflicting ferro and antiferro "signals" from the oscillatory exchange interaction. The spin configurations become metastable, spin-flipping for long periods in search of a unique minimum-energy configuration. This situation is known as "frustration" of the spins. For the three-dimensional Ising spin glass with ferro and antiferro interactions it is believed that an equilibrium phase transformation takes place. An appreciation of the character of frustration may be gained even in the non-random case by considering the simple triangular array of antiferro-magnetically coupled spins situated in Fig. 3.3. The implication is clear. To minimize the total potential energy of the array, it is not possible to conclude whether the third Ising spin should point up or down. It is therefore frustrated. See (e.g.) Toulouse (1977). Whereas the mode-coupling theory (MCT) concentrated on the density-density autocorrelation function $F(k,t)$, Edwards and Anderson (1975) suggested the following expression as the most natural order parameter for the breaking of ergodicity in spin glasses with Ising (up-down) symmetry

$$q_{EA} = \lim_{t \to \infty} \lim_{N \to \infty} \left[\langle s_i(t_0) s_j(t_0 + t) \rangle \right]_{av} \qquad (3.10)$$

where the average is over an infinite set of reference times t_0 and N is the total number of spins, i.e. the relevant Edwards-Anderson order parameter for spin-glasses is the long-time autocorrelation function for magnetic spins randomly arranged on a lattice, whereas that for structural glasses is the long-time autocorrelation function for density fluctuation in the cooling liquid (or melt). Similarly, whereas the spin-glass EA autocorrelation function can be considered to be the local mean-square magnetization of the spin, in the structural glass case the EA autocorrelation function is related to a local Debye-Waller function.

Orientational Glasses

An important extension of Ising-type SG for the present experiments is that of the orientational glass. In this case the number of components of the generalized spin can be extended beyond the two (up and down) appearing in the Ising case. Instead the number of spin components may now assume any integer value n, becoming (in the non-random case) the "n-component Potts model". Of course, the simple up-and-down inversion symmetry is now lost, however. In the glassy case, where disordered n-component

3-9

"spins" may occupy the lattice sites at random, the array is called a Potts glass. Gross et al (1985) have shown that an equilibrium phase transformation may be expected in this type of material as well. For the number of components greater than four, this transition is considered to be first order. In several papers published in 1987 and 1988, Kirkpatrick, Thirumalai and Wolynes pointed out that, despite one model being formulated on a lattice, many close formal similarities exist between dynamical (kinetic) prescriptions for the Potts glass model without reflection symmetry and the MCT for the structural glass i.e., that each of the models should display both the Leutheusser-type mode-coupling transition and the Kauzmann-type "entropy crisis" transition. This is a remarkable result since spin-glass-like systems such as the orientational glasses just discussed are considered to have their structural disorder "quenched in", i.e., the positions of the impurity or dopant atoms (and hence the spins) are fixed in time by some high-temperature preparation, unaffected by "annealing" of the alloy in the supercooling region, which is considered to be at a much lower temperature. Structural glasses, by contrast, are not considered to contain any such quenched disorder. Since the aim of the present work is to describe the properties of stabilized zirconia in terms of a generalized orientational glass to be outlined in the next section, the point that needs to be made here is that we can expect CSZ to behave in a way very similar to that of a "real" (structural) glass with both Leutheusser and Kauzmann-type transition in principle observable. Even if the latter turns out to be inaccessible, then the usual calorimetric or dilatometric dynamical transition to be expected at T_g should still be detectable, as in other glasses.


Fig. 3.3 Illustration of frustration on triangle of antiferromagnetic Ising spins.

3.4 A Description of the Allpress-Rossell Model for CSZ in Terms of the VKZ Orientational Glass Theory

All the spin-glass or orientation glass systems studied so far in this thesis have had their dipolar "spins" placed randomly on an essentially rigid lattice. In order to compare predictions from a realistic model with experimental diffraction results from CSZ, it is necessary to find a formulation of the problem which tests the Allpress-Rossell microdomain model. Gross, Kanter and Sompolinsky demonstrated that a glassy model with n-component "elastic spins" could be found with properties very similar to those of the n-component Potts orientational glass. This model is called the n-component quadrupolar glass (QG) in which the "spins", here modeled by the principal axes of uniaxial elastic quadrupoles, can point in a finite number of different directions on a rigid lattice. It differs from the Potts glass chiefly in not attaining a completely frozen state. The final step in linking lattice-based spin-glass-type theories to CSZ is taken by allowing the lattice to become deformable. The consequences are clearly in evidence in the experimental behavior of CSZ. Several theoretical papers were published early in this decade on the topic of orientational glasses in deformable materials ("mesoscopic elasticity") and we will later use their results in a very direct way to interpret our experimental data.

Grannan, Randeria and Sethna (1988, 1990) (GRS) were able to show computationally that two randomly-located uniaxial elastic quadrupolar defects embedded in a homogeneous elastic medium will tend to order antiferro-elastically into a "tee" ("T") configuration at low temperatures with the principal axis of one of the two quadrupoles parallel to a line joining their centers and the principal axis of the other quadrupole perpendicular to the line, as in Fig. 3.4b. They further showed that such a configuration would lead to frustration if a large number of these elastically interacting defects were to occupy the sites of a three-dimensional Bravais lattice. In a deformable medium with a finite concentration of such randomly-placed defects on a Bravais lattice, a certain fraction of defect pairs will, they showed, interact ferro-magnetically as well, with parallel alignment of quadrupole orientations as in Fig. 3.4a. Thus, the systems considered by GRS appear to possess all the essential properties of a spin-glass model i.e., randomly mixed ferro- and antiferro- configurations and subsequent "spin" frustration. Strong

evidence for the "tee" configuration in room temperature diffraction patterns from CSZ will be presented in chapter 5.

Ferroelastic

"tee"

antiferroelastic

Fig. 3.4 Ferroelastic and antiferroelastic "exchange" between pairs of reorientable defects in a plane.

The VKZ theory (general)

The theoretical paper whose contents are to be described below ("Discrete-state models of orientational glasses" by H. Vollmayr, R. Kree and A. Zippelius (VKZ), 1991) is probably the most important single reference for the whole thesis, describing the phase equilibria and elastic properties with structures like cubic zirconia where the microdomains may be realistically modeled by elastic quadrupoles.

Extending the GRS theory, Vollmayr, Kree and Zippelius (VKZ) consider reorientable quadrupolar elastic defects embedded in an elastic matrix, only this time the defects are no longer point-like. Now they are considered to be coherently intergrown with a crystallographically cubic, deformable elastic matrix, just as in the Allpress-Rossell model. As before, the defects may be modeled as uniaxial elastic quadrupoles, but, being crystalline atom-vacancy complexes some tens of Ångstroms across ("mesoscopic") embedded in a cubic matrix, the orientation of the defects with respect to the axes of the matrix are restricted by the host's lattice anisotropy.

VKZ considered three crystallographic possibilities for the lattice anisotropy with discrete sets of allowed orientations only. Thus, the defect may be parallel to the host's four-fold cubic axes (VKZ case A), parallel to the host's body diagonals (case B), or parallel to the host's face diagonals (case C). With those restrictions, VKZ studied the elastic interactions between randomly-located pairs of quadrupoles aligned as in case A, B, or C. As we shall see, VKZ were able to demonstrate that both glassy and homogeneous elastic phases could be generated by the three-state (case A), four-state (case B) and six-state (case C) defect models at low temperature, depending on the model parameters.

The VKZ theory (model building and approximations)

Though most of the experimental results to be presented in this thesis involve Y-CSZ (i.e., zirconia stabilized by yttria (Y_2O_3) at various dopant concentrations, an initial description of the correlation between theory and experiment is most simply displayed by considering the behaviour of Ca-CSZ (calcium-stabilized zirconia). In the Ca-CSZ case the six possible orientations for the unique b-axes of the crystalline line phase

ϕ_i (CaZr$_4$O$_9$) correspond closely to the six "orientation states" of VKZ case C. The ϕ_1 microdomains are now considered to be quadrupolar defects reorientable by means of a locally reconstructive diffusion process.

As we have already noted, the VKZ theory introduces a class of model for systems of rigid, immobile, reorientable defects randomly located on a deformable cubic lattice, to be described only at a semi-microscopic level. The defects are considered to possess uniaxial symmetry, so that the orientational configurations may be characterized by a unit vector $\overrightarrow{d}$. The computational method of VKZ involves the calculation of the partition function from an effective Hamiltonian. At this point it is appropriate to discuss several of the approximations made in the VKZ derivation of the long-wavelength elastic properties of the model because in a real material the disorder quenched in leads to large fluctuations on microscopic length scales and the reorientation of defects near transition leads to anharmonicity, neither of which is treated within the theory. A concept used in constructing the VKZ theory and crucial for the interpretation of some of the present experimental work is the connection linking phase transformations with universality and the renormalization group. Briefly, the main aspect of universality is that as the temperature is lowered to correspond to that of an approaching phase transition and the paramagnetic spin-flip process slows down, the correlation length (i.e. the maximum distance between spins with highly-correlated spin-flip fluctuations) will grow, in principle to infinite size at a second-order transition, but to large finite values in general. In such a "critical" state there are correlations between spins on all scales and the susceptibility of the spin system to external fields becomes large. The correlation length is now the most important scale in the system, much larger than the unit cell length and larger than any phenomenological "coarse-graining" length corresponding approximately to the size of the Allpress-Rossell microdomains. Two parameters now govern the phase transformation: the dimensionality of the order parameter and the dimensionality of the space in which the order parameter transforms. What this means for transitions in zirconia is that the apparent discrete set of microscopic orientations (e.g., VKZ's A, B or C anisotropies) may not turn out to determine the resultant low-temperature structure, due to changes in the anisotropy potential while the correlation grows as the transition is approached. For a clear introduction to universality and the renormalization group including phenomenological "coarse-graining" and effective Hamiltonians see the book by

Pfeuty and Toulouse (1977). Such a phenomenological approach is necessary so that long-wavelength terms due to elasticity may emerge relatively simply in the effective Hamiltonian. So, with the remarks above in mind, we assume that near an equilibrium spin glass the correlation length of thermal orientional fluctuations is large enough so that a relatively simple effective Hamiltonian is operative and that the following approximations hold. This discussion follows closely that of the original VKZ paper.

(i)   The ranges of all inter-atomic forces are small compared with that of the coarse-graining length, which is in turn small in comparison with correlation length of the long-wavelength critical fluctuations

(ii)   On mesoscopic length scales the effective Hamiltonian will be a quadratic function of the displacements, displaying essentially harmonic behavior throughout

(iii)   Under universality, near a phase transition the Hamiltonian contains a term describing the local anisotropy, restricting orientational fluctuation to a discrete set of states, corresponding to the absolute minima of the anisotropy potential on the coarse-graining scale. For the purpose of interpreting the results of Chapter 5 it is important to note that, as VKZ point out, under the operation of the renormalization group, the absolute minima of the anisotropy potential may change when approaching the transition, and that at criticality the resulting anisotropy is not necessarily the one to be expected from microscopic considerations.

The simplest effective Hamiltonian studied by VKZ takes the form

$$H_{eff} = \sum_x \left\{ \frac{1}{2} \varepsilon_{ij}(x) C^0_{ijkl} \varepsilon_{kl}(x) + \sigma_{ij}(\underline{d}(x)) \varepsilon_{ij}(x) + \upsilon(\underline{d}(x)) \right\} + \frac{1}{2} \sum_{xx'} J_{xx'}(\underline{d}(x), \underline{d}(x')) \qquad (3.11)$$

where x is a position coordinate on a cubic lattice. The terms under the first summation represent the elastic parts of the Hamiltonian involving the states of stress and strain in the matrix and of the interaction between the defects with the matrix. The term under the second summation represents the interactions of the randomly-located defects with each other, i.e., it is the spin-glass part of the Hamiltonian.

In detail the coarse-grain terms in the effective Hamiltonian are:

ε_{ij} is the local strain tensor.

σ_{ij} is the local stress arising from a defect in the orientational state $\underline{d}(x)$.

C_{ijkl}^0 are the bare elastic constants (i.e. not renormalized by the long-range interactions at criticality) on the mesoscopic coarse-graining scale. Here, bare means the elastic constants operating before the spin-glass-type interactions are switched on in the low-temperature phase.

$\upsilon(\underline{d}(x))$ denotes the local anisotropy energy.

The spin-glass-type coupling term $J_{xx'}(\underline{d}(x), \underline{d}(x'))$ between the defects is considered to be random due to the random placement of the defects. As mentioned before, GRS determined that quadrupolar interactions between two defects in a homogeneous elastic medium would tend to order the defect orientation in a "tee" configuration.

VKZ considered anisotropy potentials with absolute minima in the directions of three equivalent sets of cubic symmetry axes, i.e., the $\langle 100 \rangle$ directions, the $\langle 111 \rangle$ directions and, in the case of interest here, the set of six two-fold axes parallel to the face diagonals of the cube, i.e., the $\langle 110 \rangle$ directions.

The effective Hamiltonian then becomes

$$H_{eff} = \sum_x \left\{ \frac{1}{2}\varepsilon(x)C^0\varepsilon(x) + \sum_\mu^p n^\mu(x)\sigma^\mu\varepsilon(x) \right\} - \frac{1}{2}\sum_{xx'}\sum_{\mu\nu}^p J_{xx'}^{\mu\nu}n^\mu(x)n^\nu(x') \quad (3.12)$$

where the superscripts μ, ν each range from 1 to 3, 4 or 6, depending on whether the VKZ crystal anisotropy A, B, or C is under consideration. The occupation or dilution variables $n^\mu(x)$ are equal to unity if the defect at position coordinate x is in the orientational state μ and is zero otherwise. The extra stresses introduced by the uniaxial defects are denoted by σ^μ.

In the anisotropy case A, with defect axes parallel to one of the four-fold directions, e.g., [100], the "extra stress" tensor is of the form (model A)

$$\sigma^1 = \begin{pmatrix} \sigma_0 + \frac{2}{3}\sigma & 0 & 0 \\ 0 & \sigma_0 - \frac{1}{3}\sigma & 0 \\ 0 & 0 & \sigma_0 - \frac{1}{3}\sigma \end{pmatrix} \quad (3.13)$$

where σ_0 is a (diagonal) isotropic stress term.

If the defect axis is body-diagonal, with $\underline{d}$ parallel to $[1\ \bar{1}\ \bar{1}]$ as in case B, the extra stress tensor takes the form (model B)

$$\sigma^1 = \begin{pmatrix} \sigma_0 & -\sigma & -\sigma \\ -\sigma & \sigma_0 & +\sigma \\ -\sigma & +\sigma & \sigma_0 \end{pmatrix} \qquad (3.14)$$

For face-diagonal defects, VKZ computes the extra stress tensor for a defect with unique axis parallel to $\underline{d} = [011]$ (model C) as

$$\sigma^1 = \begin{pmatrix} \sigma_0 + 2\sigma_L & 0 & 0 \\ 0 & \sigma_0 - \sigma_L & \sigma_T \\ 0 & \sigma_T & \sigma_0 - \sigma \end{pmatrix} \qquad (3.15)$$

Note that the factorization of the term $J_{xx'}(\underline{d}(x), \underline{d}(x'))$ to $J_{xx'}^{\mu\nu} n^\mu(x) n^\nu(x')$ makes the VKZ calculation essentially an Edwards-Anderson-type treatment of the interactions.

Results from the VKZ model

The Vollmayr-Kree-Zippelius (VKZ) theory for discrete-state models is lengthy and notationally complex, but essential for our discussion of the Allpress-Rossell model of CSZ. Having established the relevant notation for important quantities and surveyed the main approximations of the theory, we now quote the results of importance for comparison with the experimental results to be reported later.

The main results of the VKZ paper are in the form of the elastic stiffness constants of the models and various phase diagrams corresponding to the models. Depending on the strength of the interactions between the quadrupolar "spins", i.e., on the magnitude of $J_{xx'}^{\mu\nu}$, the crystal can transform either to another homogeneous crystalline phase of lower symmetry, or it can transform to a glassy state with zero net distortion. For the face-diagonal six-state glass case there are two possibilities for the local distortion, depending on two Edwards-Anderson order parameters, q^+ and q^-, corresponding to local tetragonal order and local orthorhombic order respectively. In the literature survey, as we have seen, it appears that only the order parameter q^+ is non-zero in CSZ at ordinary pressures.

VKZ demonstrate that when the equilibrium phase transition temperature is approached from above, the elastic stiffness constants soften, but restiffen below the transition temperature. We will see that mode-coupling sets in experimentally at a temperature some 20-25% higher than VKZ's equilibrium temperature, in line with the predictions of sections 3.2 and 3.3 of this thesis, which makes the restiffening more gradual. The effect is brought out clearly in the x-ray and neutron diffraction experiments in chapter 6 and 7.

3.5 Further Orientational Glass Theories with Results Relevant to the Present Experiments

C.C.Yu (1992) has also published a theory relating to phase transitions among interacting elastic defects. Using an approach somewhat like that of GRS, where the important interactions are those between the "spins", mediated by short-wavelength lattice distortions, Yu finds that two equilibrium spin-glass-like phase transitions occur: one for the diagonal components of the defect stress tensor and the other for the off-diagonal components. The quenched ground state of the off-diagonal components exhibits antiferro-elasticity while the diagonal components do not. The temperatures at which those transitions occur are widely separated on the temperature scale (Yu, 1992). Under the approximations made, the two transitions take place at

$$T_{C-} \approx 0.32 \, J$$
$$T_{C+} \approx 0.42 \, J$$

where T_{C-} represents the off-diagonal antiferroelastic phase transition, which would results in "tees" on the places in Ca-CSZ. T_{C+} is the transition temperature for the normal strain terms. J, of course, is a phenomenological Edwards-Anderson-type coupling strength term, which serves to fix the overall temperature scale. At their respective temperatures, the fourth-order elastic susceptibilities associated with the defects can be considered to diverge.

A mode-coupling description of the dynamics which would correspond adequately to coupled components (i.e., the reorientable defects and the distorted zirconia matrix) in CSZ has been provided by Franosch and Götze (1994).

Briefly, the Franosch-Götze theory states that in a structural situation such as that believed to occur in the Allpress-Rossell model of CaSZ (calcia-stabilized zirconia), where interacting quadrupolar defects can "rotate" between the six equivalent $\langle 110 \rangle$ directions as described by the VKZ theory, it is considered that a MCT-type structural arrest appears in the α-oscillations of the tetragonally-distorted cubic pure zirconia between the microdomain "rotors", which is initiated by an equilibrium phase transition among the (ϕ_1) rotors. As the ϕ_1 rotors (i.e., the reconstructively reorientable microdomain defects) become more antiferro-elastically correlated on the {100} planes of the cubic lattice as T falls below T_m, the rotors increasingly form a rigid "cage" around the distorted cubic material so that its tetragonality (and hence its Edwards-Anderson order parameter) increases until an equilibrium orientational glass transition occurs at T_{OG}. In the Franosch-Götze model A (for two-component glasses and ionic conductors like CaSZ), the EA order parameter immediately takes a sharp upward turn at a temperature corresponding to the equilibrium transition T_{OG}, which then is also identifiable as the Leutheusser temperature T_L i.e., the onset of mode-coupling regime. The modes involved in this case are density fluctuation modes; the gradually tightening antiferro-elastically-locked rotors of the cage arrest the ferro-elastically oscillating α-wave in the tetragonally-distorted cubic matrix. The source and precise oscillatory character of the glassy α-wave is not known, but Chen and Sellar (1996) have associated it with the distorted matrix in the YSZ case as well, in electrical experiments to be described in the next chapter.

Franosch and Götze have given a plot of the EA order parameter/Debye-Waller factor/non-ergodicity parameter as a function of MCT control parameters in their 1994 paper which we reproduce in Fig. 3.5.

Fig. 3.5 Edwards-Anderson order parameter as a function of temperature for the cage rotors (q=1) and the distorted matrix (q=2).

The non-ergodicity parameters represent the long-time values of the correlation functions for the rotors and for the matrix. In the plot shown, the temperature decreases to the right. The abscissa of their plot can be considered to be $1 - \dfrac{T}{T_L}$. The upper curves (q=1) represents the non-ergodicity parameter of the cage rotors and the lower curves that of the distorted matrix (q=2). Note that as the temperature falls below T_L (their zero coordinate) the non-ergodicity parameter curve flattens out; this shape is called the "square-root cusp". The continuous curves (q=1,2) correspond to the "ideal" MCT glass transition, where no α-wave motion persists below T_L. The dashed curves represent the refinement mentioned earlier in chapter 3, where hopping motion is allowed, which partly restores ergodicity and permits α-oscillations to persist below T_L. We will make direct comparisons with the dashed (q=2, matrix) square-root-cusp "hopping-smeared" curves shown here and quasi-elastic neutron diffraction data to be presented in chapter 7.

We have attempted in this section to link the orientational glass temperature T_{OG} of the rotors with T_L, the Leutheusser transition temperature corresponding to the structural arrest of the matrix, by means of the mode-coupling theory (MCT). It is tempting to seek some "scaling regularities" in some of the phenomena that have been discussed: in particular, the non-rigorous "scaling" of the two temperatures corresponding to diverging fourth-order elastic susceptibilities described be Yu (1992). Using the approximate identity of T_L and T_{OG} (here, Yu's 1992 lower planar-antiferro-elastically ordering T_{c^-}), suggests that

$$T_{c^+} \approx \frac{0.42}{0.32} T_{c^-} \approx \frac{4}{3} \cdot \frac{5}{4} T_g \approx 1.6 T_g \approx T_m$$

where $\frac{5}{4} T_g$ is the approximate empirical value for T_L, as mentioned earlier in this chapter although without rigorous foundation. This simple observation prompts consideration of the idea that the temperature associated with the onset of the paraelastic regime for the rotors and strong ionic conduction of oxygen ions and vacancies through

3-20

the matrix may be in some way connected with the divergence of the fourth-order elastic susceptibilities of the rotors themselves, corresponding to the upper transition T_c. identified by Yu (1992) for the diagonal elements of the defect (rotor) stress tensors, at least in fragile glasses.

3.6   Summary

We summarize briefly here the results from this chapter most likely to undergo test in the forthcoming experimental chapters.

If the Allpress-Rossell model of Ca-CSZ, cubic zirconia stabilized by calcia, is well-described by the VKZ six-state model and extensible to Y-CSZ, then several hitherto unrecognized phase transitions should become apparent in experiments conducted using thermal or mechanical probes, or in diffraction experiments which capture the long-term behaviour of the density-density autocorrelation functions. It should therefore be possible to detect the "forbidden" tetragonal diffraction spots in electron diffraction experiments on thin, well-oriented single crystals of CSZ, and to observe the vanishing of these spots at high temperatures above that of the orientational six-state glass transition (chapter 5).

For powder experiments using X-rays, where usually only scatter due to the metals is detectable, it should be possible to detect changes in the intensity of the diffraction lines due to diffuse X-ray scatter out of the Bragg beams (attributable to effective Debye-Waller functions) as a function of temperature to obtain information on the extent to which the Debye-Waller function is wavenumber-dependent. The mode-coupling (MCT) theory would predict it is substantially insensitive to wavenumber. Anomalously dispersive X-ray diffraction could raise the scattering contrast between yttrium and zirconium atoms in the YSZ matrix and supply metal-ordering data on the "rotating species" in Y-CSZ. Whereas the VKZ interpretation of the Allpress-Rossell model as a six-state glass with anisotropy corresponding to VKZ model C fits the known diffraction data, it is not known for the present what exactly is rotating in the Y-CSZ case. This question is answered in part in chapter 6.

The picture presented in this chapter of the microstructure of CSZ i.e., as temperature falls, an increasingly rigid cage of antiferro-elastically-coupled defects causing structural

arrest in the ion-conducting, ferro-elastically-oscillating matrix material (Franosch and Götze, 1994) is put to the test in chapter 7.

We finish this chapter with a review of the temperature ranges where critical phenomena related to the glassy phenomena surveyed might be expected. To establish such a framework we look ahead slightly to the results in the next chapter, where evidence is presented for a glass transition near 400°C and a Leutheusser (MCT) transition near 650°C. This suggests that Yu's (1992) lower antiferroelastic transition between the rotators at T_{c^-} will occur near 650°C and that T_{c^+}, the upper phase transition involving the diagonal terms of the extra defect stress tensor, will occur between 900 and 1000°C, near T_m, the "melting" temperature of the distorted –tetragonal ion-conducting part of the material, no longer "caged" by the quadrupolar defects which are now in a paraelastic state. The supercooling regime is hence 500 –600°C in extent.

CHAPTER 4

INDEPENDENT EVIDENCE FOR GLASSINESS IN YTTRIA-STABILIZED ZIRCONIA

4.1 Introduction

The experiments to be described in the present work all involve diffraction of neutrons, electrons, and X-rays. In the previous chapter, we have described the theory to be used in interpreting such experiments and how it might support the assertion that CSZ is a glassy material: in particular that diluted six-state orientational glasses are likely to behave in a way similar to structural glasses.

There is no way to prove the connection between the diffraction data and glassy behaviour except via the theory, which, as we have seen, combines several approximations and assumptions. This is in part the reason why the alloy's glassy character has not been identified earlier despite intense experimental probing over the past twenty-five years. In this chapter evidence is presented of glassiness more immediately recognizable to the materials engineer, some already published in the literature. By "independent" in this context, we mean independent of the theory in chapter 3 and independent of specific interpretations of diffraction data.

4.2 Early experiments

In 1976, Garvie noted that the thermal conductivity of CaSZ was low and nearly independent of temperature, like that of a glass, identifying the random distribution of oxygen-lattice vacancies as cause (Garvie, 1976), but did not refer to any mesoscopic mechanism of glass transition. Walker and Anderson (1984) examined the thermal conductivity, specific heat, thermal expansion and dielectric response of a concentration series of ZrO_2-Y_2O_3 alloys in the cubic range, at temperature below $10°K$. They found that in each case the results were consistent with zirconia's harboring glassy low-temperature excitations attributable to the existence of disordered two-level "tunneling" states in the material, but were not able to associate

these states with any defects likely to arise form the "doubly disordered" random solid solution model for CSZ. See also Ackerman et al (1986) and Lawless (1980).

All these observations were considered to support the idea that zirconia was extremely disordered, but the authors did not connect the glassy behaviour at the time with mesoscopic reorientable defects which might give rise to a spin-glass-type phase transition of the type discussed in the previous chapter.

4.3   Recent Experiments

In 1996, using standard electrical measurements, Chen and Sellar conducted a systematic yttria concentration series of experiments into the dielectric and conductivity relaxations of single crystals of yttria-stabilized zirconia alloys, to study the behaviour of dielectric properties and whether YSZ possesses the same microstructure as CaSZ, for which direct high-resolution imaging had been possible (chapter 2). The question to be answered in these experiments was whether the structure of YSZ could also be partitioned into two parts:- a distorted cubic matrix through which the oxygen vacancies move and reorientable mesoscopic defects whose disordered collective interaction could cause an OG transition. In these electrical experiments (Chen and Sellar, 1996) it was found that the dielectric properties of YSZ decreased with increase of dopant, consistent with Allpress-Rossell idea that essentially all the dopant cations went into the structure of the non-conducting defect rather than the matrix, gradually choking off the ionic conduction pathways. It was also found that a simple analysis of the measured dielectric loss factor appeared to indicate that for 12 mole % Y_2O_3 dopant sample (in the stabilized cubic range, but of relatively low dopant concentration), a loss peak corresponding to the a-wave would be detected at temperatures below that considered to be the calorimetric glass transition temperature T_g for YSZ (see next section). Hence a structural similarity with CaSZ was established and evidence for glassy behaviour adduced.

Evidence from thermal experiments

For the verification of a glass transition, most materials engineers would require evidence from "simple" thermal experiments, i.e., the familiar calorimetric or dilatometric experiments. These have been carried our and are described below.

(i)   Specific heat at T_g

In structural glasses a rise in the specific heat C_p of charactieristic shape is well known to occur on heating through T_g, the "calorimetric" glass transition temperature. An example of this dynamic phase transition is seen in Fig. 4.1 where an experimental plot is displayed for freshly-prepared YSZ-18 powder.
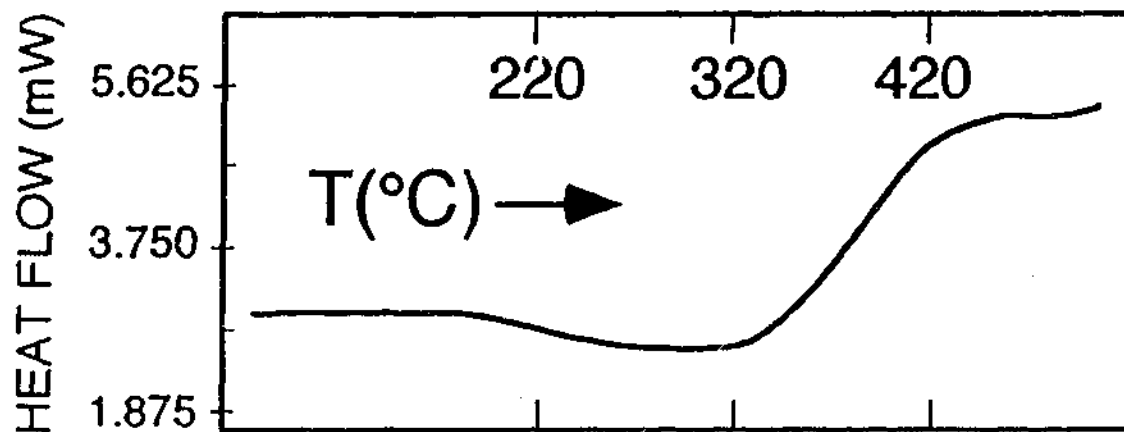
Fig. 4.1 Specific heat of YSZ-18

The C_p experiment was performed on a Perkin-Elmer DSC7 Differential Scanning Calorimeter with a charge of 48 milligram and a (heating) scan speed of 5°C/min.

The transition begins somewhere above 320°C and finishes at approximately 1 Kcal/mole, typical of a structural glass transition. We takes this result as a considerable vindication of the idea that fragile diluted quadrupolar glasses on deformable lattices of the kind described in chapter 3 are thermodynamically very similar to window glasses and that a phenomenon closely resembling a structural glass transition occurs in YSZ-18 near 400°C.

(ii)   Dilatometer traces

4-3

These deductions may be sharpened somewhat by examining the results of a dilatometer experiment conducted in a single crystal of ZrO_2-12 mole % Y_2O_3 (YSZ-12) cut so as to have the dilatometer axis (Adamel Lhomargy D124) coincide with the [310] direction of the crystal. The scan rate is 0.5°C per minute.

THERMAL EXPANSION of CUBIC STABILIZED ZIRCONIA (~12 mole%Y_2O_3)

PARAELASTIC MOBILE STATE

SUPERCOOLING REGION (420°C - 885°C)

FROZEN STATE   T —▶   (°C)

0   400   800 885   1200
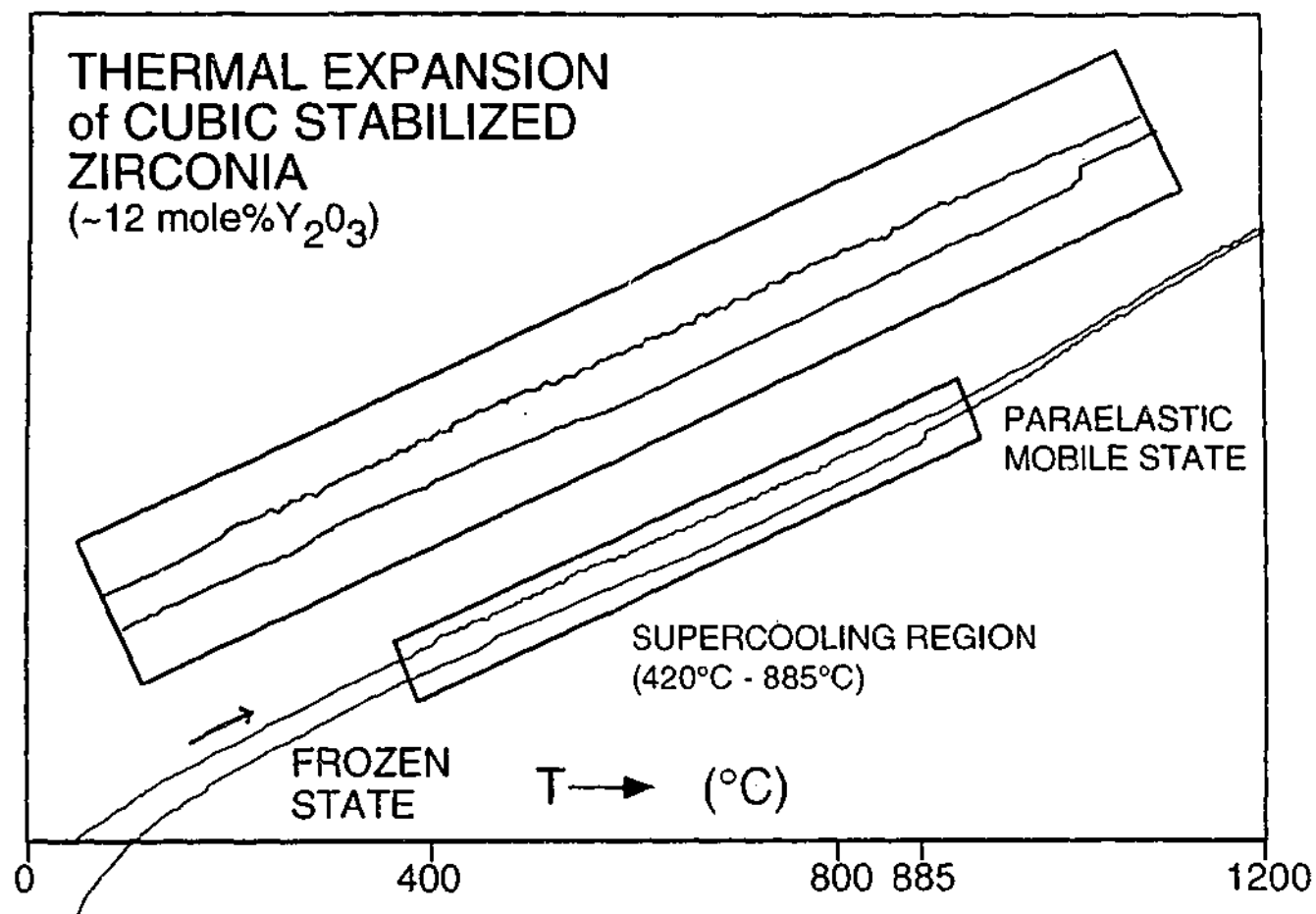
Fig. 4.2   Dilatometer trace displaying the frozen, supercooling and liquid states for YSZ-12.

We have attempted to demonstrate the alloys' glass-like behaviour over a temperature range corresponding to the duty regime of Y-CSZ-based solid oxide fuel cells where (if it were a glass) Y-CSZ should produce two breakpoints in the slope of a dilatometer trance, delineating the frozen glassy state, the supercooling state and the liquid state (here the paraelastic state of the rotors). Representative results are shown in Fig.4.2. We identify the glass transition region to be above 400°C, with T_g approximately 420°C, where the average slope of the dilatometer slope experiences a sharp change and where Barkhausen-like noise phenomena commence during the heating cycle. This noise, which persists throughout the supercooling region,

possesses an apparent average period of the order of a few hours, which is six or seven orders of magnitude slower than Y-CSZ's measured dielectric relaxation (Chen and Sellar, 1996). The amplitude of the noise is roughly 5 microns. These characteristics are very similar to those observed by Patkowski et al (1993) in the supercooling range on heating a low-molecular-weight organic glass, which they interpreted as the ultraslow relaxation of excess volume frozen in their as-received glass specimen during cooling.

A considerable amount of dilatometric hysteresis exists between the heating and cooling cycles even with heating and cooling scan rates the same. Beyond the supercooling region above approximately 885°C, both curves converge somewhat. In Fig. 4.2 this range corresponds to the paraelastic state of the rotors where unique-axis orientation is rapid, corresponding to the liquid state in structural glasses. We identify T_m here as approximately 885°C, where a small but sharp first-order phase transition is observed during the cooling cycle in Fig. 4.2. the dilatometer trace slope changes more abruptly at T_m than in the glass transition region. Under a wide variety of scan rates and yttria concentrations, the ratio T_m/T_g for our samples approximates the value 1.6 cf. Kauzmann's average value of 1.5.

(iii) Location of mode-coupling onset temperature

It was suggested in chapter 3 that certain empirical "scaling relations" appeared to hold in the thermal behaviour of glasses, in particular the onset of the mode-coupling regime, where orientational fluctuations among the elastic quadrupolar microdomains are postulated to control the structural relaxation of the distorted cubic matirx. These approximate relationships placed the mode-coupling temperature regime in the lower half of the supercooling region, so that any sudden onset of structural arrest in the matrix would be near 650°C. Manning et al (1997) have recently discovered that the transport proprerteis of ZrO_2-9.5 mole % Y_2O_3 undergo a relatively sharp change at 650°C of a kind that correlates well with an abrupt MCT-type structural arrest. A first order phase transformation has been found in as-received single crystal of YSZ-15 when a small [110] oriented slab of this material is examined in a dilatometer. Fig. 4.3 demonstrates that on cooling such a specimen at 0.3°C per minute a sharp transformation is observed near 650°C.

420	480	540	600	660	720	780	840	900
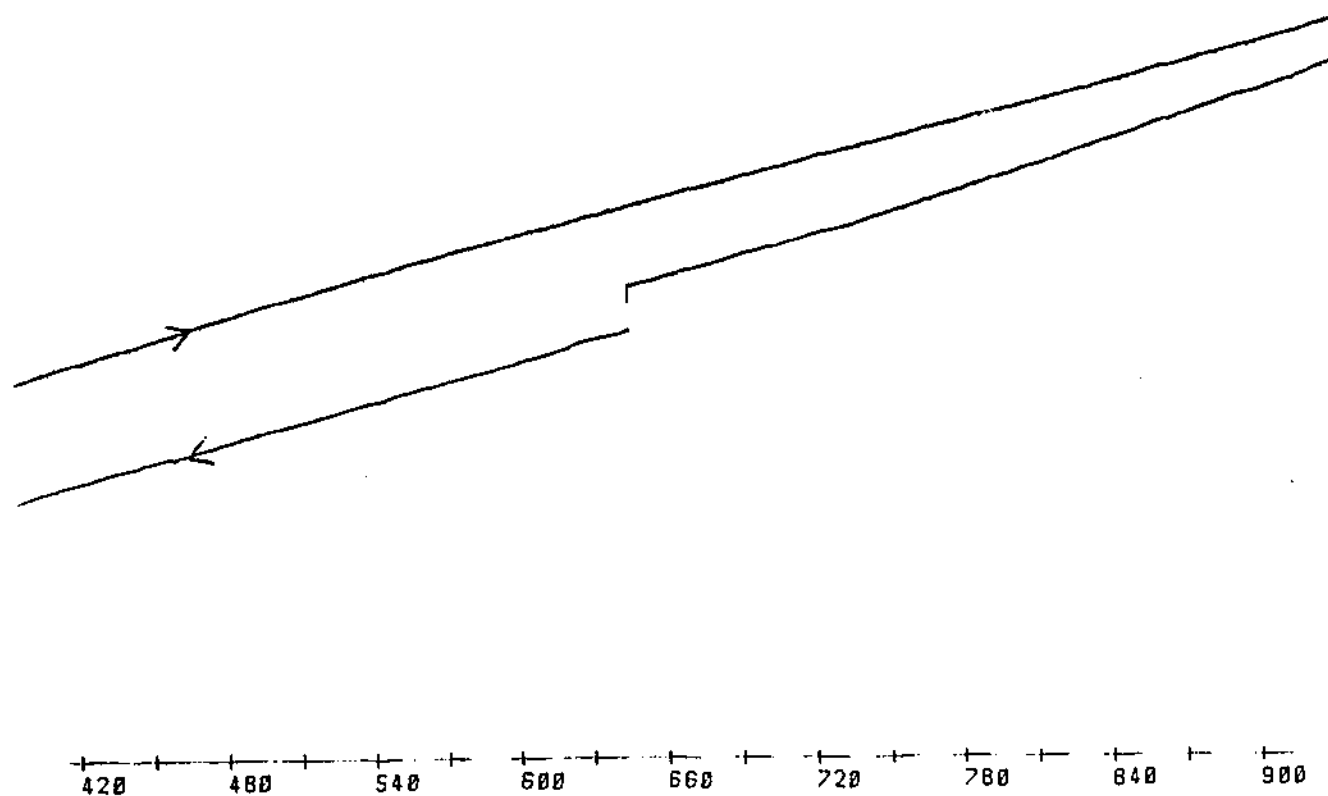
Fig. 4.3 Detection of sharp phase transition in YSZ-15 near 650°C. Specimen size reduction on cooling through the transition ~ 5μ.

4.4. Conclusion

The need to conduct non-diffraction experiments, not requiring a complicated theory for their explanation, has been satisfied in this chapter using calorimetric and dilatometric experiments. Results of familiar type were presented in support of the idea that the (usual) kinetic glass transition occurs near 400°C for yttria-doped zirconia alloys of various concentrations and that mode-coupling behaviour appears near 650°C as predicted by the crude scaling relations. Since the coefficient of linear expansion depends inversely on the bulk modulus (see e.g., Walker and Anderson, 1984), the increase in slope of the dilatometer trace in Fig. 4.2 near 900°C suggests at least a partial softening of the lattice, which we attribute to the liquid-like high-conductance state of the cubic inter-domain matrix. Diffraction evidence in the next three chapters offers considerable support for these conclusions.

CHAPTER 5

ELECTRON DIFFRACTION FROM A SERIES OF STABILISED ZIRCONIA ALLOYS

5.1 Introduction

As discussed in Chapter 2, Literature Review, a great deal of experimental evidence has accrued regarding the diffraction patterns from different types of stabilized zirconia, and the review contains references to articles with widely-varying interpretations of the contrast. In this chapter we examine the diffraction patterns from major crystallographic zones of CSZ as a function of dopant concentration, an approach apparently seldom taken elsewhere in the literature, where almost every paper tends instead to concentrate on a single dopant concentration, so that a concentration-series test of the Allpress-Rossell model is not possible. Although a seemingly simple idea, the employment of a dopant - concentration series in an earlier set of dielectric measurements (Chen and Sellar, 1996) afforded a considerable insight into the dipolar character of cubic zirconia, as we saw in Chapter 4. Our diffraction experiments as a function of dopant concentration will carry out a similarly systematic search for the crystallographic character and microstructure.

5.2 Theory

In this section we attempt to explain the electron diffraction behaviour of cubic stabilized zirconia (CSZ) as that of an orientational glass, with randomly-arranged (but crystallographically reorientable) microdomains playing the role of Potts-glass-like quadrupoles as explained in Chapter 3. The microdomains are embedded coherently in the cubic matrix (as described in the Allpress-Rossell model), interacting via random elastic "exchange" (Gross et al., 1985). A few nanometers across, these reorientable "defect" species are so strongly coupled elastically to the cubic matrix as to display collective behaviour characteristic of structural (conventional) glasses. In Chapter 4 we

demonstrated the typical frozen, supercooling and mobile regimes of a glassy CSZ specimen in simple dilatometer experiments   We link observed "critical points" to recent published observations on the mechanical (Morscher et al., 1991; Baufeld et al., 1995), diffraction (Martin et al., 1993; Proffen et al., 1993; Welberry et al., 1994; Hull et al., 1988; Rossell et al., 1991) and transport (Badwal and Swain, 1985; Fischer, 1993) properties of CSZ and structural glasses.

The microdomains (in Ca-CSZ, at least, where correspondence between structure and diffraction is most clear-cut) are reconstructively reorientable Potts-like mesoscopic rotors, able to orient their crystallographically unique monoclinic axis in any of the six distinct ⟨110⟩ directions of the strained cubic host.   The static version of our model for Ca-CSZ then, is that of a dilute, deformable, six-state orientational glass (Vollmayr et al., 1991) as explained in Chapter 3.   Except for this crystallographically-constrained orientability facilitated by short-range diffusion of dopant cations in the microdomains, the model bears some resemblance to several other domain or cluster models of structural glasses and glassy ionic conductors (Goodman, 1975; Ingram et al., 1988; Stillinger, 1988; Kirkpatrick, 1989).   Although the rotor's crystallographically unique axes may rotate through large angles, the displacement of individual atoms in the microdomains is small. The energy difference between a ϕ_1 microdomain and an equivalent volume of disordered "parent" phase through which it may transform ferroelastically during axis reorientation is very low (Dwivedi and Cormack, 1990).   We expect other zirconias to behave similarly and not to depend too greatly on the details of rotor interaction near phase transformations (Grannan et al., 1990): i.e., to belong to the same universality class.

As outlined in Chapter 3, in the Ca-CSZ case, the interaction between the ϕ_1 rotors may be modeled on a random array of frustrated elastic quadrupoles interacting via elastic exchange, in which pair-wise configurations in the form of antiferroelastic "tees" are found to predominate at low temperatures (Grannan et al., 1990): i.e., the unique axis of one of

a pair of ϕ_1 rotors will tend to align itself parallel to a line joining their centres, while another will align perpendicular to the line, with the unique axes of both pointing along $\langle 110 \rangle$ -type cubic directions. The pair-wise configuration of the rotors results in a disordered locally tetragonal strain in the cubic matrix (Vollmayr et al., 1991), which , when the system is in the supercooling or completely glassy frozen state, will produce the "forbidden" $\overline{1}12$ -type diffuse diffraction spots characteristic of CSZ at low temperatures. These extra diffuse spots are the source of the "tetragonal" reflections in powder neutron diffraction patterns of Ca-CSZ (Martin et al., 1993; Proffen et al., 1993) and the source of the t" phase described recently as being "tetragonal without tetragonality" (Yashima et al., 1994) in Y-CSZ and the cause of considerable confusion in the diffraction characterization of many zirconia alloys, since other modifications (e.g., rhombohedral, orthorhombic) are also possible, depending on the thermomechanical preparation of the specimen (Martin et al., 1993; Hull et al., 1988; Vollmayr et al., 1991). In large Ca-CSZ single crystals the diffuse tetragonal spots often go undetected due to random local strain fields arising from matrix-microdomain unit cell mismatch (Grannan et al, 1990). The strain is released in Ca-CSZ powders and the effect is anyway small in the Y-CSZ case, for both powders and single crystals.

5.3   Experimental Details

The experiments were carried out in a Philips CM20 electron microscope operating at 200 kV and equipped with a GATAN double-tilt heating stage borrowed from the CSIRO. The YSZ specimens examined are all single crystals of supplied by ZIRMAT (Massachusetts USA) prepared by the skull-melting method.   Similarly, the CaSZ specimens were all prepared by Hrand Djevahirdjian (Monthey, Switzerland). The EM specimens were cut by a diamond saw and thinned in a GATAN ion-beam thinner to thickness suitable for EM examination. The nominal dopant concentrations are 9.5, 12, 15, 18, 24 mole% for YSZ, and calcium-doped samples with molar CaO concentrations of 12.0% and 14.6%.

Most of the diffraction experiments were conducted at room temperature, although a small number were conducted at higher temperatures up to 1000°C, in order to test the predictions of the theory, which we sketch below.

5.4   Experimental Results

The electron micrographs in the following pages represent the experimental results of this chapter. They are of three types.

(i)   Room-temperature concentration series of Y-CSZ.

(ii)   High-temperature micrographs of Y-CSZ

(iii)   Room-temperature patterns of Ca-CSZ.

Our aim is to describe the various types of contrast visible in the patterns and examine how the contrast changes with concentration, and in some cases with temperature. In line with the Allpress-Rossell model, we consider that an increase in dopant corresponds to an increase in ϕ_1-like rotor concentration and a corresponding decrease in the cubic/tetragonal ZrO_2 matrix material.

The main types of contrast are:

(i)   Bragg spots: strong scatter from the average lattice.

(ii)   The extra $\bar{1}12$ tetragonal superlattice reflections visible in [110] and [111] axis-oriented diffraction patterns.

(iii)   Characteristic circular diffraction rings in [112] projections.

(iv)   Bow-tie-shaped diffuse scatter visible in [110] projections.

(v)   Hexagonally arrayed mushroom-shaped diffuse scatter radiating from the $2\bar{2}0$ Bragg diffraction spots in $\langle 111 \rangle$ projections.

(vi)   Broad diffuse streaks between 002 and 020 diffraction spots and the reciprocal space origin 000 spot in $\langle 100 \rangle$ projections.

(vii)   Fine streaks of diffuse contrast of circular or lemniscate shape, visible in several projections.

The origins of several of these different types of contrast are already reasonably well understood and have been referred to in the literature review (Chapter 2), and as outlined below.

Comments

(a)   The strong f.c.c.-type Bragg spots are what are expected from an alloy whose average structure is the fluorite structure.   We do not expect the appearance of these spots to change much with yttria concentration and to change little with the temperatures available in our experiments.

(b)   The striking characteristic rings of diffuse scatter in the $\langle 112 \rangle$ projections of CSZ alloys with various dopants: Miida et al (1994), Withers et al (1991) have described the ring contrast in terms of the microdomains found in CSZ.   Hence, if the microdomains indeed contain the dopant cations as suggested by Allpress-Rossell model, the relative intensity of the rings should increase with dopant concentration.

(c)   The mushroom-shaped diffuse scatter in $\langle 11i \rangle$ projection diffraction patterns and the bow-tie-shaped diffuse scatter are attributable to the microdomains and therefore should grow brighter and clearer as the concentration of dopant increases.

(d)   The fine complex patterns (circles, lemniscates, ellipses, etc.) found in several projections have been attributed to Huang-type scatter by Chaim and Brandon (1984) and attributed to defects with trigonal symmetry, which may be considered as part of the complex structure (but not the whole of the structure) of microdomain constituents like ϕ_1. Their appearance is indicative of cation disorder.

(e)   Perhaps the most puzzling aspects of the diffraction patterns of CSZ is the appearance (at low dopant levels) of a "superlattice" of small diffuse spots corresponding to tetragonal symmetry. Miida et al (1994) have conducted tilting experiments of Y-CSZ specimens in the electron microscope, revealing that most of the tetragonal spots are due to double diffraction from a small set of essential tetragonal spots with index $\overline{11}2$ and its five equivalents. We shall pay particular attention to those spots in what follows.

(f)   Finally, it should be remarked that few commentators have deduced definite attribution to any particular lattice defect for the case (vi) of the broad, cross-shaped diffuse scatter, found in $\langle 100 \rangle$ projections.   This contrast emerges with relative clarity in electron diffraction because of the great sensitivity to symmetry breaking that its strongly dynamical character allows. It will prove to be of crucial importance in our interpretation of the diffraction patterns in terms of the microdomains and is intimately linked to the interpretation of the $\overline{11}2$ -type tetragonal diffraction spots.

Each of the following sets of micrographs consists of diffraction patterns form single-crystal Y-CSZ specimens in the [111], [110], [112], and [100] projections, with the Y_2O_3 dopant concentration constant for each set: the set of four shots is usually taken from the same ion-beam-thinned crystal.   The temperature is room temperature unless otherwise stated. We now follow the changes observed in the different types of diffuse scatter,

paying particular attention to which types grow (and which fade) with change in dopant concentration.

9.5 mole% Y_2O_3 doping level (YCZ-9.5)

This is the least-heavily doped of our commercially available crystals. We consider (following Allpress and Rossell, 1975) that as dopant is added , the microdomains grow in number but not in size, i.e., that diffuse diffraction due to the microdomains intensifies but need not become any narrower in reciprocal space. Hence, the [112] projection rings are very faint at this concentration, which is near the lower limit of cubic stabilization (8 mole % Y_2O_3).

The [111] "mushrooms" and [110] "bow-ties" do not emerge clearly at this concentration, but there is clear evidence for the $\overline{1}12$ family of "tetragonal superlattice" spots in the [111] and [110] projection diffraction patterns. As we shall see this is evidence that the $\overline{1}12$ - type spots do not originate directly form the microdomains themselves but from the background of tetragonally distorted cubic material. The [100] projection diffraction pattern reveals little complicated diffuse scatter and no trace of $\overline{1}12$ -type tetragonal spots. It does, however, show a faint but discernible cross-shaped pattern of broad diffuse scatter which does not extend very far past the 020 or 002 spots.

12 mole% Y_2O_3 doping level (YSZ-12)

The [112] projection "rings" become much more pronounced and the [110] bow-ties now appear: the [111] projection diffraction pattern appears to have developed diffuse streak contrast between the $2\overline{2}0$ -type diffraction spots but this is due to the development of the hexagonal streaks emerging from the spots.

In between the hexagonal streaks (the precursors, as we shall see, of mushroom-shaped contrast at higher dopant concentrations) faint $\bar{1}\bar{1}2$-family spots are still visible in the $[1\bar{1}\bar{1}]$projection at this concentration, evidence for the fact these "superlattice spots" are not due to remnant tetragonal precipitates as is sometimes suggested, since at 12 mole% Y_2O_3 we are now completely in the single-phase cubic region, well clear of the cubic/tetragonal two-phase region according to any reliable phase diagram. Our high-temperature experiments will be conducted on 12 % specimens for this reason.

The $\bar{1}\bar{1}2$-type superlattice spots formerly plainly visible at 9.5 mole% Y_2O_3 which sat at the intersection of the very faint "bow-ties" in [110] patterns at that concentration are now very faint and diffuse, whereas the "bow-ties" are much clearer. This appears to indicate that the "superlattice" vanishes as dopant concentration increases, again identifying the cubic/tetragonal matrix as the source of the "superlattice" scatter and that the "bow-ties" contrast originates from the microdomains, since it increases with dopant concentration. The cross-shaped diffuse contrast visible in the 9.5 mole% Y_2O_3 specimen is seen to increase in intensity in the 12 mole% diffraction pattern, suggesting its origin as scatter from the microdomains. It should be pointed out that due to the dynamical (multiple-scattering) character of electron diffraction, direct comparison of contrast levels in diffraction patters from specimens of differing thickness is difficult. In a given projection, similarity in brightness of the Bragg spots might be a guide to the direct comparability of diffuse contrast between concentrations or temperatures, but features can be lost from the micrograph if the exposure is not long enough. In the [111] projection diffraction pattern for 12 mole% Y_2O_3 , for example, the Bragg spots are very bright due to a long electron microscope exposure for the purpose of demonstrating the persistence of the $\bar{2}11$ family of superlattice spots.

As seen in the [111] projection diffraction pattern of the 12 mole% Y_2O_3 CSZ set, this long exposure has also revealed the otherwise very weak ring-shaped features, now visible in the center of triangular regions between spots. In [111] projections at specimens of the

other concentrations, these ring features are vestigially visible in the pattern, but may be brought out only by optical over-exposure.

15 mole% Y₂O₃ doping level (YSZ-15)

The $\bar{2}11$-type superlattice spots have now vanished from the [111] and [110] projection diffraction patterns. The [112] "smoke-rings" persist. The hexagonal "mushroom" shape is now clearly radiating from the $2\bar{2}0$-type spots in the [111] projection and the "bow-ties" have brightened, sharpening up to some extent as well. In the [100] projection, the cross-shaped diffuse streaks appear to have brightened and broadened again, with streaks now visible on rows parallel to [010] and [001] directions.

18 mole% Y₂O₃ doping level (YSZ-18)

The hexagonal-arrayed "mushroom" diffuse contrasts in the [111] projection persists at 18 mole% Y₂O₃, as does the "smoke-ring" contrast in the [112] projection, in which some continuous diffuse scatter has condensed into spots. The now almost continuous "bow-ties" are similar in appearance to the 15 mole% case and there is no sign of any "superlattice" spots. The cross-shaped pattern is similar to that at 15 mole %.

24 mole% Y₂O₃ doping level (YSZ-24)

The [112] patterns appear sharp: "radial" diffuse scattering similar to the "mushroom" now appears around other spots further out in the [111] diffraction pattern. The [110] projection diffuse scatter has broken up into an almost continuous chain-link structure along the [$\bar{1}$11] direction. With comparable tilt and brightness of Bragg spots, the [100]

pattern now seems to have diffuse brightness diminished in comparison with the 18 mole% case.

Summaries (Yttria dopant series)

(i) The $\overline{2}11$-type superlattice is associated with the essentially dopant-free cubic/tetragonal matrix regions.

(ii) The "bow-ties" increase in brightness and definition with dopant additive and are therefore associated with the microdomains, which are considered to contain all the dopant.

(iii) The "mushrooms" appear to brighten and sharpen with added dopant and therefore arise from the microdomains.

(iv) In a similar way to (ii) and (iii) above, the "smoke-rings" are attributable to the microdomains.

Doping with Calcia

Similar investigations to the yttria-doped series above have been undertaken using ion-beam thinned single crystals of Ca-CSZ. Since 20 mole% CaO corresponds to the line phase ϕ_1 in the calcia-zirconia system, the two compositions 12 mole% CaO and 14.6 mole% CaO of the present study represent stabilized zirconia with relatively low dopant. The amount of ϕ_1 should only be slightly greater than half the total volume with a large amount of matrix cubic/tetragonal distorted ZrO_2 present. A correspondingly large amount of $\overline{2}11$-type superlattice diffraction is expected.

12 mole% CaO doping level (CaSZ-12)

Examining the set of four room-temperature micrographs from 12 mole% CaO, it is clear that all the diffraction phenomena found in the yttria dopant series are also found in the calcia series. The "bow-ties", "mushrooms" and "smoke rings" are all present and in the same relative positions as before. The $\overline{2}11$ family of superlattice diffraction spots are brighter and sharper than in the yttria dopant series and could no longer be mistaken for the central part of a "bow-ties" structure although the "bow-ties" diffuse scatter is also sharper than before. Quite generally, many of the diffuse scattering features for Ca-CSZ series are sharper than those of the Y-CSZ series. This is likely to attributable to the fact that Ca-CSZ domains (ϕ_1) are larger (~28Å, Rossell, Sellar and Wilson, 1991) than those of Y-CSZ (~ 10Å, according to Welberry et al., 1993). The [112] "smoke-rings" however are sharper, clearer, and larger than those from Y-CSZ. The [100] cross-shaped pattern is similar in brightness and structure to several of the yttria series.

14.6 mole% CaO doping level (CaSZ-14.6)

The "mushrooms", "bow-ties" and "smoke-rings" are all similar in this case to the previous 12 mole% CaO case. The $11\overline{2}$-type "superlattice" spots are still visible especially in the [110] projection, but the small very slim circles of contrast are no longer visible in the [111] projection. The [100] cross-shaped pattern is similar to the 12 mole% CaO case but may be slightly narrower. Some Huang scattering of the kind described by Chaim and Brandon (1984) are slightly more visible in this projection than for yttria or calcia-doped specimens of other concentrations.

Summaries (Calcia dopant series)

The overwhelming conclusion from both concentration series is that, with minor variations, the diffraction patterns of all concentrations of both dopants are the same, with an increase of dopant corresponding to an increase of rotor-microdomain (as evidenced by

the "mushrooms", "bow-ties" and "smoke-rings") and a decrease of dopant corresponding to an increase in volume of cubic/tetragonal pure ZrO_2 structural, giving rise to the $11\bar{2}$ family of superlattice reflections.

Importantly, the similarity between the diffuse scattering features of Y-CSZ and Ca-CSZ manifests that the microdomains in Ca-CSZ and Y-CSZ have similar orientations mesoscopically.

In the next section we interpret these observations in terms of the glassy model.

5.5   Discussion

In detail, we consider pair-wise stress-strain interactions between the microdomains, here modeled on ϕ_1 which possesses six distinct unique axes and, according to VKZ, conform to the requirements of a random array of reorientable, discrete six-state quadrupoles (As shown by similar diffuse scattering features of both Y-CSZ and Ca-CSZ above, ϕ_1 –like defects exist in Y-CSZ.   And in chapter 6, we attempt to discern the possible microdomains in Y-CSZ and their orientations).   Cubic symmetry restricts the form of all the couplings between quadrupoles.   There are only three independent elastic constants. The tensors corresponding to the extra stresses due to the uniaxial microdomains are denoted by $\underline{\sigma}^\mu$.   Since in a cubic lattice, the principal tensor axes for ϕ_1 correspond to the $\langle 110 \rangle$ directions, the tensor must be invariant against residual symmetry operations, i.e., rotations around the defect axis which leave the cube invariant (Vollmayr et al., 1991). Thus symmetry requirements reduce the extra stress tensor due to a ϕ_1-like microdomain to following form, as reported in chapter 3.

(I)   Defect axes parallel to [001]

5-12

$$
\begin{bmatrix}
\sigma_0 + 2\sigma_L & 0 & 0 \\
0 & \sigma_0 - \sigma_L & \sigma_T \\
0 & \sigma_T & \sigma_0 - \sigma_L
\end{bmatrix}
$$

where σ_0 is the isotropic hydrostatic pressure component: subtracting this term, $\underline{\sigma}^u$ assumes the form

$$
\begin{bmatrix}
2\sigma_L & & \\
& -\sigma_L & -\sigma_T \\
& -\sigma_T & -\sigma_L
\end{bmatrix}
$$

(II)   Defect axes parallel to $[0\bar{1}1]$

For a defect axis parallel to $[0\bar{1}1]$, with isotropic term removed, the local stress tensor takes the form

$$
\begin{bmatrix}
2\sigma_L & & \\
& -\sigma_L & -\sigma_T \\
& -\sigma_T & -\sigma_L
\end{bmatrix}
$$

If two neighboring domains are of axis orientation $[0\bar{1}1]$ and $[011]$ (mutually orthogonal as in the Sethna-type "tee" configuration,), the resultant stress in the "domain walls", consisting of disordered cubic ZrO_2 will be proportional to the sum of the superimposed stresses due to the two neighboring microdomains, to within a certain approximation. That is, it will be of the form

$$
\begin{bmatrix}
2\sigma & & \\
& -\sigma & \\
& & -\sigma
\end{bmatrix}
$$

i.e. the resultant stress in the "cubic" walls is of the form of a $\langle 100 \rangle$ type stress: this is the source of the local tetragonality, which yields no bulk tetragonallity if averaged randomly over interacting pairs of domains. Local cubic symmetry is randomly broken by the resultant normal stresses in the regions between pairs of domains. Small regions of orthogonal atomic {100} planes are hence shifted randomly away from the atomic planes of the average (cubic) lattice with displacements in the ratio 2:1:1, so diffuse diffraction spots are found in the forbidden $\overline{2}11$-type Bragg reflecting positions when the CSZ sample is below the glass transition temperature and the pairs of domains are frozen into "tee" configurations. This then, is an approximate derivation of the "tetragonal without tetragonality" found near room temperature in CSZ samples with low stabilizer doping. The frozen-in tees also explain another hitherto-unexplained diffraction phenomenon reported in this electron diffraction experimental section. As the concentration of dopant increases up to around 18 mole % Y_2O_3, cross-shaped diffuse streaks appear between diffraction spots of electron diffraction in each of the $\langle 100 \rangle$ family of projections. As the dopant increases, so does the intensity of the streaks relative to the Bragg spots from average lattice. As pointed out earlier, this appears to indicate that the diffuse streaks correlate strongly with the presence of dopant. In the light of Sethna's planar tee-shaped configuration concept in the frozen state, we take our interpretation of the cross-shaped diffuse streaks one step further: since all the dopant is considered to reside in the microdomains, it seems reasonable to claim that the $\langle 100 \rangle$ streaks are due chiefly to planar arrays of mutually orthogonal domains, the size of which is limited by frustration effects. Judging by the width of the diffuse streaks in the diffraction pattern their spatial extent is typically 50 Å, the size of two microdomains of average size and separation. Their effect on the diffraction pattern then is somewhat like that of Guinier-Preston zones but of much smaller size. The effect of these tee-domains on the mechanical properties of zirconia alloys has recently been described by Baufeld et al. (1995), without reference to the structure or paired character of the defect.

Temperature dependence of the $1\bar{1}\bar{2}$-type diffraction spots

In the final montage of three separate electron micrographs, we present evidence for the disappearance of the $1\bar{1}\bar{2}$-type electron diffraction spots at temperatures above T_m, the glassy "melting point" for the material. The microdomains are considered to be sufficiently uncoupled at these temperatures that the tetragonal matrix $1\bar{1}2$ reflections no longer suggest a non-zero value for the Edwards-Anderson order parameter.

The specimen is an ion-beam-thinned 3 mm sample of single crystal 12 mole% Y_2O_3-ZrO_2, so as to be clear of the "equilibrium" cubic-tetragonal two-phase region of the phase diagram. The montage represent a "before" (room temperature) - 1000°C - "after" (room temperature) sequence of diffraction patterns taken of the same specimen in the [111] projection. The intensities of the main $02\bar{2}$-type Bragg beams between which the $1\bar{1}2$-type diffuse spots appear are roughly comparable in such of the three shots, so that valid comparisons of $1\bar{1}2$ spot intensities can be drawn. The specimen is tilted slightly away from the axis.

The initial room temperature micrograph exhibits small, dim $1\bar{1}2$-type reflections between pairs of the $02\bar{2}$-type Bragg spots and between the hexagonally-radiating broad diffuse lines emanating from each of the $02\bar{2}$-type spots which become mushroom-like at higher concentrations. The second micrograph of the montage shows the apparent lack of any $1\bar{1}2$-type spots between the $02\bar{2}$-type Bragg peaks at a temperature near 1000°C, signaling a zero-value for the Edwards-Anderson order parameter. The hexagonally arrayed linear diffuse scatter has also vanished almost entirely, which may suggest a link between the two types of scatter; one scatter attributable to the domains themselves and the other due to the matrix cubic zirconia between the domains (see next chapter).

The third micrograph shows the contrast from the specimen after returning to room temperature. Although relative intensities are often difficult to compare in electron micrographs and despite the somewhat more "ragged" overall appearance of the third diffraction pattern, it is reasonably clear that the $1\bar{1}2$-type spots have returned as well as

the hexagonally radiating linear diffuse contrast, demonstrating a certain degree of reversibility.

5.6   Conclusion

We have conducted concentration series and temperature series on single-crystal, ion-beam thinned samples of Y-CSZ. The concentration series serves to identify which diffuse diffraction features are attributable to the microdomains and which to the tetragonally-distorted cubic regions between the microdomains. Under the Allpress-Rossell model, where essentially all the dopant goes into the microdomain, an intensification of the brightness of a given diffuse diffraction feature with concentration would appear to indicate that the feature arises due to scatter from the microdomains.

Thus, the "bow-ties", "mushrooms" and "smoke-rings" can be attributed to the microdomains from our concentration series (9.5 to 24 mole% Y_2O_3). The "cross-shaped" diffuse scatter was shown to arise from the antiferroelastic pairing of the reorientable elastic defects on $\{100\}$ planes, making it seem as if the planes were disordered by these random pair-wise couplings at low temperature. Probably the most important result is that an increase in dopant causes a decrease in the brightness of the "forbidden" $1\bar{1}2$ -type tetragonal diffuse spots. This suggests that they arise from the distorted cubic material between the domains, with the superposed stresses from the adjacent domains (considered as reconstructively reorientable defects) imparting a net local tetragonal distortion to the cubic matrix at low temperature, with small regions of $\langle 1\bar{1}2 \rangle$ –oriented planes diffracting randomly and independently, resulting in no net distortion overall.

Limiting our experiments to one concentration value, considered to reside solely in the "equilibrium" cubic phase (12 mole% Y_2O_3), we demonstrated that above about $1000°C$, in excess of the temperature T_m, the $1\bar{1}2$ spots vanish, indicating the arrest of the cubic region by the microdomains has ceased, with a low value for the Edwards-Anderson order parameter for the reorientable defects (domains).

[100]

02̄2   002   022
02̄0   000   020
02̄2̄   002̄   022̄

[111]

2̄02   02̄2
1̄1̄2
2̄11   1̄01   01̄1   12̄1
2̄20   1̄10   11̄0   22̄0
1̄21̄   011̄   101̄   21̄1̄
022̄   112̄   202̄

[110]

002
1̄12   11̄2
1̄11   001   11̄1
2̄20   22̄0
1̄11̄   001̄   11̄1̄
1̄12̄   002̄   11̄2̄

[112]
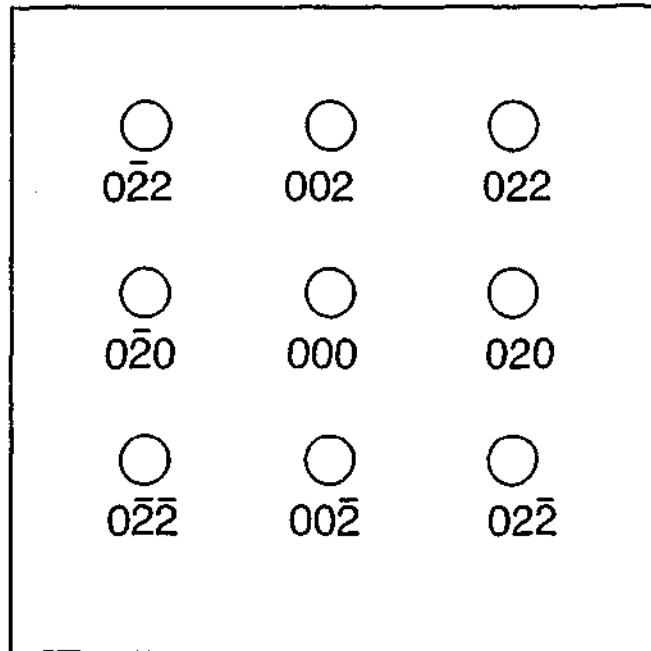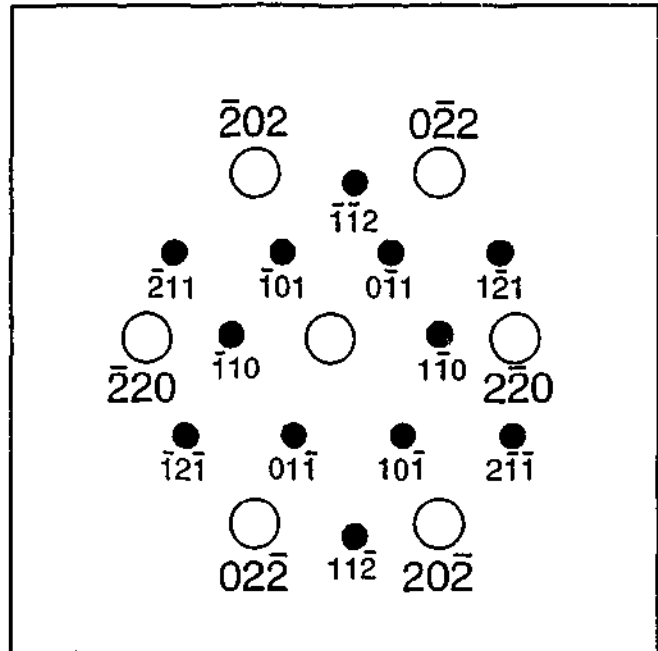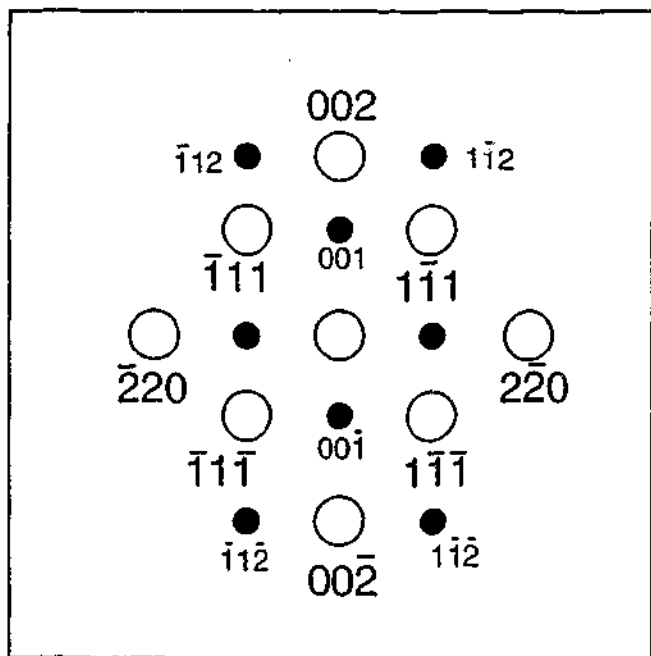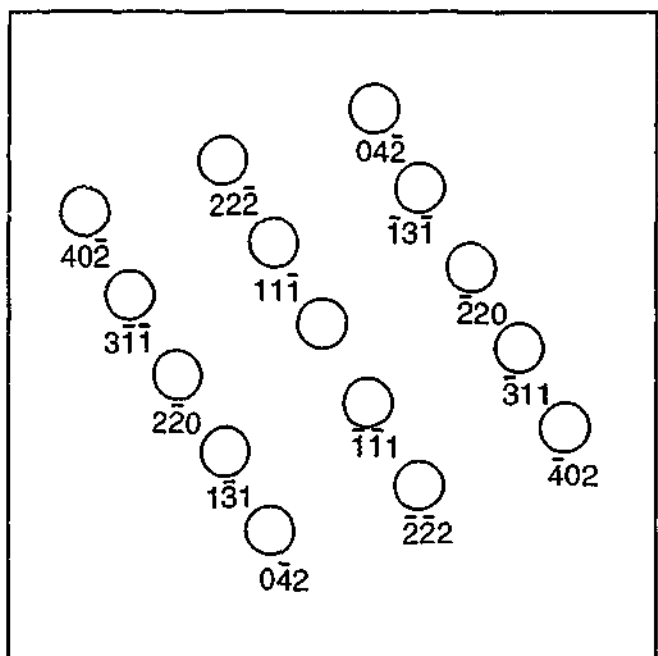
042̄
22̄2̄   1̄31̄
402̄   111̄   2̄20
311̄
2̄20   1̄11
131̄   2̄2̄2   3̄11
042̄   4̄02

YSZ - 9.5
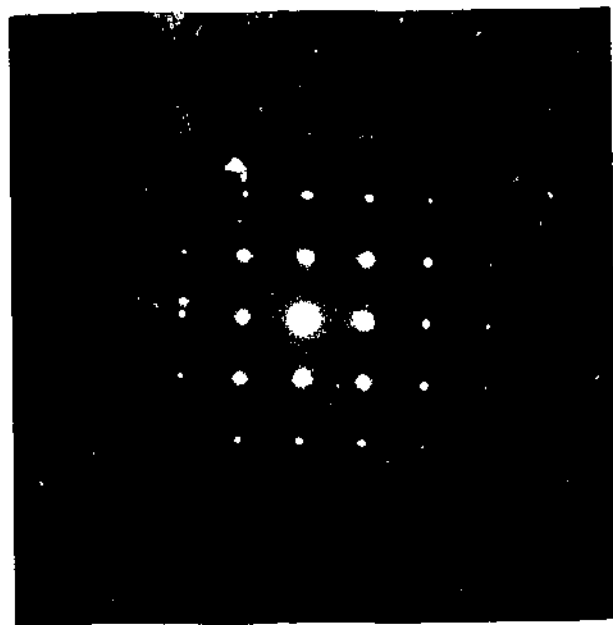
[100]
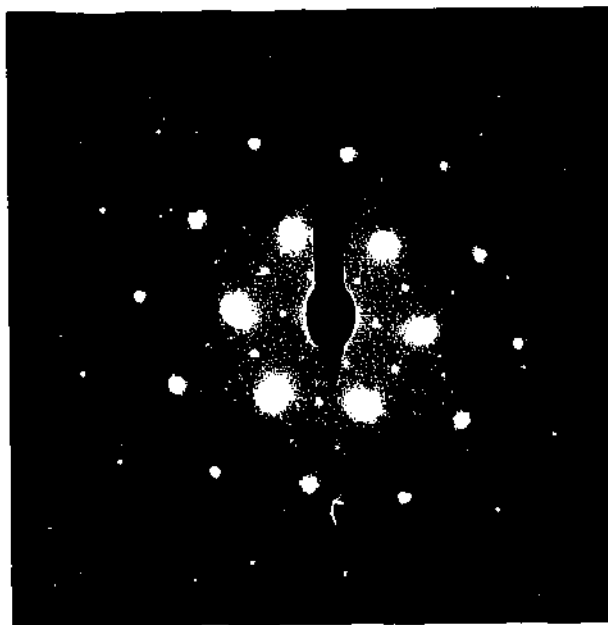
[111]
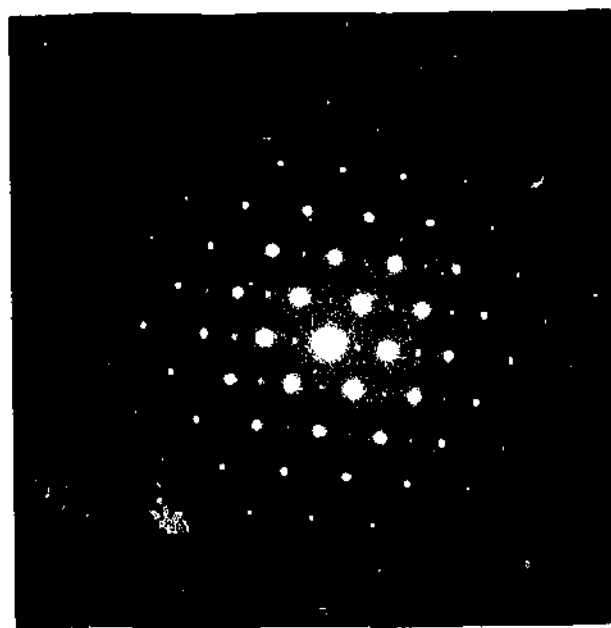
[110]
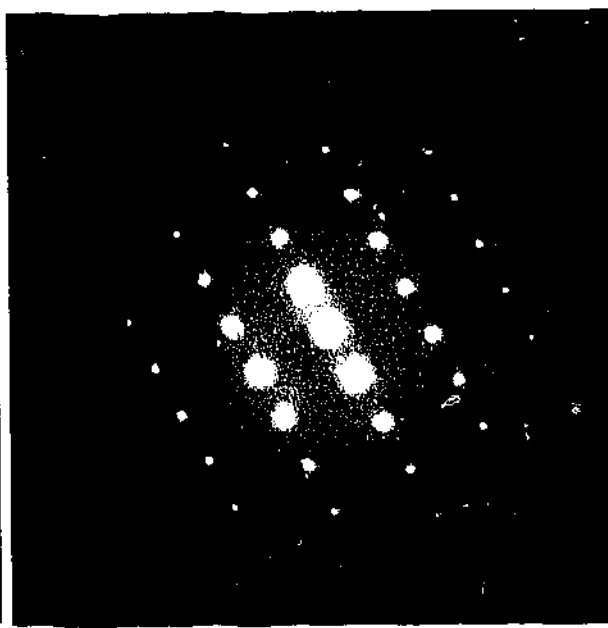
[112]
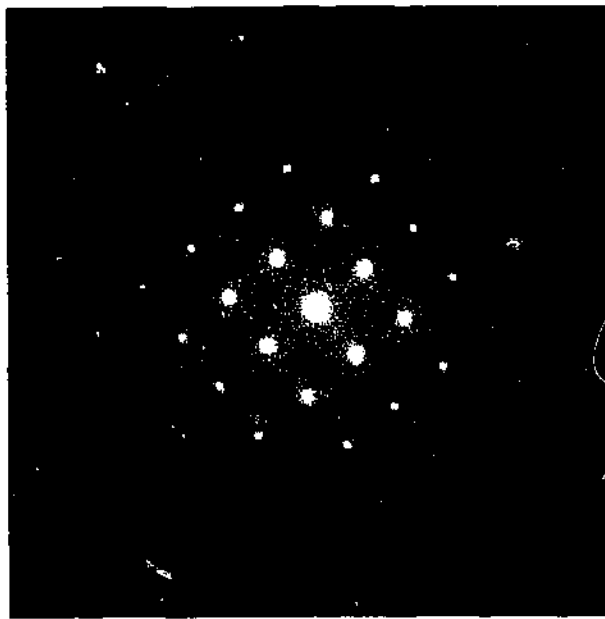
YSZ - 12

[100]
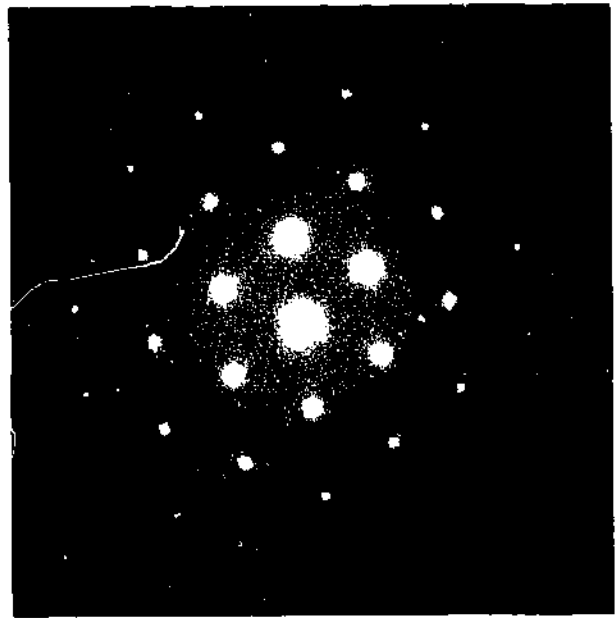
[111]
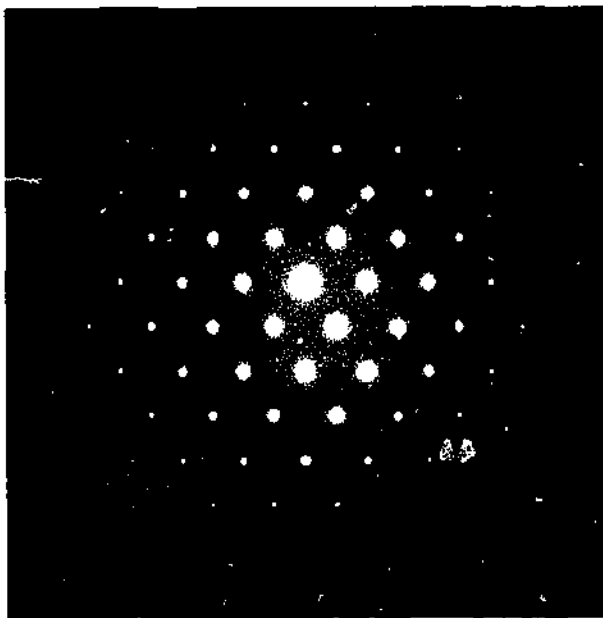
[110]
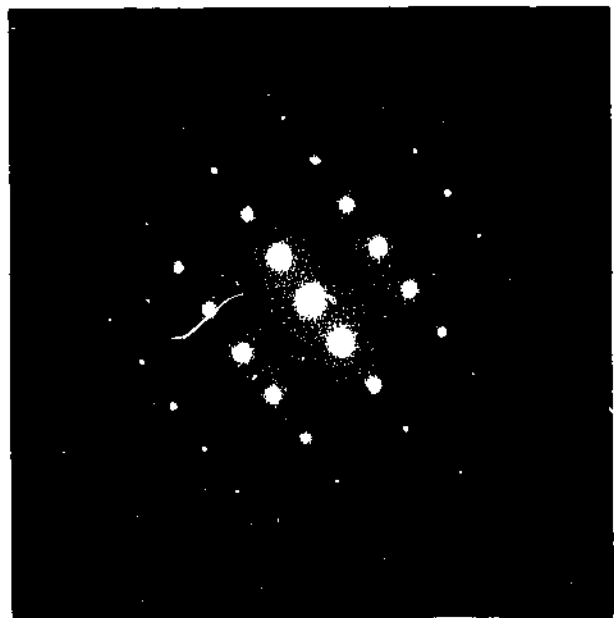
[112]

YSZ - 15
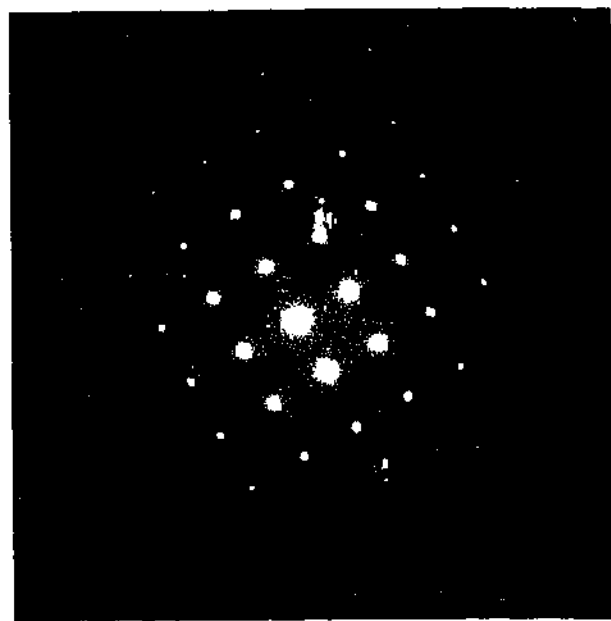
[100]
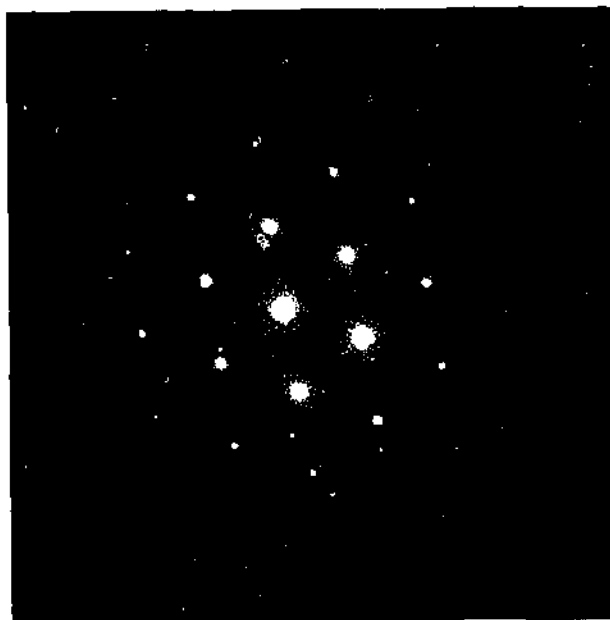
[111]
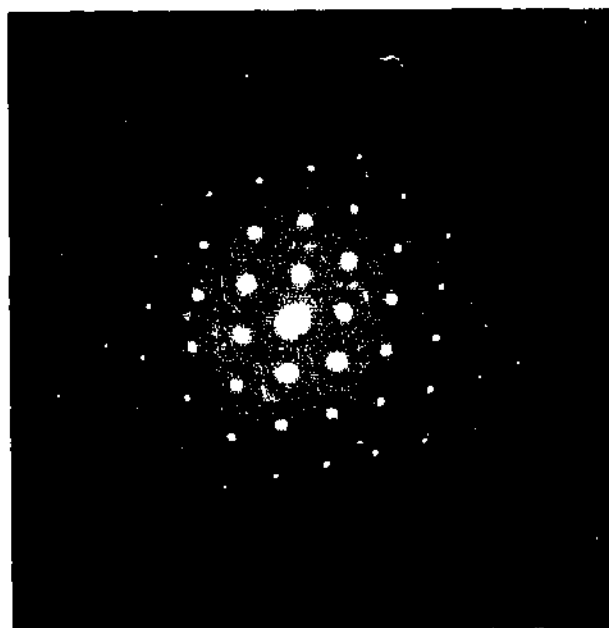
[110]
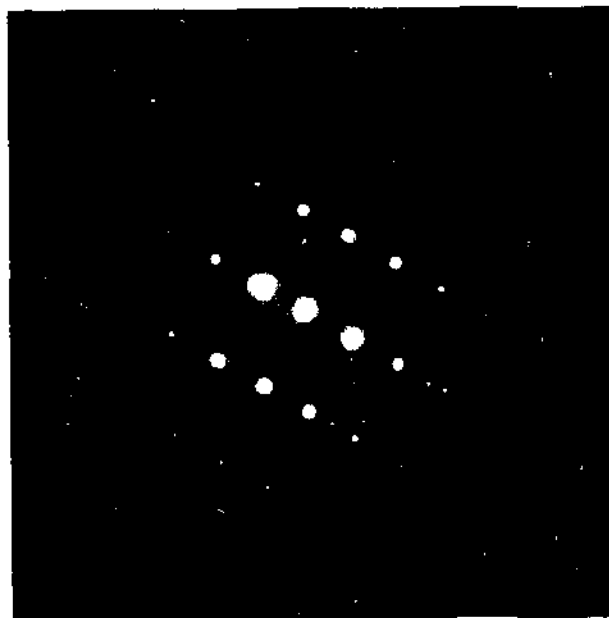
[112]

YSZ - 18
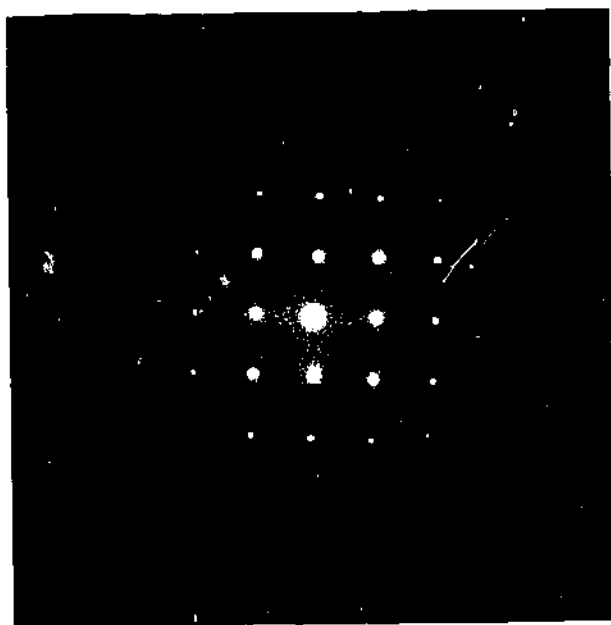

[100]

[111]
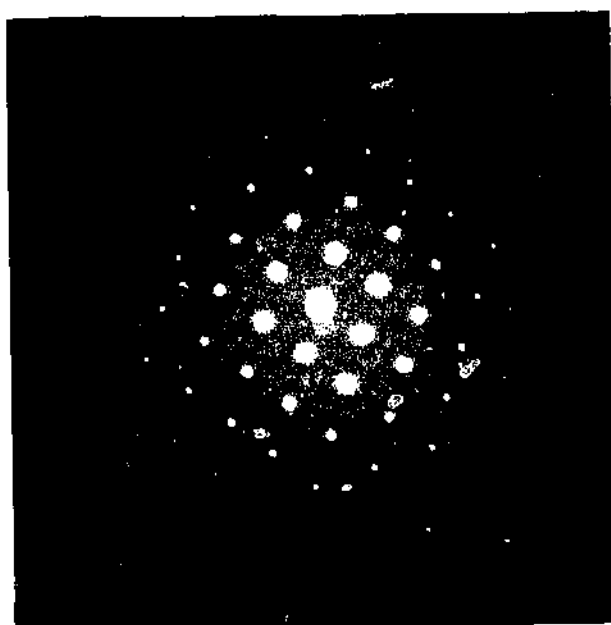
[110]

[112]

YSZ - 24
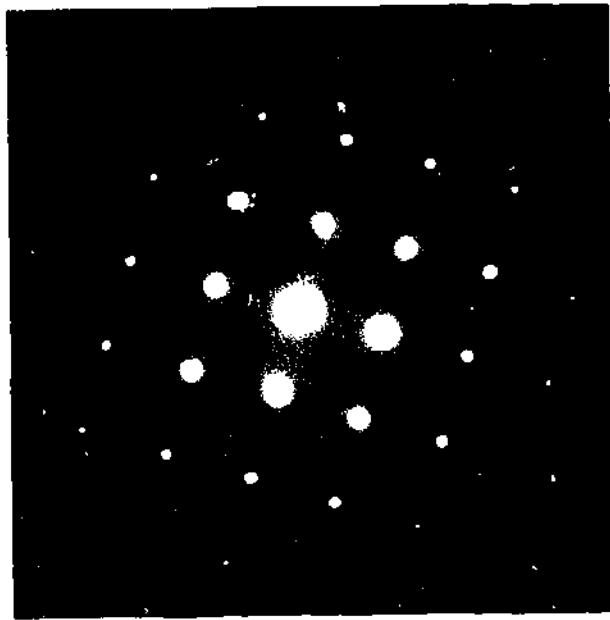
[100]
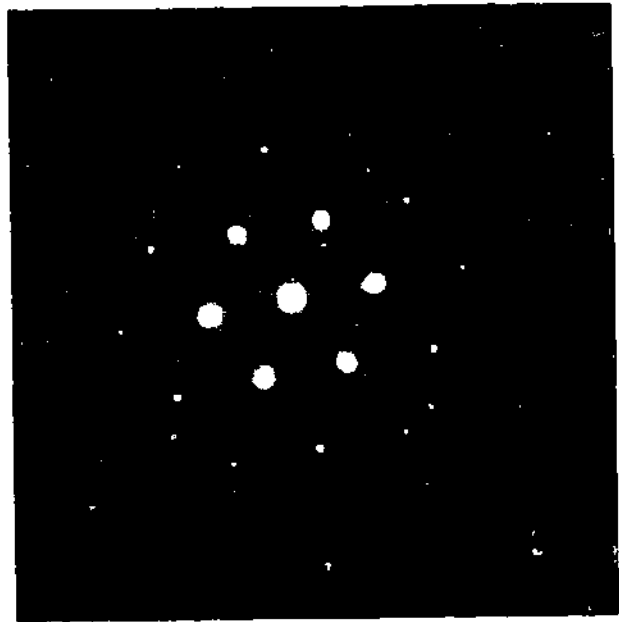
[111]
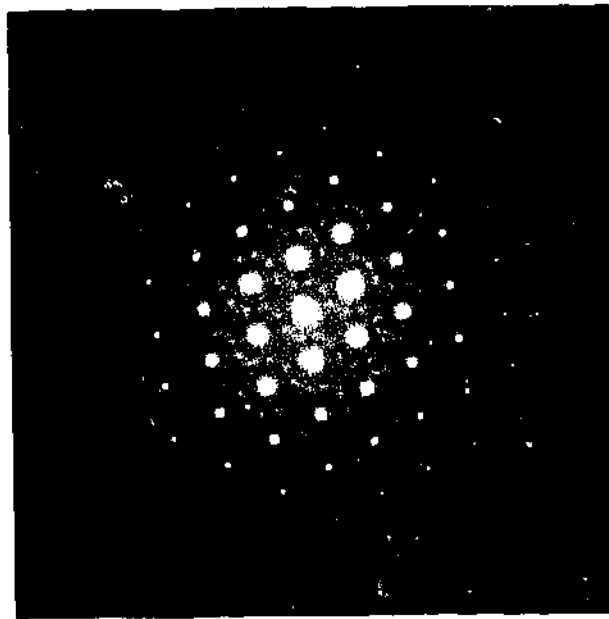
[110]
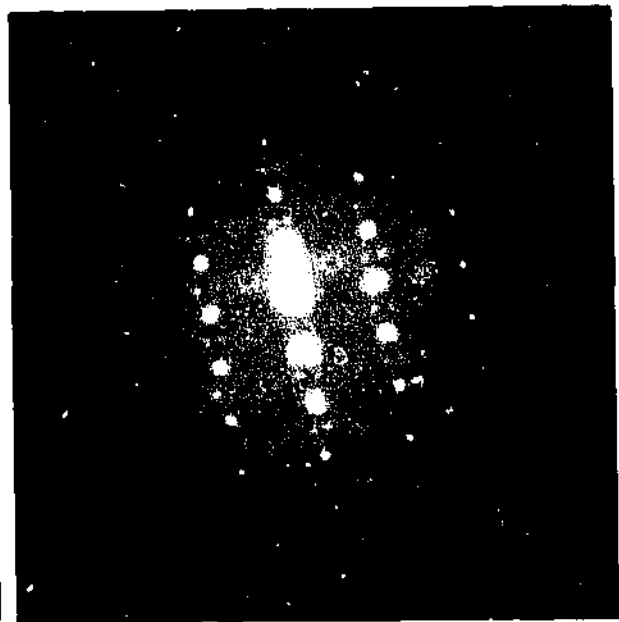
[112]

CaSZ - 12
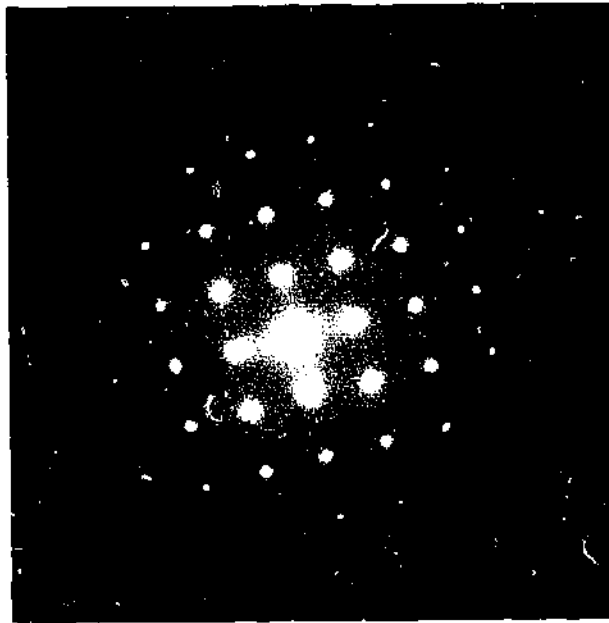

[100]
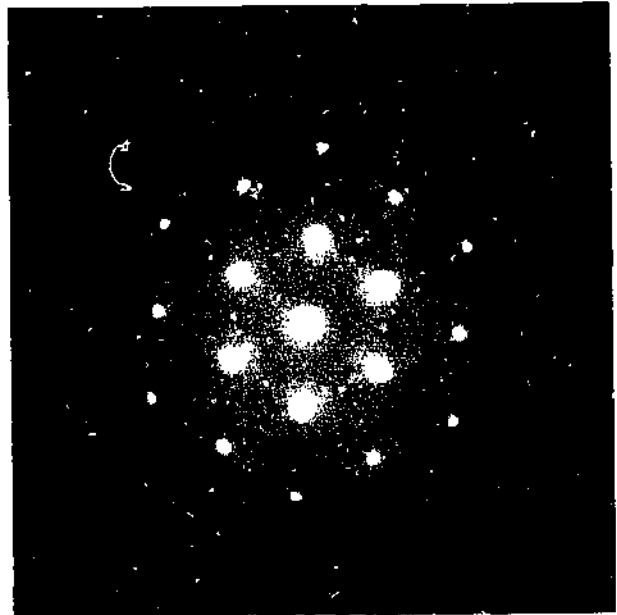
[111]
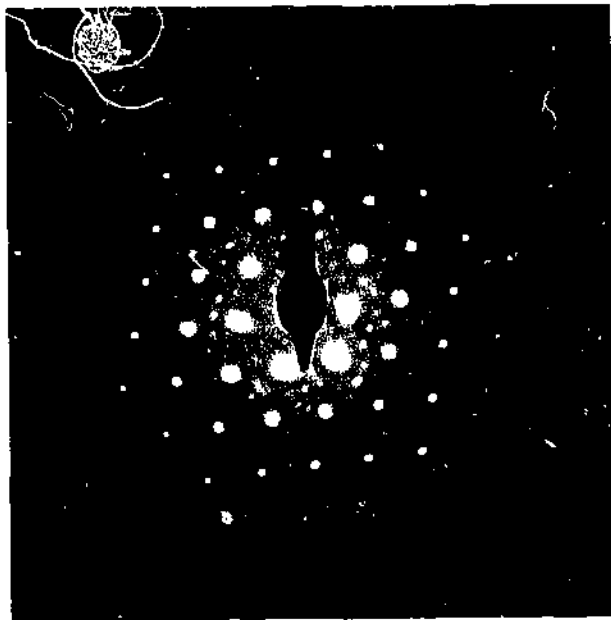
[110]

[112]

CaSZ - 14.6
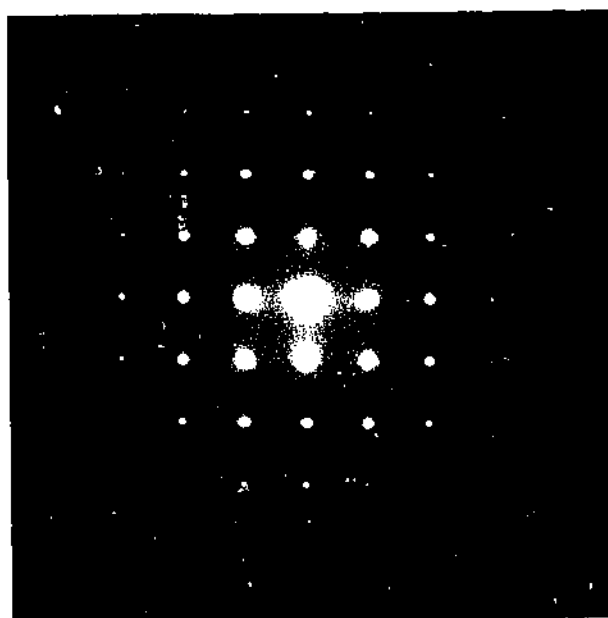
[100]
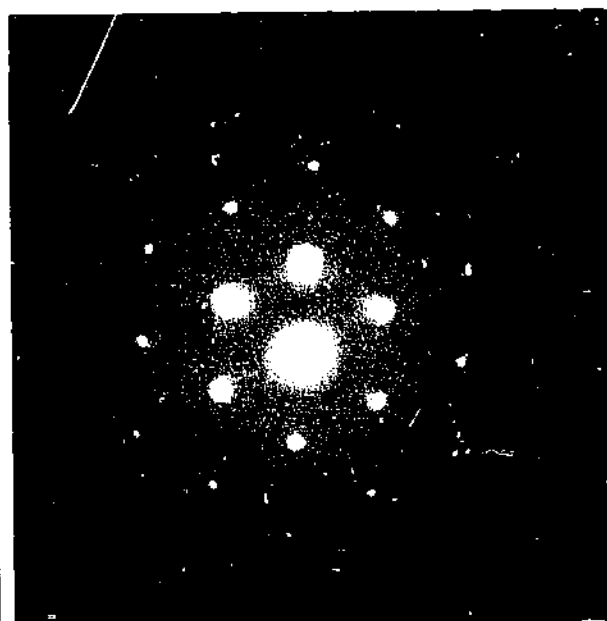
[111]
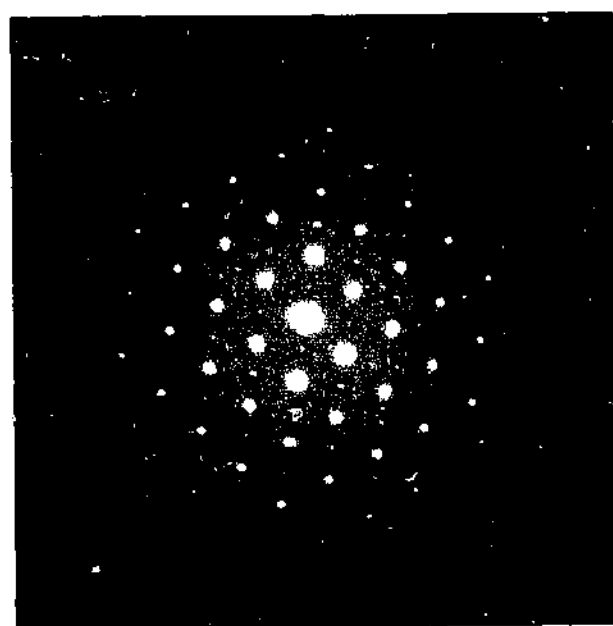
[110]

[112]
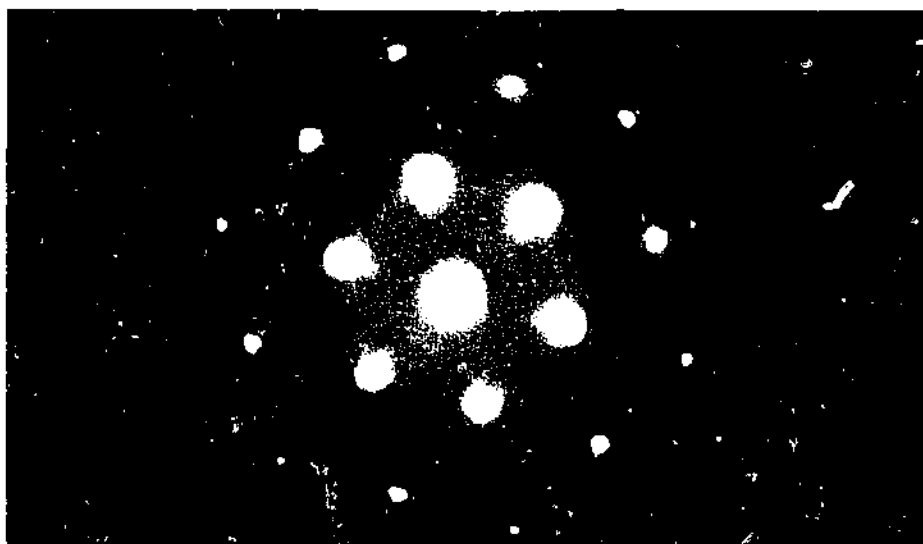
YSZ-12 at room temperature before heating. Note dim 1$\bar{1}$2-type spots between the Bragg 220 family.
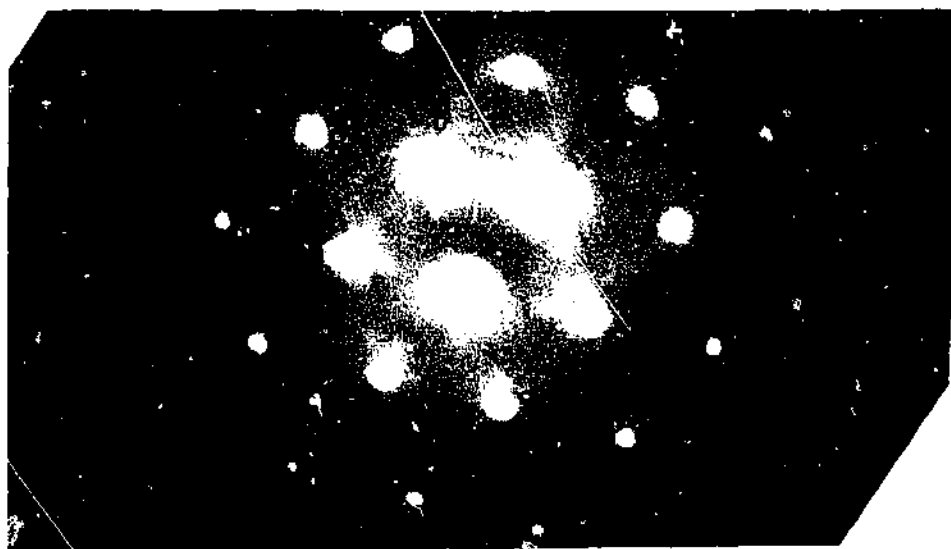
YSZ-12 near 1000°C. Note absence of 1$\bar{1}$2-type spots.
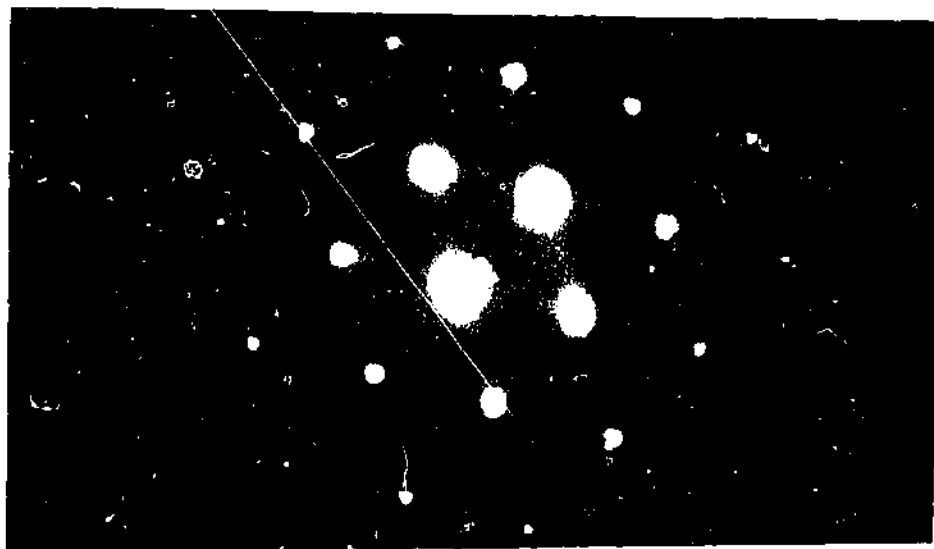
YSZ-12 at room temperature after 1000°C excursion. Note the return of 'forbidden' spots.

CHAPTER 6

X-RAY DIFFRACTION INVESTIGATIONS OF YTTRIA-STABILISED ZIRCONIAS

6.1 Introduction

Among CSZ components stabilized by various aliovalent cations, yttria-stabilised zirconia has been used most as the oxygen ion conductors in applications such as oxygen sensors, fuel cells, etc. because of its higher ionic conductivity, good mechanical strength, and relatively high resistance to aging effect. The defect structure in yttria-stabilised zirconia has long been a very interesting research topic. As we mentioned in the previous chapters, a great deal of research work has convinced people that the defect structure in stabilised zirconia alloys mainly consists of relaxations around oxygen vacancies and short-range order of oxygen vacancies/oxygen ions or vacancy clusters (Andersen et al., 1986; Osborn et al., 1986; Hackett, 1987; Neder et al., 1990; Welberry et al., 1993, Dai et al., 1996)). It is believed in general that anion ordering does not necessarily imply cation ordering, but cation order implies anion order (Rossell, 1984). A question arises. Is there any dopant cation ordering involved in the defect structure scene in yttria stabilised zirconia alloy? An answer to this question is quite rare or controversial. For example, among the researchers who attempted to answer the question, some believe that dopant cations are the next neighbour of oxygen vacancies (Steele and Fender, 1974; Tuller et al., 1987), some believe that the host cations are the next neighbour of the vacancies (Li et al., 1993), while others ignore any ordering in cation lattice (Dai et al., 1996; Welberry et al., 1993). It seems that more knowledge has been gained about the anion lattice than that about the cation lattice. One of the main reasons is that it is very difficult to distinguish the host cations from the dopant cations by electron, neutron, and x-ray diffraction, because Y (Z=39) and Zr (Z=40) have indistinguishable scattering factors (Welberry et al., 1992; Dai et al, 1996).

When the absorption edge of an atom in a material is close to the wavelength of the incident x-rays, the scattering factor of the atom changes drastically. The K-absorption

edges and characteristic radiations for Y, Zr, Cu, and Mo extracted from International Tables for Crystallography are listed in table 6.1.

Table 6.1 Wavelength of K-emission series and absorption edges in Å

Z	Element	$K\alpha_1$	$K\alpha_2$	$K\beta_1$	$K\beta_2$	K-absorption edge
26	Cu	1.54090	1.54474	1.39242		
39	Y	0.82879	0.83300	0.74068	0.72874	0.72762
40	Zr	0.78588	0.7901	0.70170	0.68989	0.68877
42	Mo	0.70926	0.713543	0.632253	0.62099	0.61977

It can be seen that the wavelengths corresponding to the K-absorption edges for Y and Zr are far from Cu $K\alpha$ radiation, but close to the $K\alpha$ radiation of Mo. Specifically, the K-absorption edge of Y is greater than the $K\alpha$ radiation of Mo, and the K-absorption edge wavelength value for Zr is lower than that for the $K\alpha$ radiation of Mo. This means that Y has higher absorption ability on the $K\alpha$ radiation of Mo than Zr does. Using $K\alpha$ radiation of Mo may therefore differentiate between the scattering factors of Y and Zr, so that ordering of the cation lattice may be observed (more in Section 6.2).

It was also reported that freezing of quadrupolar glass can be studied by x-ray diffraction (Hochli et al., 1990; Knorr and Loidl, 1985).

In this chapter, we are going to approach the defect structure of yttria-stabilised zirconia alloys and search for the evidence of quadrupolar glass behavior with high temperature x-ray diffraction technique using both Cu and Mo $K\alpha$ radiation. Before we go to the details of the experiments, a brief introduction about the relationship between the absorption and the atomic scattering factor is presented next.

6.2 Theoretical Background

6.2.1 Structure Factor of the Crystal with Anomalously Scattering Atoms

For x-ray diffraction, assuming that the frequency of the incident radiation is much greater than the frequency corresponding to any energy for excitation of the atom, the atomic scattering factor is (Cowley, 1981)

$$f(\underline{Q}) = \int \rho(\underline{r}) \exp(-i\underline{Q} \cdot \underline{r}) dr \qquad (6.1)$$

where $\rho(\underline{r}) = \Sigma \rho_n(\underline{r})$ is the time averaged electron density function. It is a function of scattering vector $\underline{Q}$. With increasing scattering angle θ, that is, with larger distance ($|\underline{Q}| = (2\pi/\lambda) \sin\theta$) from the origin of the reciprocal space, the atomic scattering factor in form (6.1) decreases rapidly and becomes almost constant at a high value of $|\underline{Q}|$.

If the atom has an absorption edge close to the incident x-ray frequency, the scattering factor of the atom is modified by anomalous dispersion. An imaginary part and a small real part are added to $f(\underline{Q})$ as defined by (6.1). Thus the atomic scattering factor is given by (Chung et al, 1993)

$$f = f_0(|\underline{Q}|) + f'(\lambda) + i f''(\lambda) \qquad (6.2)$$

and the atom is called an anomalously scattering atom.

The structure factor of a cation sublattice with anomalously scattering atoms is

$$F_{hkl} = \sum_{i=1}^{n} (f_{i0} + f_i' + if_i'') \exp\{2\pi i(hx_i + ky_i + lz_i)$$

$$(6.3)$$

where n is the number of cations in the unit cell. The complex phase function can be written as

$$A_i + i B_i = \exp\{2\pi i(hx_i + ky_i + lz_i)\} \qquad (6.4)$$

In this notation, the structure factor is given by

$$F_{hkl} = \sum_{i=1}^{n} (f_{i0} + f_i' + if_i'')(A_i + iB_i) \qquad (6.5)$$

In a general case the measured intensity of a reflection *hkl* is proportional to

$$F_{hkl}F_{hkl}^* = \sum_{i=1}^{n}\sum_{j=1}^{n}(f_{i0} + f_i' + if_i'')(A_i + iB_i)(f_{j0} + f_j' - if_j'')(A_j - iB_j)$$

$$= \sum_{i=j}^{n}[(f_{i0} + f_i')^2 + f_i''^2] + N(F)$$

(6.6)

where $N(F) = \sum_{i=1}^{n}\sum_{j\neq i}^{n}(f_{i0} + f_i' + if_i'')(A_i + iB_i)(f_{j0} + f_j' - if_j'')(A_j - iB_j)$

(6.7)

The second part in the right-hand side of form (6.6) contains the phase-sensitive terms; it will depend on the degree of order between the different types of atoms. The first part in the right-hand side of (6.6) contains all the square terms which are all positive and real. Equation (6.6) shows that the imaginary part of atomic scattering factor of cation i due to absorption cannot be ignored in determination of the reflection intensity for *hkl* net planes. The significance of (6.6) can be further analysed in four different situations, for simplicity assuming that only two different cations are present.

i), ii) There is no cation ordering, f_{i0}, f_i', and f_i'' for the two types of cations may or may not the same. In both cases f_{i0}, f_i', and f_i'' for the two types of cations can be replaced by averaged figures and put outside the summation, yielding Bragg scattering from the average lattice and a uniform background scatter, depending on whether the effective scattering from the different atoms is sufficiently similar or not. No ordering will be detected in a powder x-ray diffraction pattern.

iii) There is cation ordering, but f_{i0}, f_i', and f_i'' of the two different cations are close enough that they can be treated as equal and be put outside the summation. No ordering can be detected.

iv) There is cation ordering; f_{i0}, f_i', or f_i'' of one type of cation are substantially different from those of the other type of cation. Cation ordering can then be detected.

Values of f_{i0}, f_i', and f_i'' of Y and Zr at Kα-radiations of Cu and Mo are listed in table 6.2 and 6.3.

Table 6.2 f_0 of Y and Zr at different scattering vectors

Scattering Factor	Element	sinθ/λ (Å⁻¹)							
		0.0	0.1	0.2	0.4	0.6	0.8	1.0	1.2
f_0	Y	39	35.0	29.9	21.5	17.0	13.4	10.9	9.0
f_0	Zr	40	36.3	30.8	22.1	17.5	13.8	11.2	9.3

Extracted from Cullity, 1978.

Table 6.3 f' and f'' of Y and Zr at Kα-radiations of Cu and Mo.

Scattering Factor	Element	Cu-Kα₁	Mo-Kα₁
f'	Y	-0.2670	-2.7962
	Zr	-0.1862	-2.9673
f''	Y	2.0244	3.5667
	Zr	2.2449	0.5597

Extracted from *International Tables for Crystallography*, Vol. C, edited by Hahn, T.

It can be seen that at Cu-Kα₁ radiation, the values of f_{i0}, $f_i^{'}$, and $f_i^{''}$ for both Y and Zr are very close so even if there is cation ordering, situation iii) will apply; no cation ordering can be detected. However at Mo-Kα₁ radiation, the values of f'' for Y and Zr are substantially different. According to form (6.6), situation iv) is applicable, and cation ordering could be detected if, indeed, there is a cation ordering.

6.2.2   Freezing of Orientational Glasses Indicated by X-ray Diffraction

It is well known that elastic strain in a crystal can be detected by the x-ray diffraction because local strain fields cause broadening of Bragg scattering peaks (Klug and Alexander, 1974; Wilson, 1963). Different from the local static distortions which cause diffuse scattering, elastic strain is a distortion with large correlation length. The interplanar spacing for a set of parallel planes $h\,k\,l$ subject to elastic strain is not a single value, rather a variable following a Gaussian distribution with the mode at the interplanar spacing when there is no elastic strain. It is straightforward to understand the broadening of the Bragg diffraction caused by elastic strains based on the fact briefed above. The most difficult problem in reality is how to separate the broadening

caused by elastic strains from the broadenings caused by other factors, such as small particle size, instrumental aberrations, etc.

When a quadrupolar glass material undergoes a transition from a supercooled liquid to a glass, all quadrupoles (local strain ellipsoids, see Nowick and Heller, 1963) are frozen. Elastic strain fields are formed as a consequence of the freezing. Therefore the transition from a supercooled liquid to a glass could be detected by monitoring the breadths of Bragg reflections as a function of temperature.

Knorr et al. (1985) studied the glass transition of the quadrupolar glass $(KBr)_{1-x}(KCN)_x$ with $x = 0.2$, 0.5, ..., 0.9 in the temperature range from 15 to 300K using x-ray powder diffraction technique. They found that in the glass compositions, $x = 0.53$, 0.5, 0.2, there were plateaus in the low temperature range on the curves representing the width of the cubic lines versus temperature. The deflection points were reported to correspond to the glass transition temperatures for those quadrupolar glasses.

6.3 Experimental Details

6.3.1 Sample Preparation

Yttria-stabilised zirconia single crystals with yttria content from 9.5 mole% to 24 mole% made by Ceres Corporation, Waltham, Mass. were crushed and ground into powder form using agate mortar and pestle. The powdered crystals were sieved through a 325 mesh screen.

Silicon metal powder and K_2SO_4 powder of analytical grade were used to calibrate the accuracy of the goniometer and temperature.

6.3.2 Instrumentation

All the measurements were made using the Diffractometer Rigaku D/max-A at Materials Engineering Department, Monash University. The goniometer of the diffractometer is of a vertical type. The original high temperature attachment of x-ray

diffractometer from Rigaku was used to perform x-ray diffraction at different temperatures. Its central core configuration is sketched in Fig. 6.1.
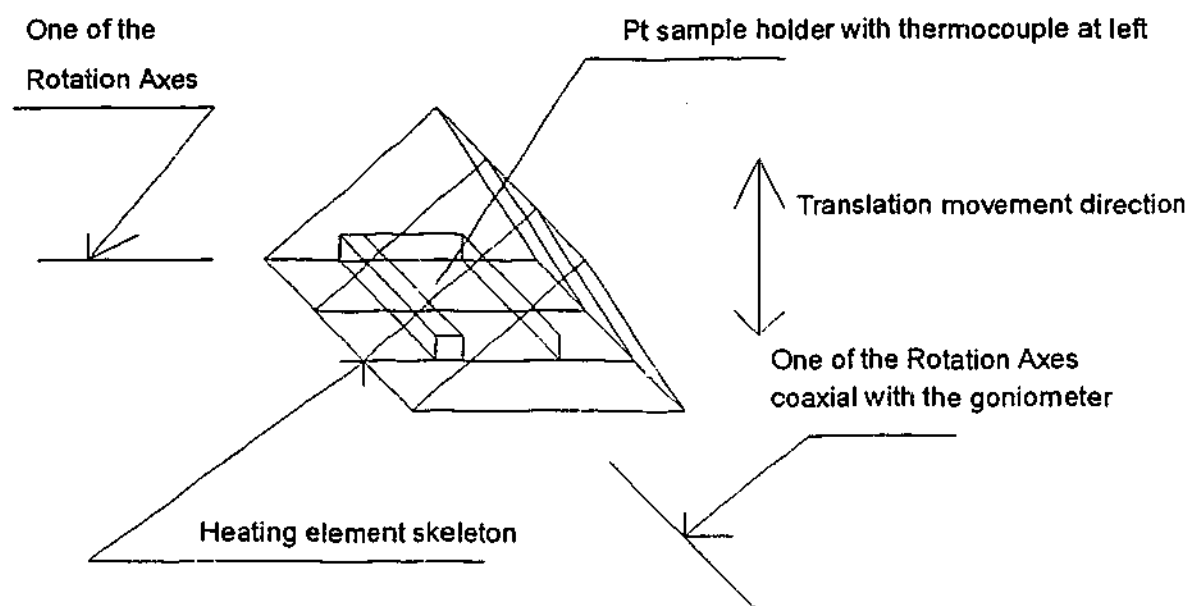
Fig. 6.1 The central core configuration of the high temperature x-ray diffractometer attachment.

Outside the central core there are inner and outer shielding drums and a water cooling case. Each of them has a x-ray window covered by aluminium foil or beryllium foil. When Cu radiation was used, one window was covered with nickel foil, which replaces the filter in front of the detector to remove $K\beta$ radiation. The filter material for $K\beta$-radiation of Mo is Zr. Because the sample is made of zirconia, no extra Zr filter was used.

The heating of the high temperature attachment was controlled independently using an Eurotherm controller (Model 904).

The goniometer was calibrated by running a diffraction pattern on a standard Si metal powder sample. The alignment of the high temperature attachment was carried out following the Instruction Manual For High Temperature X-Ray Diffractometer Attachment For Vertical Goniometer (Rigaku).

6.3.3 Temperature calibration

The difference between the reading of the thermometer connected to the temperature controller and the temperature on the surface of the specimen was calibrated using K_2SO_4, which has a phase transformation from orthorhombic to hexagonal at 588°C, and $CaSO_4$, which has a phase transformation at 1210°C. The sample was brought close to its transformation temperature, thereafter scanned by x-rays at temperatures in steps of 10°C according to the thermometer. The phase transformation temperature of K_2SO_4 recorded by the reading of the temperature controller was as at 590-600°C, and for $CaSO_4$ was at 1220-1230°C. So it was noted that the temperature difference between the surface of the sample and controller reading is about 10°C. This difference is not crucial for the interpretation of our experiments.

6.3.4 Measurement and data processing

Operation parameters of the diffractometer are summarised in table 6.4. For measurements at high temperatures, the heating rate was 5°C/min, and the sample was soaked for 30 minutes before measuring.

The measured data were downloaded from the on-line control computer as ASCII documents and were processed on a separate computer using the Trace software version 3.0 developed by Diffraction Technology Pty Ltd., ACT, Australia. $K\alpha_2$ radiation in all the diffraction patterns was stripped off according to the intensity ratio $K\alpha_2 / K\alpha_1 = 0.51$ during data processing.

Table 6.4   Operation parameters of the diffractometer

Operation parameter	Room temperature		High Temperature	
	Cu radiation	Mo radiation	Cu radiation	Mo radiation
Voltage (kv)	40	50	50	50
Current (mA)	22.5	17.5	30	20
Divergence slit	1°	1/2°	1°	1/2°
Receiving slit	0.3mm	0.15mm	0.3mm	0.15mm
Scan speed (2θ)	1°/min	0.5°/min	1°/min	0.5°/min

Scan range (2θ)	20-80°	10-40°	20-80°	12-40°
Time constant	2 sec	2 sec	2 sec	2 sec

6.4 Experimental Results

6.4.1 Cu Radiation

Diffraction patterns around the 111 peak of Y-CSZ with various yttria contents at room temperature are shown in Fig. 6.2. The peaks are typical f.c.c and well shaped. The variation of intensity with composition was not expected, and it might be caused by sample preparation, since, as we have warned earlier, if our claim for a glass transition with T_g near 400°C is correct, Y-CSZ at room temperature is nearly 400°C below the transition and likely to be out of equilibrium.

Fig. 6.3 shows typical diffraction patterns of 12 mole% Y-CSZ as a function of temperature. The striking feature in Fig. 6.3 is that the X-ray diffraction intensity drops dramatically after 1000° regardless of the index of the reflecting net planes. The intensity for 111 diffraction drops at 500°C and undergoes another dramatic drop after 1000°C. Scatter from the 311 plane has an intensity maximum at about 400°C and a minimum at 1200°C. For 220 diffraction the intensity stays roughly the same until about 1000°C.

Fig. 6.2.

6-9
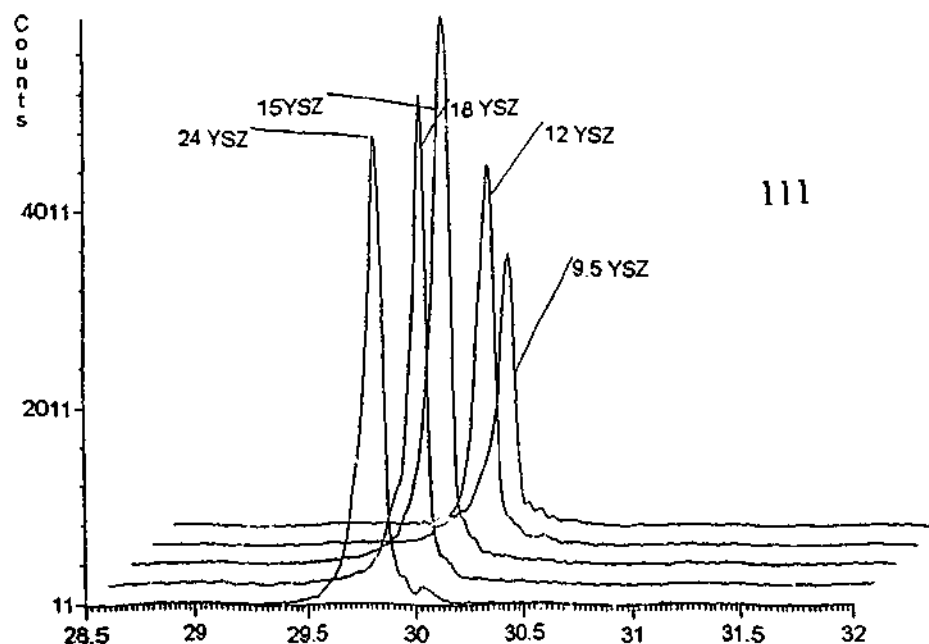
Fig. 6.2 Diffraction patterns around the 111 peak of Y-CSZ with various yttria contents at room temperature, Cu radiation.

The behavior of the three Bragg diffraction peaks as a function of temperature suggests strongly the operation of the mode-coupling structure arrest feedback mechanism referred to in chapter 3. Despite the fact that the measured peaks are truncated, and that the room-temperature measurement may reflect a non-equilibrium state, it seems clear that for a given reflection, the heights of all the peaks are roughly comparable for temperature between 400-1000°C, which we have claimed corresponds to the supercooling range and fall abruptly above this value. Looked at as the effect of a Debye-Waller factor, the fact that the intensities of individual reflections behave so similarly as a function of temperature (at least in the high-temperature region) for reflections so far apart in reciprocal space suggests a relative wavelength (or wavenumber) insensitivity, one of the chief symptoms of the MCT.

Using a simple equipartition argument, which should be valid at high temperatures, where Debye-Waller type reduction in intensity is greatest, the reduction function which multiplies the Bragg intensities is approximated by

$$\exp\left\{-ATu^2\right\}$$

where A is a constant, u is a reciprocal space coordinate and T is in Kelvins (K). It is more familiar as a function of u for constant T. Each of our experimental intensity plots in Fig. 6.3, however, can be considered to be an intensity reduction function of temperature, for constant u. The remarkable fact emerging from these plots is that around 1000°C, the fall-off in intensity (about 50% for 1200°C) is the same for each reflection, regardless of u value. Given that the value of u^2 for the 220 reflection is approximately three times larger than that for the 111 and approximately six times larger in the case of 331, the details near 1000°C barely change at all, rather than being damped out completely at the higher values of u^2. Very roughly, if T_R is the temperature at which the Debye-Waller-type reduction of 1/e in intensity occurs, then according to our approximations above $(T_R u^2)_{111} = (T_R u^2)_{220}$ for such a 1/e reduction. If the arrest mechanism were highly wavenumber dependent, T_R for the 220 reflection would then be about 450K if that for the 111 reflection were about 1200K. Fig.6.3 appears to indicate that this is not the case.

The full widths at half maximum (FWHMs) of 111, 220, 311 at different temperatures are shown in Fig. 6.4. Corresponding to the low intensity at temperatures higher than 1000°C shown in Fig. 6.3, FWHMs for all three reflection net planes increase dramatically after 1000°C. We believe that after 1000°C defects are "unlocked" from their "tees", thermal excitation plays an important role, and the drop in peak intensity and increase in FWHM are caused by Debye-Waller effects associated with thermal vibrations, paraelasticity and ionic transport. For the 111 reflection, the FWHM becomes slightly broadened when the temperature is below 600°C and for the 220 reflection the FWHM is broadened substantially at temperature below 500°C: these effects may be due to critical behaviour in the mode-coupling and freezing range. There is no systematic broadening of FWHM for the 311 reflection at lower temperatures, except for a gradual broadening as the temperature rises.
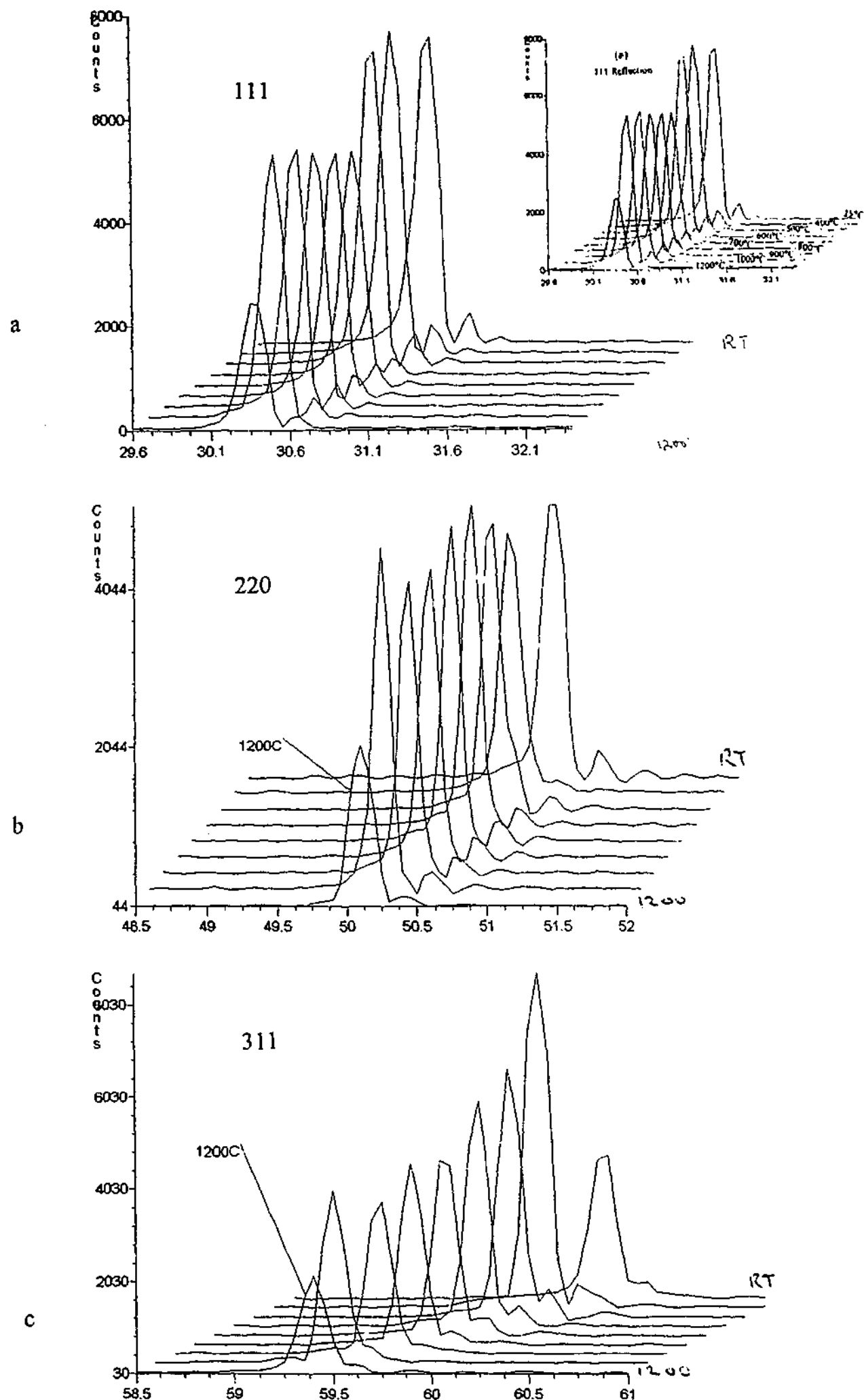
Fig. 6.3 Diffraction patterns of YSZ-12 as a function of temperature. The graphs in (b) and (c) have the same temperature sequence as indicated in (a).
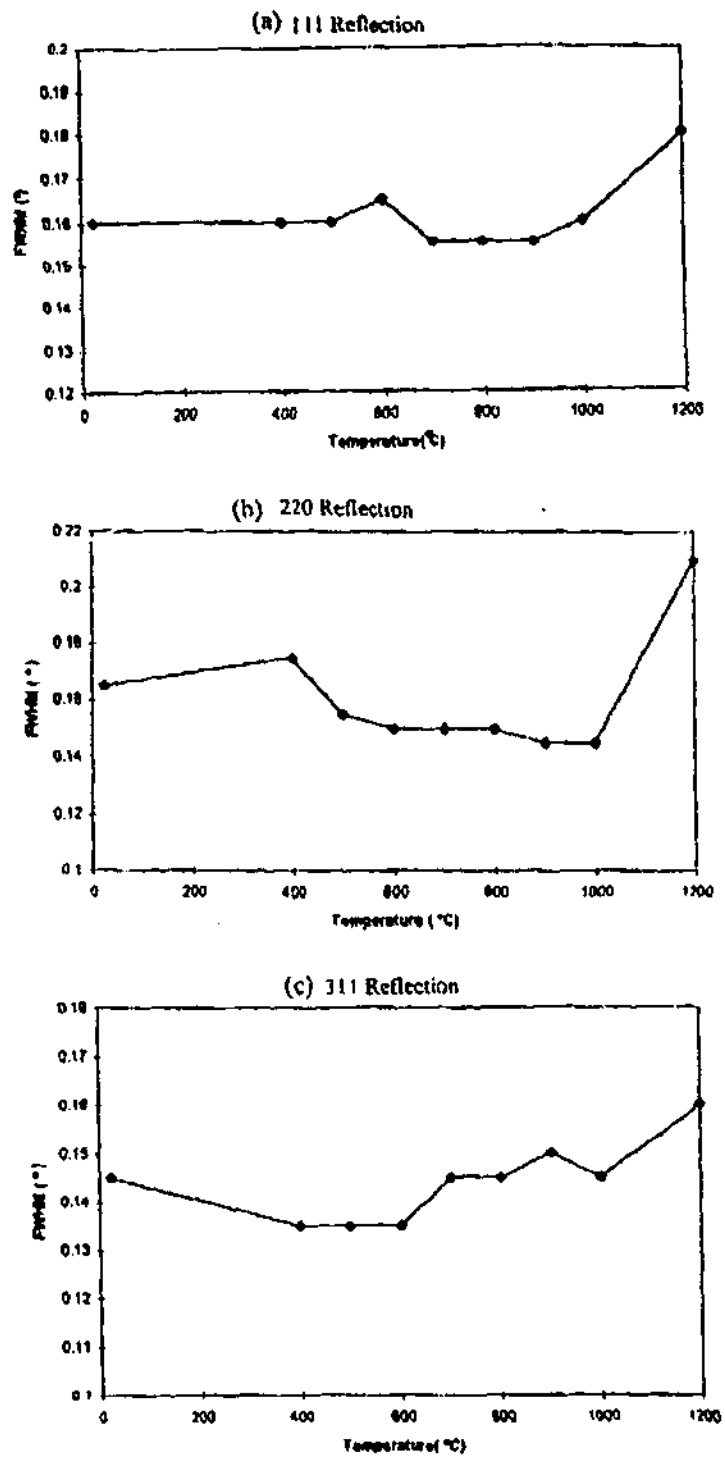
Fig. 6.4 The full width at half maximum (FWHM) of 111, 220, and 311 reflection peak as a function of temperature.

6.4.2. Mo Radiation

Fig. 6.5 shows diffraction patterns of 12 mole% Y-CSZ under Mo radiation at different temperatures. In comparison with diffraction patterns of the same materials under Cu radiation, peaks in Fig. 6.5 are split into doublets or triplets. This is more obvious at 111_{fcc} reflections. Fig. 6.6 shows the magnified $111_{f.c.c}$ reflection positions. It can be seen that at and below 800°C, the $111_{f.c.c}$ reflections are split into a well formed doublet. Fig. 6.7 and 6.8 show the magnified $220_{f.c.c}$ and $311_{f.c.c}$ reflections respectively. For $220_{f.c.c}$ and $311_{f.c.c}$ reflections, the splitting of peaks begins at temperature 1000°C, and the doublets or triplets are not as well formed as those of 111 reflections.

As an example, d-spacing and 2θ angles of the separated peaks near positions of 111, 220 and 311 reflections of fluorite structure at 500°C are listed in table 6.5. The differences in d-spacings for each group (difference between the largest d-spacing and smallest d-spacing in the same group) are 0.036Å for 111, 0.01Å for 220 and 0.007Å for 311.

Table 6.5.

No.	2θ Angle (°)	D-spacing (Å)	Relative Intensity(%)	$f.c.c$ group
1	13.736	2.966	97	111
2	13.768	2.959	89	111
3	13.904	2.93	100	111
4	22.432	1.823	67	220
5	22.484	1.819	76	220
6	22.56	1.813	68	220
7	26.368	1.555	56	311
8	26.388	1.554	53	311
9	26.492	1.548	58	311
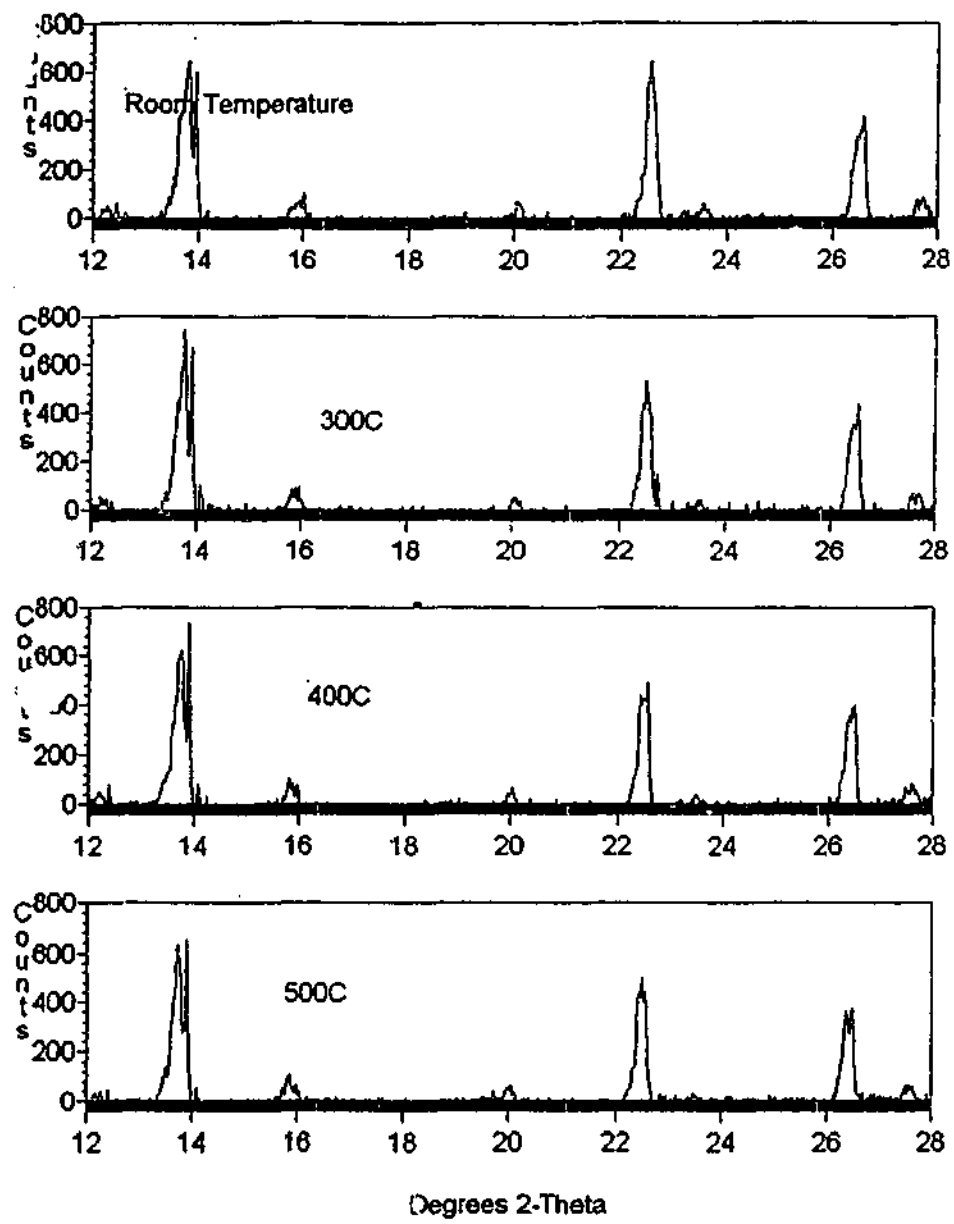
Fig. 6.5 Diffraction patterns of YSZ-12 under Mo radiation at different temperatures, continued to next page.
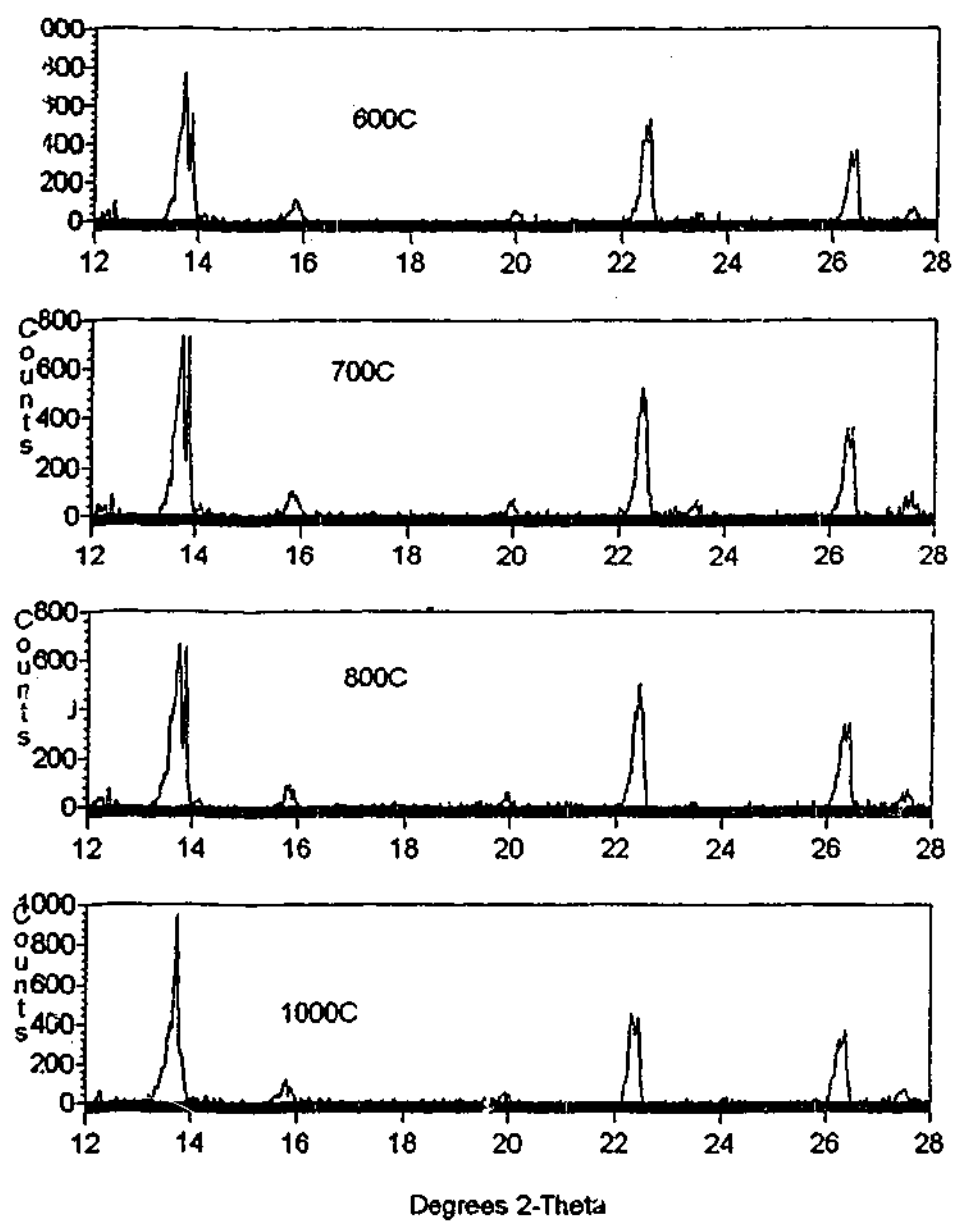
Fig. 6.5 Diffraction patterns of YSZ-12 under Mo radiation at different temperatures.
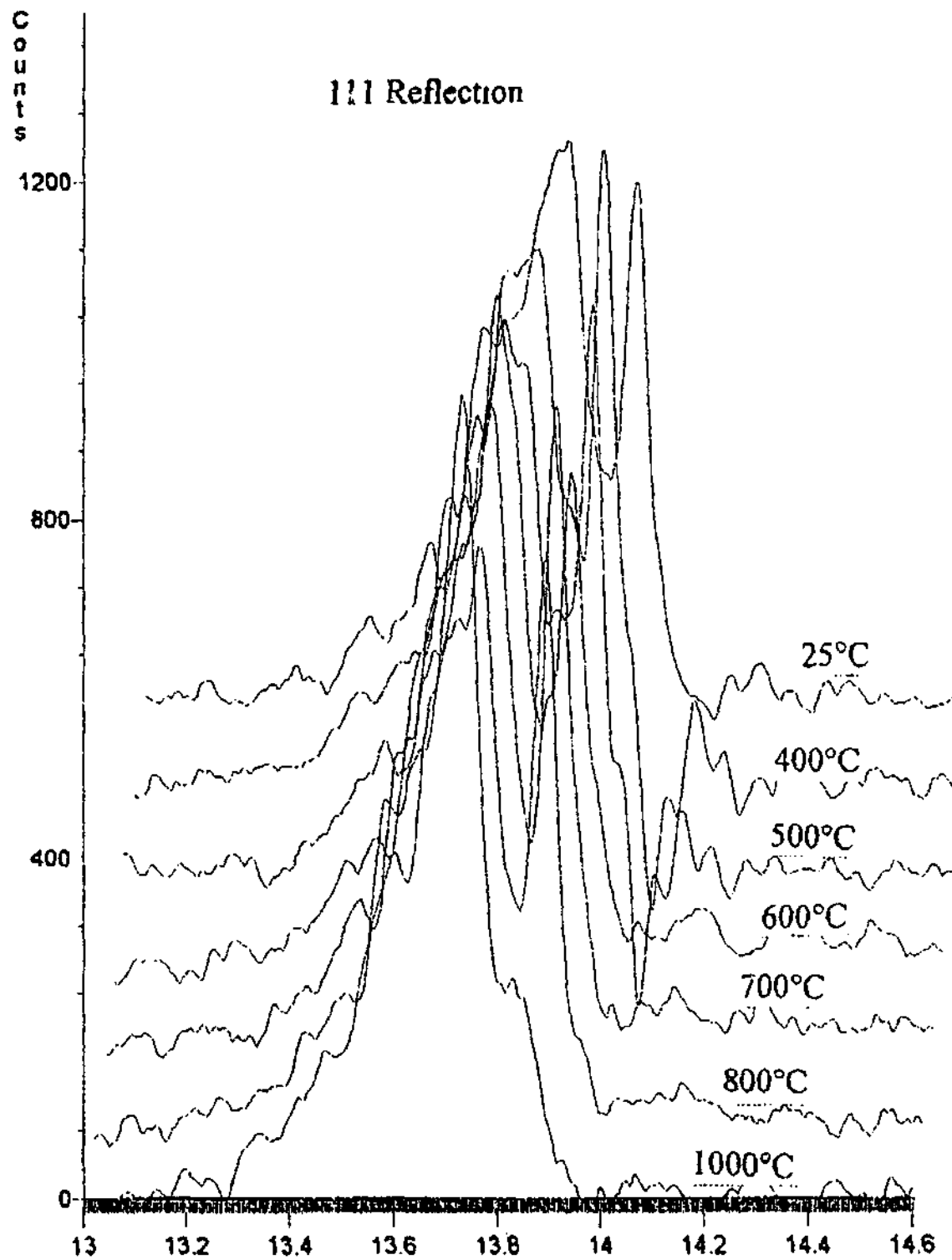
Fig. 6.6 111 reflections of YSZ-12 under Mo radiation at different temperatures.
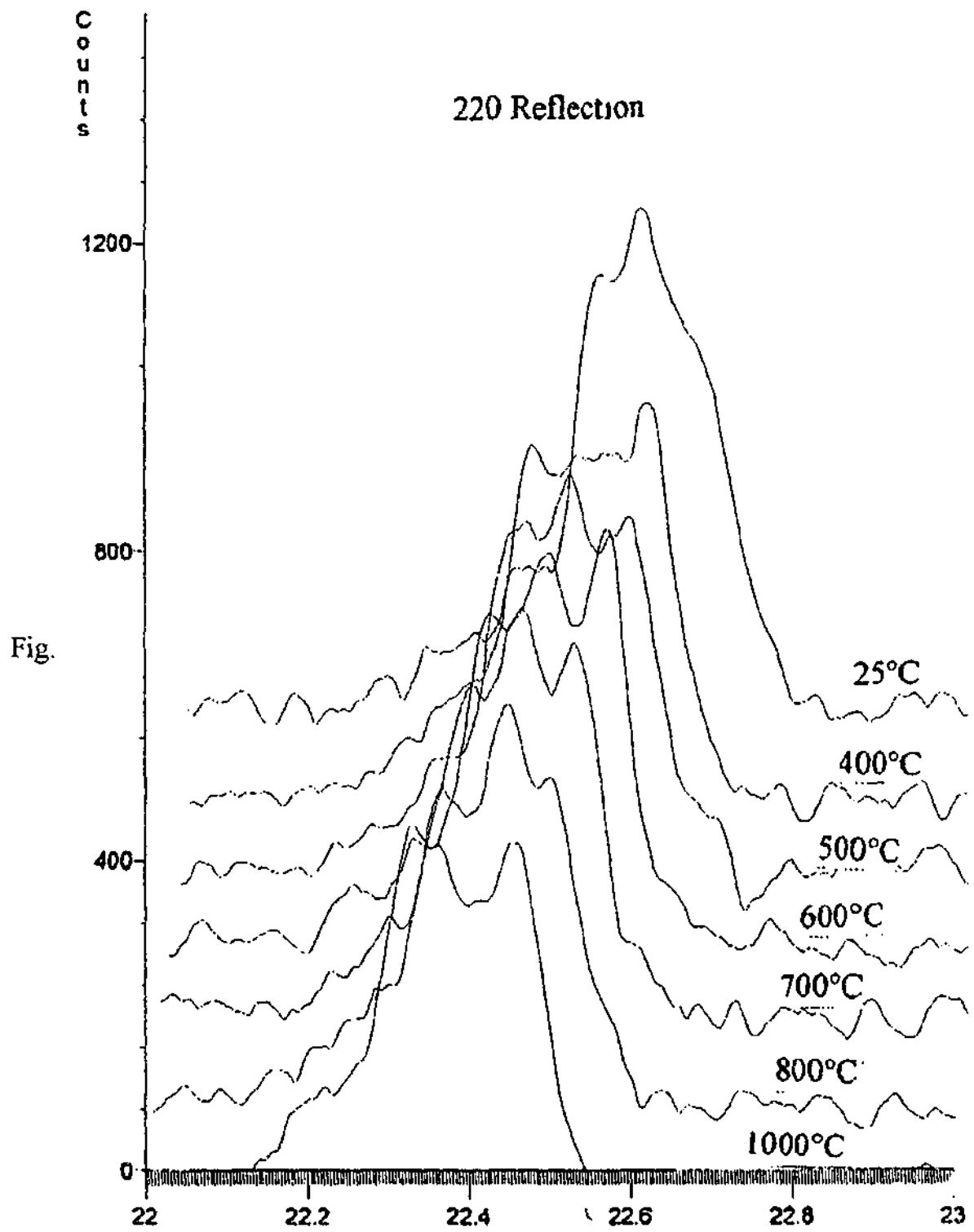
Fig. 6.7 220 reflections of YSZ-12 under Mo radiation at different temperatures.
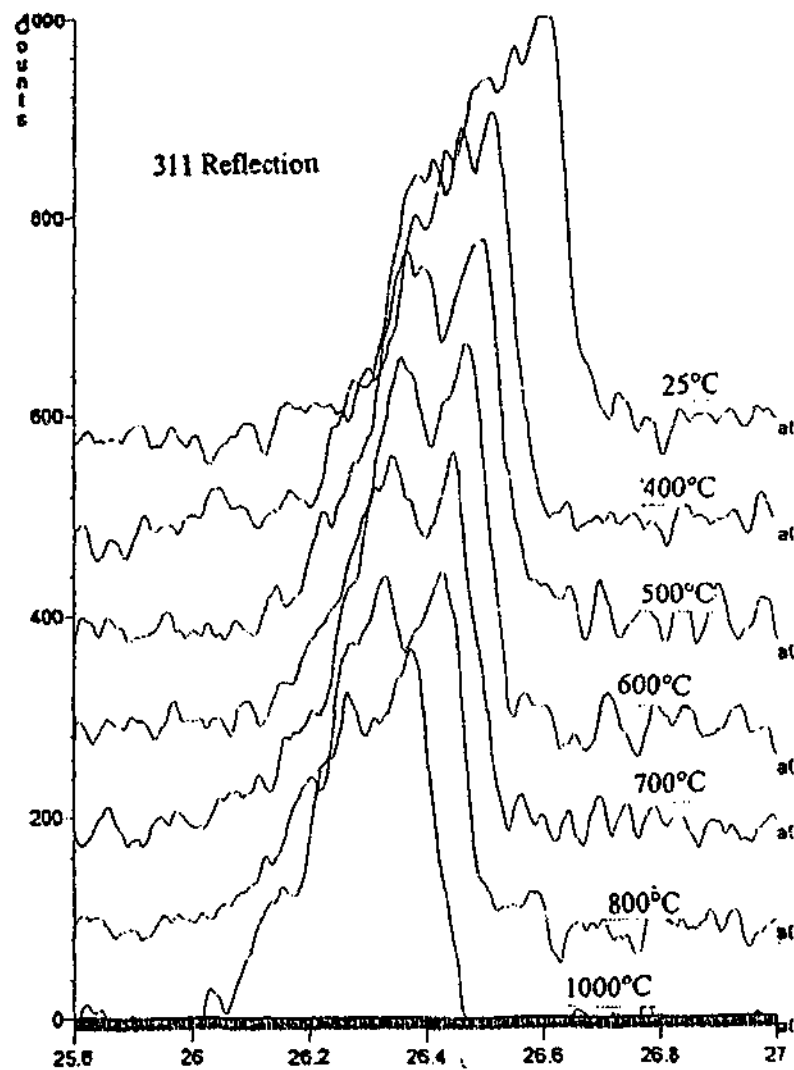
Fig. 6.8 311 reflections of YSZ-12 under Mo radiation at different temperatures.

6.5 Discussion

The striking features of results presented in section 6.4 can be summarized as follows:

(a). Under Cu radiation, all reflection net planes yield single peaks; there is no peak splitting.

(b). 111 peak is broadened slightly at temperatures below 650°C, and 220 peak is broadened substantially at temperature below 600°C, no systematic broadening for other peaks.

(c). The plots of intensity versus temperature for each Bragg reflection appear to support the wavelength independence criterion of the MCT.

(d) Under Mo radiation, $f.c.c$ peaks are split into doublets, or triplets at temperature about or below 1000°C.

The results can be well explained with the model of microdomains embedded in a distorted cubic matrix similar to the Allpress-Rossell model as mentioned in chapter 3. To facilitate the discussion, the microdomain model is briefly recapped below.

Through our diffraction study, we believe that in a mesoscopic range the microdomains could have a structure similar to one of the three ordered phases found in ZrO_2-Sc_2O_3 γ, β, δ (Thornber et al., 1968); evidences discussed in this chapter suggest that more likely they are γ, or β (see later). Cations are ordered in these microdomains and the unique axis of the microdomains is along one of the four $\langle 111 \rangle$ directions in the cubic matrix, since these ordered phases are fluorite-related by ordering of vacancies and/or cations along $\langle 111 \rangle_{fcc}$ directions (Thornber et al., 1968). Microdomains of this type, however, are the "bare" reorientable defects of VKZ model B, and hence crystallographically unable to form a right-angle "tee" configuration in pairs, which VKZ (Vollmayr et al, 1991) calculate is not describable as a six-state glass with tetragonal local symmetry at low temperatures. We have seen, nonetheless, from the electron diffraction patterns scattered from low-dopant Y-CSZ in chapter 5, that the "forbidden" tetragonal diffraction spots are present in the YSZ case as well as in the CaSZ case. This difficulty may be overcome by reference to VKZ's remarks (mentioned in chapter 3) that the anisotropy of the lattice near criticality may not necessarily reflect the apparent microscopic anisotropy, that of the four-state model in the present case, i.e., at the phase transition, the detailed microscopic interactions are not necessarily a good guide to the low-temperature anisotropy.

How can the emergence of a six-state glass state in Y-CSZ at low temperature be reconciled crystallographically with a defect with a unique three-fold axis along $\langle 111 \rangle$ direction? One possible solution is that four near-neighbor VKZ model-B defects combine to form an effective "tee" configuration on $\{100\}$ planes as in the six-state case. This might be achieved in the following way. Two model B defects "pair up" on (e.g.) the $(0\bar{1}1)$ plane to give a compound defect which in turn is further compounded by "pairing up" with a similar linked pair on the (011) plane to give a "tee"-like configuration on the (100) plane made up of four microdomains. Though approximate and highly speculative, some evidence for complex partial ordering of this type has been presented in chapter 5. There, both CaSZ and YSZ diffraction patterns exhibit the cross-shaped diffuse scatter in the $\langle 100 \rangle$ projections, due, as we have already proposed, to orientational ordering into "tees" on $\{100\}$. It is at least equally arguable that the "mushroom-shaped" diffraction radiating hexagonally from $2\bar{2}0$-type spots in $\langle 111 \rangle$ projections of Y-CSZ is evidence for similar orientational order of pairs of

Model B defects in $\{110\}$ planes, in part confirmation of the "compound tees" hypothesis advanced in this chapter.

In such a model as the one described above, the ordering of cations in a mesoscopic range is not be able to be detected by X-ray diffraction using Cu radiation, or electron or neutron diffraction because yttrium and zirconium have similar atomic scattering factors or nuclear scattering factors under these circumstances, where as we discussed at section 6.2.1, situation iii) applies. Hence, it is not surprising that the diffraction patterns of 12 mole% Y-CSZ consist of well defined peaks of *fcc* lattice under Cu radiation, as shown in Fig. 6.2.

The broadening of 111 and 220 reflections at temperatures below 650°C are believed to be related to the freezing of the rotors at the mode-coupling transition, which results in the formation of local elastic strain fields. As we mentioned before, in our microdomain model, the compound rotors order in $\{110\}$ and $\{111\}$ planes. The result that broadening of the 220 peak below 650°C shown in figure 6.4 is more substantial than that of the other peaks suggests large elastic strain fields in $\langle 110 \rangle$ directions. This observation then, appears to support what we proposed in our microdomain model; that 650°C would be the mode-coupling transition temperature or the temperature for the sharp onset on structural arrest for the orientational glass 12 mole% Y-CSZ.

The separation of cubic fluorite structure reflections into doublets or triplets under Mo radiation proves that there is a cation ordering in the Y-CSZ. The situation iv) discussed at section 6.2.1 applies in this case. Unfortunately it is impossible to further identify the details of cation ordering structurally, which should be closely related to the microdomain structure, since the separations of peaks are not completely isolated. However reports about the intermediate phases found in ZrO_2-Sc_2O_3 (Lefevre, 1963; Ruh et al., 1977; Sakuma and Suto,1986) may give some hint on the microdomain structures in ZrO_2-Y_2O_3. In ZrO_2-Sc_2O_3 there is a β-phase in the region of 9 to 13 mole% Sc_2O_3, a γ-phase in the region of 15 to 23 mole% Sc_2O_3 and a δ-phase in the region of 24 to 40 mole% Sc_2O_3 (Ruh et al., 1977). All the three intermediate phases are rhombohedral (Lefevre, 1963; Thornber et al., 1970). XRD results of these intermediate phases obtained by Lefevre (1963) showed that separation of cubic fluorite reflections into doublets or triplets is the feature of β- and γ- phase formations.

It seems very likely that the separation of cubic fluorite structure reflections into doublets or triplets under Mo radiation in ZrO_2-Y_2O_3 reported in this thesis are attributable to β- or γ- phases as well.

Our sample composition is 12 mole% Y_2O_3 , which is in the region of β- phase; from this viewpoint, the microdomains may share the β- phase structure. On the other hand, when the comparison is made between the span of peak splittings found in our experiments and the span of peak splittings reported by Lefevre (1963) (table 6.6), it seems that the spans of peak splittings observed in this thesis are closer to those of γ-phase reported by Lefevre (1963).

β- and γ-phases in ZrO_2-Sc_2O_3 were reported to be stable below 600°C and 1100°C respectively (Ruh et al., 1977). Sakuma et al. (1986) found that β-phase in ZrO_2-Sc_2O_3 is stable up to 800°C. The separations of cubic fluorite reflections under Mo radiation observed in our experiments occur at temperature at 1000°C or higher. This observation supports the possibility of the presence of the γ-phase in our sample. If the extra reflections are caused by the presence of the β-phase it means that the upper temperature limit for β-phase in ZrO_2-Y_2O_3 may be as high as 1000°C. So far no reports in the literature about β- and γ- phases in ZrO_2-Y_2O_3 have been found, to our knowledge.

Table 6.6.

	d-spacing spans of peak splittings (Å)		
f.c.c group position	12 mole% Y-CSZ	β- phase in Sc-CSZ*	γ-phase in Sc-CSZ*
(111)	0.036	0.089	0.016
(220)	0.01	0.039	0.011
(311)	0.007	0.035	0.007

* Lefevre (1963)

6.6 Conclusion

XRD studies on 12 mole% Y-CSZ revealed that 220 and 111 reflection peaks are broadened at temperatures below 650°C, and that reflection peaks under Mo radiation

are split into doublets or triplets at temperature below 1000°C.   The results can be explained very well using the microdomain-orientational glass model.   The broadening is caused by the freezing of the rotors in a cubic matrix, which signals the formation of orientational glass of Y-CSZ.   The rotors consist of microdomains with probable structures of β or γ.   Cation ordering in those microdomains accounts for the splitting of the reflection peaks under Mo radiation.   Unfortunately it was impossible to identify the particular ordered phase from current results,   although γ-phase is possibly more likely.

All three phases ($\alpha, \beta.\gamma$) are of VKZ Model B type, and a mechanism has been suggested how Model B defects might combine to give a six-state glass with local random tetragonal distortions.   Plots of intensity versus temperature suggest that the structural arrest mechanism is wavenumber insensitive, which is a symptom of the mode-coupling transition.

CHAPTER 7

NEUTRON DIFFUSE SCATTERING INVESTIGATION OF YTTRIA-STABILISED ZIRCONIA

7.1 Introduction

In this chapter, the measurement of neutron diffuse scattering from single crystals of a 15 mole% Y_2O_3-stabilised ZrO_2 will be reported. With regard to the defect structure, as mentioned before, there is a considerable body of literature devoted to a description of the defect structure of CSZ. As we put forward in Chapter 3, a model of microdomains of ordered phases coherently embedded in the tetragonally distorted cubic matrix is more favored. To achieve the aim of the project, which is to understand more the diffuse scattering caused by the defects and the relation between the diffuse scattering patterns and the glass concept of CSZ, neutron diffuse scattering from CSZ has been undertaken. The aim of this chapter is twofold: a) to justify the microdomain model of defect structure through neutron diffuse scattering measurements and b) to attempt to find the glass transition temperature of the 15 mole % Y_2O_3-stabilised ZrO_2 and further evidence for the mode-coupling mechanism. Prior to the experimental details and any discussion on diffuse scattering from CSZ, the theoretical aspects of the scattering will be briefly discussed in the following section.

7.2   Theoretical Background

Scattering from a crystal due to deviation from either the average composition, or the mean location of atoms is described as *diffuse*. The word diffuse is used as the magnitude of the cross section of these effects is much smaller than that for Bragg scattering and is smeared out in reciprocal space. The effects of deviation from the mean composition and the average structure have been described in detail by a number of workers (Lovesey, 1987; Cowley, 1975). In principle, diffuse scattering can result from either chemical ordering of atoms in the lattice, or local distortion, away from atomic mean positions. Here an *intentionally* brief description will be given with the

aim of discussing the main features of diffuse scattering, and to give a grounding for the measurements which will be reported in this chapter.

7.2.1 Chemical Effects: Laue Monotonic Scattering

The discussion of diffuse scattering for simplicity will be centered on a simple binary alloy which forms a rigid Bravais lattice, with lattice vector $\underline{l}$. The elastic (coherent) cross section is given as (Lovesey, 1987),

$$(\frac{d\sigma}{d\Omega})_{coh} = \overline{\left|\sum_l \overline{b_l} \exp(i\underline{Q} \cdot \underline{l})\right|^2} \tag{7.1}$$

where $\overline{b_l}$ is the mean scattering length of atom l averaged over all spin states and isotope distributions, and $\underline{Q}$ is scattering vector. The horizontal bar in the expression denotes an average over the spatial configurations of the two components of the alloy. We label the components 1 and 2. Let c be the fractional concentration of atoms of type-2. The configurational average of the scattering length is then,

$$\overline{(\overline{b})} = (1-c)\overline{b_1} + c\overline{b_2} = b \tag{7.2}$$

In order to perform the configurational average over the elastic coherent cross section it is useful to introduce a site occupancy function p_l which is defined by,

$p_l = 1$, if l labels an atom of type 2

$p_l = 0$, if l labels an atom of type 1. $\tag{7.3}$

By definition,

$$\overline{p_l} = c \tag{7.4}$$

and

$$\sum_l p_l = cN \tag{7.5}$$

where N is the total number of atoms in the alloy. From the definition of p_l we can write the mean scattering length

$$\overline{b_l} = \overline{b_1} + p_l(\overline{b_2} - \overline{b_1}) = b + (\overline{b_2} - \overline{b_1})(p_l - c) \tag{7.6}$$

From equation 7.1 to 7.6, it can be shown (Lovesey, 1984) that the coherent cross section can be written as

$$\left(\frac{d\sigma}{d\Omega}\right)_{coh} = \left(\frac{d\sigma}{d\Omega}\right)_{Bragg} + N(\overline{b_2} - \overline{b_1})^2 c(1-c) \qquad (7.7)$$

where Bragg scattering cross section is

$$\left(\frac{d\sigma}{d\Omega}\right)_{Bragg} = b^2 \left| \sum_l \exp(i\underline{Q} \cdot \underline{l}) \right|^2 \qquad (7.8)$$

and the second term is known as Laue monotonic diffuse scattering. Equation (7.7) shows that the total elastic cross section for this perfect alloy crystal consists of Bragg scattering and Laue monotonic diffuse scattering. While Bragg scattering is localised in reciprocal space and occurs only for specific values of $\underline{Q}$, diffuse scattering in this case is independent of $\underline{Q}$. Laue monotonic scattering is derived from purely compositional effects and vanishes if $c = 1$ or $c = 0$. The term $(\overline{b_2} - \overline{b_1})^2$ in this case acts as a contrast factor.

This result can also be applied to an arbitrary lattice if we interpret b as the configurationally averaged unit-cell structure factor.

7.2.2 The Effect of Static Distortion

To derive the Laue monotonic diffuse scattering, the atoms are assumed in the ideal positions of a crystal. To see the effect of static lattice distortion in the coherent elastic cross-section, a vector $\underline{h_l}$ describing the deviation of an atom from its ideal atomic position is introduced. Assuming a dilute alloy with rigid lattice and weak distortion (by rigid lattice we mean no thermal vibration, otherwise a Debye-Waller factor due to thermal motion, $\exp(-w)$, needs to be introduced) the atom position is determined by the vector $\underline{h_l} + \underline{l}$, where $\underline{l}$ is a lattice vector for the average lattice and satisfies $\exp(\underline{\tau} \cdot \underline{l}) = 1$ for all $\underline{l}$, and $\underline{h_l}$ satisfies

$$\sum_l \underline{h_l} = 0 \qquad (7.9)$$

indicating no macroscopic deformations. The coherent elastic cross-section in this case is

$$\left(\frac{d\sigma}{d\Omega}\right)_{coh} = \overline{\left|\sum_l \overline{b}_l \exp\{i\underline{Q}\cdot(\underline{l}+\underline{h}_l)\}\right|^2} \tag{7.10}$$

In the dilute case the concentration of type-2 atoms is very small and the correlation between the distribution of the scattering lengths and the distortion vector is negligible. Therefore the average scattering amplitude (7.10) can be written as

$$\overline{(\overline{b}_l)\exp(i\underline{Q}\cdot\underline{h}_l)} = b\exp(-H(\underline{Q})) \tag{7.11}$$

where the equality defines a static Debye-Waller factor with an exponent $H(\underline{Q})$. If the distortions follow a Gaussian distribution with $\underline{h}=0$ so that equation (7.9) is satisfied, on average

$$H(\underline{Q}) = \frac{1}{2}\overline{(\underline{Q}\cdot\underline{h}_l)^2} = \frac{1}{6}Q^2\overline{h^2} \tag{7.12}$$

where $\overline{h^2}$ is the mean-square distortion. The Bragg cross section follows directly from (7.11),

$$\left(\frac{d\sigma}{d\Omega}\right)_{Bragg} = b^2\exp\{-2H(\underline{Q})\}\left|\sum_l \exp(i\underline{Q}\cdot\underline{l})\right|^2 \tag{7.13}$$

The diffuse cross section can be obtained by subtracting the Bragg cross section from (7.10). To achieve this, the approximation

$$\exp(i\underline{Q}\cdot\underline{h}_l) \approx 1 + i\underline{Q}\cdot\underline{h}_l \tag{7.14}$$

is used, in the limit of weak distortions, and it follows that (Lovesey, 1984)

$$\begin{aligned}
\left(\frac{d\sigma}{d\Omega}\right)_{diffuse} &= \left(\frac{d\sigma}{d\Omega}\right)_{coh} - \left(\frac{d\sigma}{d\Omega}\right)_{Bragg}\\
&\approx N(\overline{b_2}-\overline{b_1})^2 c(1-c) + b^2\sum_{ll'}\overline{(\underline{Q}\cdot\underline{h}_{l'})(\underline{Q}\cdot\underline{h}_l)}\exp\{i\underline{Q}\cdot(\underline{l}-\underline{l'})\}
\end{aligned} \tag{7.15}$$

The second contribution on the right-hand side is the diffuse scattering cross section caused by local static distortion. Unlike Laue monotonic scattering, it is localized in reciprocal space, and the precise form of (7.15) depends on the details of local distortions or short-range ordering.

7.2.3   Quasi-elastic Scattering

The term quasi-elastic is usually applied to that part of the inelastic scattering spectrum which arises from random, or stochastic, processes that occur over a relatively long time scale. Rotational jumps of a molecule and diffusion of a particle in a liquid or hot solid are examples of the types of motion which contribute to the quasi-elastic component of the spectrum (Lovesey, 1984).

When a system changes from a supercooled liquid to a glass state as the temperature decreases, both the self-diffusion constant Ds and the Maxwell relaxation time τ vary dramatically at the cross-over region. Here $\tau = \eta/G$, where η is the shear viscosity which changes by many orders of magnitude at cross-over region, G is rigidity modulus, which is comparatively insensitive to temperature.

Consider a model for scattering from a particle executing harmonic oscillations about a center which is diffusing freely in space. If there is no dynamic correlation between the two types of motion, then the neutron scattering response function is approximately

$$S_i(Q,\omega) = \frac{1}{2\pi\hbar} \int_{-\infty}^{\infty} dt \exp(-i\omega\, t - Q^2 D_s |t|) \int d\underline{r} \exp(i\underline{Q} \cdot \underline{r}) G_s(\underline{r}, t) \qquad (7.16)$$

where D_s is the self diffusion constant, and $G_s(\underline{r}, t)$ describes the oscillatory motion. The response function (7.16) comprises a quasi-elastic contribution and a sum of inelastic terms centered about $\pm\omega_0$, $\pm 2\omega_0 \cdots$. Each contribution has an energy spread $\sim (\hbar Q^2 D_s)$. The quasi-elastic contribution to the response of this model is

$$\pi\hbar\, S^q(Q,\omega) = \left\{ \frac{Q^2 D_s}{\omega^2 + (Q^2 D_s)^2} \right\} \int d\underline{r} \exp(i\underline{Q} \cdot \underline{r}) G_s(\underline{r}, \infty)$$

$$= \left\{ \frac{Q^2 D_s}{\omega^2 + (Q^2 D_s)^2} \right\} \exp\{-2W(Q)\} I_0(y) \qquad (7.17)$$

where the $\exp(-2W(Q))$ is Debye-Waller factor and $I_0(y)$ is a Bessel function of the first kind of order zero with an argument

$$y = \hbar Q^2 / \left\{ 2M\omega_0 \sinh(\frac{1}{2}\hbar\omega_0\beta) \right\} \qquad (7.18)$$

The ω_0 in form (7.18) is the frequency of vibration. Equation (7.17) is Lorentz function, and it has a peak at $\omega = 0$ with the peak height proportional to $1/(Q^2 D_s)$, and the width at half peak height proportional to $Q^2 D_s$. From a supercooled liquid to glass state, the diffusion constant D_s will drop dramatically for a given a scattering vector.

The quasi-elastic scattering profile will show an increase of the peak height and a decrease in the width of the peak.

It must be pointed out that the quasi-elastic contribution (7.17) is distinct from the inelastic components of the spectrum centered at $\pm\omega_0$ only if $(Q^2 D_s) << \omega_0$, and this condition imposes a limitation on the value of the scattering vector. In other words, only if Q is very small and close to zero is the quasi-elastic contribution recognizable.

Experimentally, the observation of the quasi-elastic contribution also depends on the experimental resolution, because there is always a Gaussian peak at zero energy transfer ($\omega = 0$) predominantly determined by elastic incoherent scattering, whose width is completely determined by the experimental resolution.

It can be proved (Lovesey, 1984) that when the particle is not diffusing freely in space but jumping stochastically, the quasi-elastic scattering contribution is still taking Lorentz form with a term of

$$\frac{\gamma(Q)/t}{\omega^2 + (\gamma(Q)/t)^2}$$

where $\gamma(Q) = Q^2 l$, l is the length of jump when $Q \to 0$, and t is the residence time at a given site.

7.3   Experimental Details

The neutron diffuse scattering measurements were made using the triple axis neutron spectrometer (TAS) at the HIFAR research reactor, Lucas heights, Sydney, Australia Nuclear Science and Technology Organization (ANSTO).

The same neutron diffuse scattering measurements were repeated three times in a time span of two years, covering 1994, 1995, 1996 in an attempt to overcome the irreproducibility which is found very commonly in stabilized zirconia alloys (Yashima et al., 1994; Kandil et al, 1984). Each time, the measurement was lasting 2 to 4 weeks.

7.3.1   The triple axis spectrometer

A layout of a TAS is sketched in figure 7.1
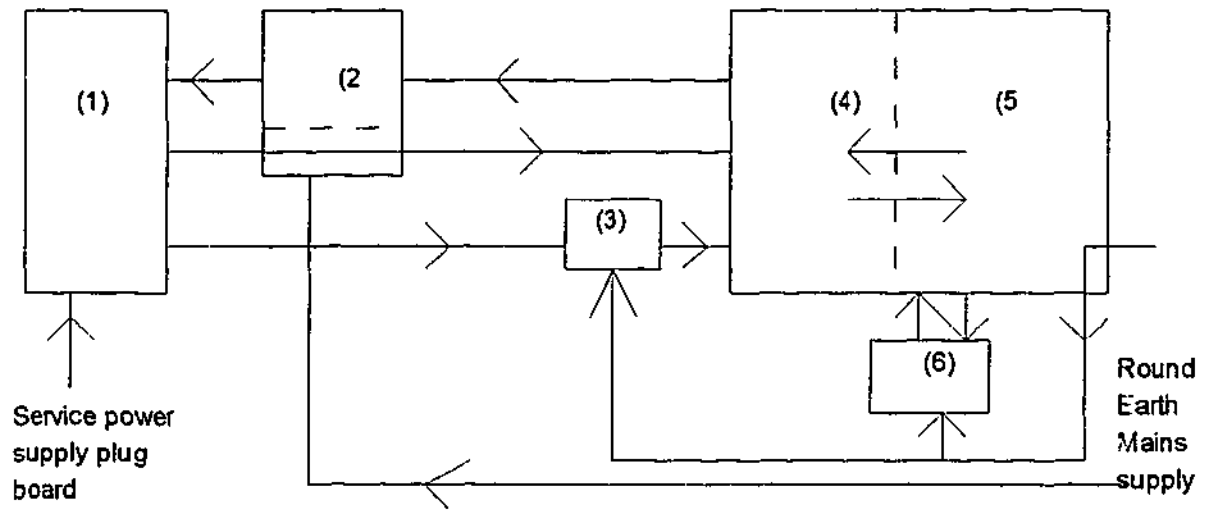
(1)   The actual instrument

(2)   The terminal box

(3)   The counting electronics

(4)   The interface

(5)   The control computer (PDP-8)

(6)   The teletypewriter.

Fig. 7.1   Connection logic of major components of Triple Axis Spectrometer.

There are three components in the actual instrument (refer to figure 7.2)

(I) The first axis (monochromator) - selects neutrons of one energy from the thermal neutron flux from the reactor.

(ii)   The se⁻ ₂nd axis (sample) - interaction point of the neutron with the sample.

(iii)   The third axis (analyser) - measures the energy of the scattered neutrons.
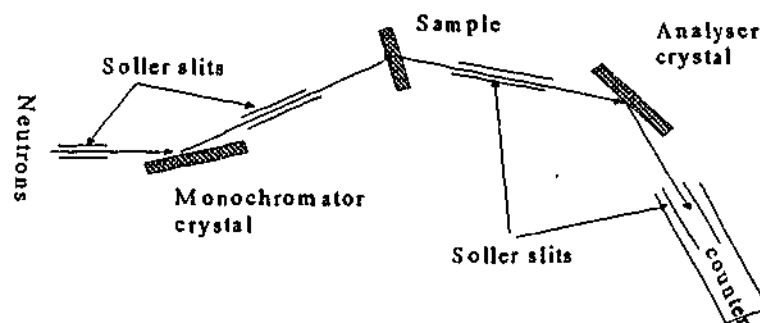
Fig. 7.2   A sketch of a Triple Axis Spectrometer.

The monochromator is a Cu crystal 5 cm x 8 cm x 1 cm thick with an [1$\bar{1}$0] axis vertical. It is set up so that a(111) plane scatters the neutron onto the sample. The neutron wavelength is given by Bragg's law $\lambda = 2d_m \sin\theta_m$ where $2\theta_m$ is the monochromator scattering angle. The neutron energy is given by $E = h^2 k^2/(2m_n)$ where $k = 2\pi/\lambda$. To vary the incident energy we can change $2\theta_m$ or we can change d_m. The angle $2\theta_m$ has well defined limits, 10-45° in range 1 and 45-80° in range 2. For our elastic diffuse scattering, the incident and scattering wave length is 1.7952 Å, which has an energy of 6.126 THz. For inelastic scattering, the scattering wave length is fixed at 1.7952 Å, but incident wave length, or the incident neutron energy was changed through the change of angle $2\theta_m$ from 54.2° to 48.9°, which corresponds to a wave length from 1.89 Å to 1. 73 Å, or energy from 5.53 THz to 6.63 THz.

As in the monochromator section, the analyzer uses the Bragg reflection from a crystal plane to select neutrons of a particular energy from the beam scattered by the sample. The analyzer is of pyrolitic graphite 2 inch x 3 inch x 1/16 inch thick using the 0002, 0004 or 0006 plane in reflection.

The sample is mounted on a large goniometer attached to the driven table. The sample can be mounted in a furnace or cryostat.

7.3.2   The Sample and sample mounting

Crystals of 15 mole % Y_2O_3-stabilised ZrO_2 were obtained from Ceres Corporation, Waltham, Mass.. The size of the crystal is about 2 cm x 2 cm x 3 cm with one face cut parallel to one of {110} planes. The angle between the normal of the face and [1$\bar{1}$0] direction is less than 1°, and the cutting was done in the Division of Manufacturing Science & Technology, CSIRO, Clayton.

The sample was mounted in a vertical tube furnace which sits on the goniometer. The construction is shown in Fig. 7.3.   The crystal was glued to the high temperature stainless steel mounter using high temperature cement with the [1$\bar{1}$0] zone axis vertical.

7.3.3 Furnace and temperature control

The furnace is a vertical tube type made by Ceramic Engineering, Sydney, with coiled kanthal heating elements around an alumina tube (Fig. 7.3). The internal diameter of the alumina tube is about 60 mm. A K-type thermocouple was inserted into the chamber from the top, and the sample was glued to its tip. We expect little temperature difference between the sample position and the thermal couple tube tip in this configuration. Temperature was controlled by an OXFORD ITC 503 controller with ±0.5°C of variation in isothermal treatment. The ramping rate in this experiment was about 4.5 °C /minute.
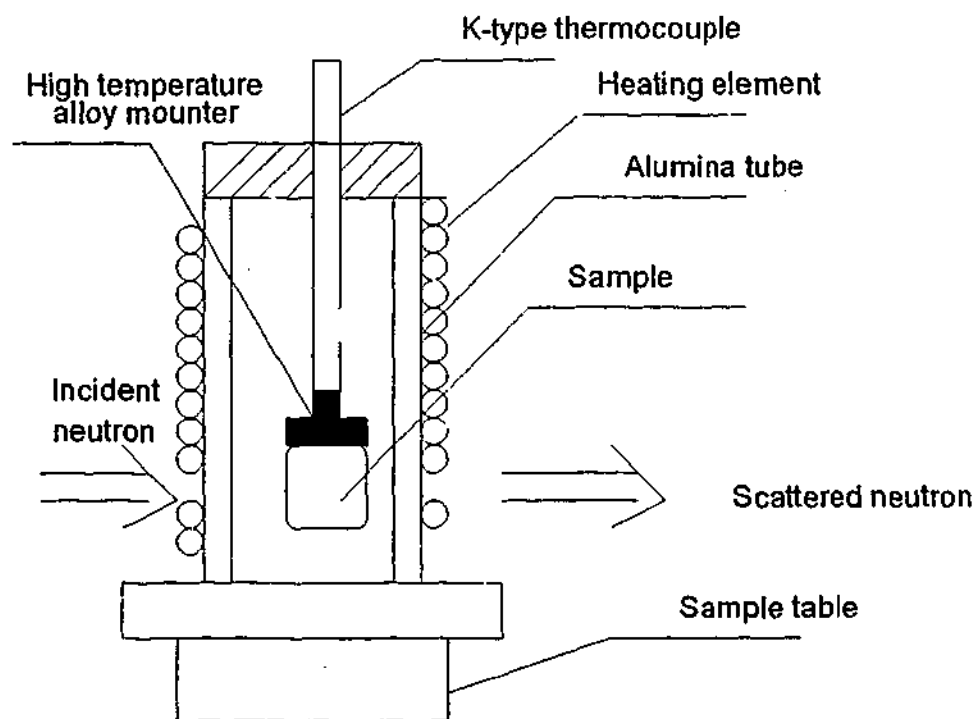

Fig. 7.3   Sketch of sample mounting and the furnace.

7.3.4 Measurements and data processing

The wavelength and energy selection for this experiment is mentioned in 7.3.1. Measurements were conducted at different temperatures, the heating rate between two temperatures is referred to in 7.3.3. At each selected temperature, both elastic diffuse

and inelastic diffuse scatterings were measured. Lattice parameter changes caused by thermal expansion at each temperature were properly incorporated so that all scattering calculations related the right lattice parameters were pursued.

Due to the limited two-circle geometry of the sample holder, we were restricted to measuring planes which pass through the origin. The zero layer of $[1\bar{1}0]$zone was chosen because it provides a large number of reciprocal space points, with a variety of reflection types (mixed and unmixed indices), than other planes available with this geometry. Elastic diffuse intensity was measured in the zero layer of the $[1\bar{1}0]$ zone at intervals of $\Delta h = \Delta l = 0.1$. Elastic diffuse intensities along specific lines were measured at intervals of $\Delta h = \Delta l = 0.01$. For the sake of time and our interest, most of the scan is limited in the area of $0.5 \leq h \leq 2.1$ and $0.7 \leq l \leq 2.5$. Inelastic diffuse intensity was measured at selected points in the zero layer of the $[1\bar{1}0]$zone at energy increment of 0.05 THz (0.21 meV).

The resolution of a triple axis spectrometer is related to the angular widths of the collimators found throughout the instrument as well as the mosaicity of the monochromator, analyser and sample crystals. The resolution function R (Q_x, Q_y, Q_z, ω) gives the probability of detecting a scattered neutron with wavevector $\underline{Q}$ and frequency ω. The observed intensity is given by:

$$I(\underline{Q}_0,\omega_0)=A\int S(\underline{Q},\omega)R(\underline{Q}-\underline{Q}_0,\omega-\omega_0,\underline{Q}_0,\omega_0)d\underline{Q}d\omega \qquad (7.19)$$

where $S(\underline{Q},\omega)$ is the scattering function, A is a constant incorporating the incident neutron flux and sample volume, R is the spectrometer resolution function, which is a four dimensional ellipsoid in $(\underline{Q},\omega)$ space (Hackett, 1987). The resolution function can be calculated with the help of a computer. In this experiment, given the scattering conditions, the energy resolution is about 0.35 THz (1.45 meV).

During the measurements powder reflections from the alumina furnace tube were recorded together with scattering from the sample. These reflections were singled out according to the known scattering angles for alumina, and removed from elastic scattering contour maps. For those quasi-elastic scattering measurements at specific points where alumina contamination are present, the intensity (neutron counts) are

7-10

presented in arbitrary units under the assumption that the contribution from alumina varies slowly with temperature.

Elastic diffuse scattering data were processed using computer program Winsurf Version 5.01 promoted by Golden Software. They are presented in the form of contours. Quasi-elastic scattering data were processed using a computer program written by Dr. Margaret. M. Elcombe of ANSTO. They were fitted with a Gaussian and a Lorentz function. Due to the limitation of the energy resolution of thermal neutrons, it was not possible to divide the quasi-elastic scattering into separate Gaussian and Lorentz components. The quasi-elastic scattering data were fitted very well by a single Gaussian function.

7.4   Experimental results

The contour maps of neutron diffuse scattering from 15 mole % Y_2O_3-stabilised zirconia crystal at different temperatures are shown in Fig. 7.4. Note that in subsequent graphical plots versus temperature, the straight lines are only meant as guides to the eye.

All diffuse scattering patterns show one diffuse scattering band from 1.6, 1.6, 0.7 to 1.4, 1.4, 1.7   There are three diffuse maxima. One is at 1.4, 1.4, 1.7, the others are

at approximately 1.6, 1.6, 1.3 and 1.6, 1.6, 0.7. Expressing the diffuse maxima as satellite vectors in the reciprocal space in terms of reciprocal lattice , they can be described as $\pm$ (0.4, 0.4, $\pm$ 0.7). These vectors are nearly the same as $\pm$ (0.4, 0.4, $\pm$ 0.8)   suggested by Hull et al. (1988), and Neder et al. (1990). One feature of the diffuse scattering patterns presented here is that the location of diffuse maxima at 1.4, 1.4, 1.7 does not move with temperature,   however the position of diffuse maxima close to 1.6, 1.6, 0.7 and 1.6, 1.6, 1.3 change with temperature. The maximum close to 1.6, 1.6, 0.7 jumps   between   1.6, 1.6, 0.7 and 1.7, 1.7, 0.7 at different temperatures   while the maximum close to 1.6, 1.6, 1.3 moves along 1.6, 1.6, 1.3 to 1.7, 1.7, 1.2. When temperature is below 650°C, the maximum is at 1.7, 1.7, 1.2, when temperature is higher than 650°C the maximum is at 1.6, 1.6, 1.3.   Fig. 7.5
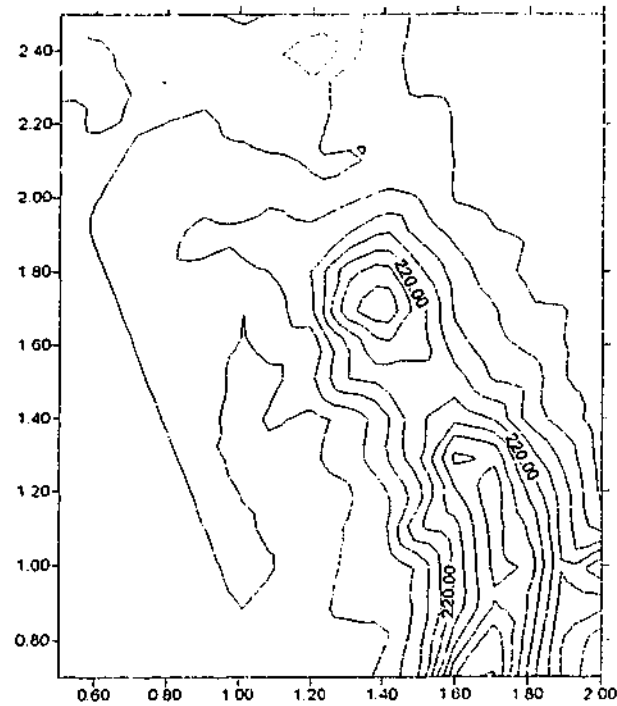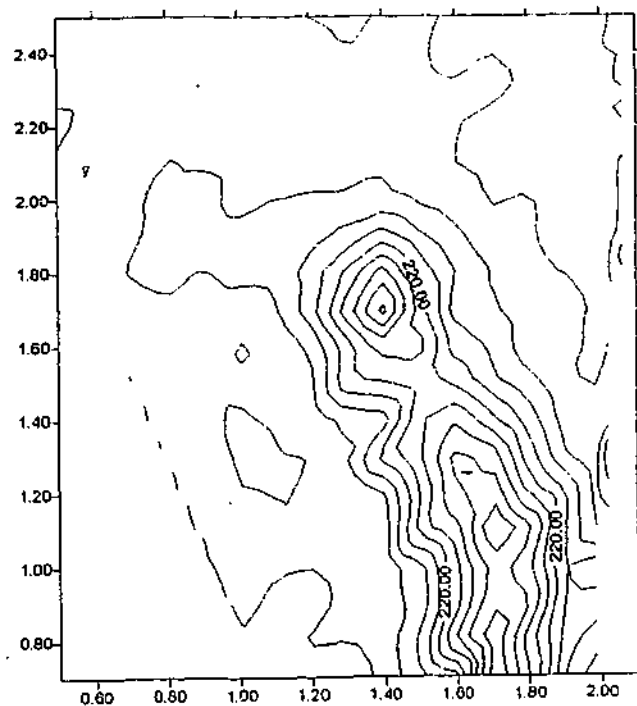
Figure 7.4 a - 7.4 b: Neutron diffuse scattering from the zero layer of the (1-10) plane a) at room temperature, b) at 450°C. The Bragg reflections have been masked out.
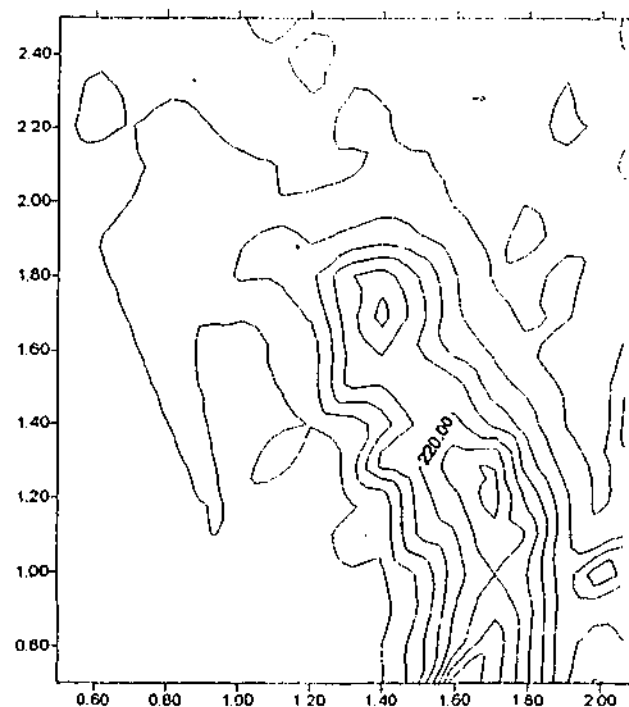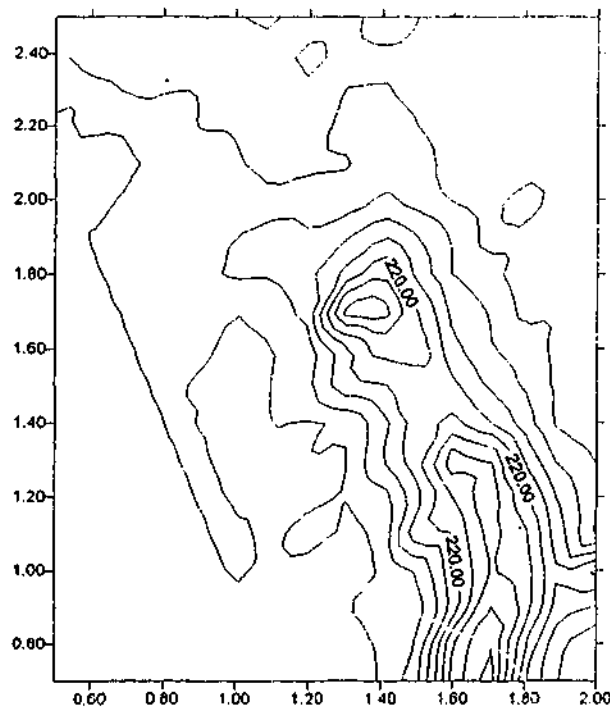
Figure 7.4 c - 7.4 d: Neutron diffuse scattering from the zero layer of the (1-10) plane c) at 550°C, d) at 600°C. The Bragg reflections have been masked out.
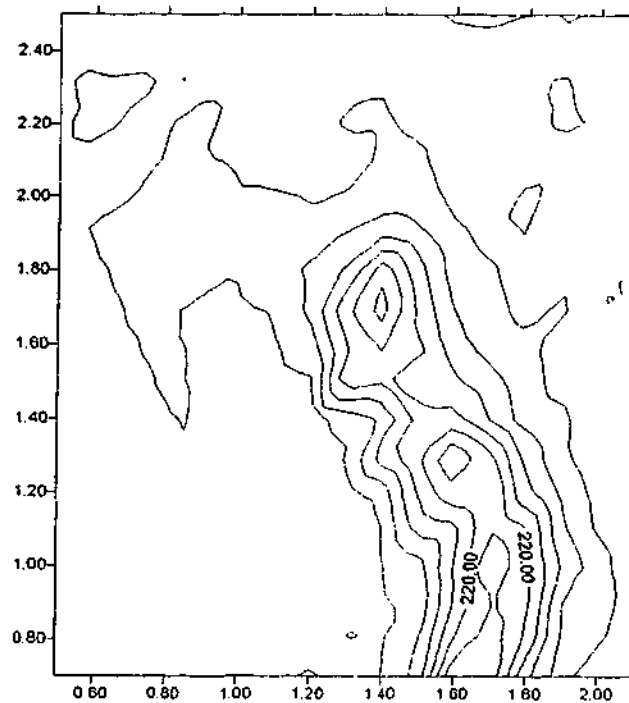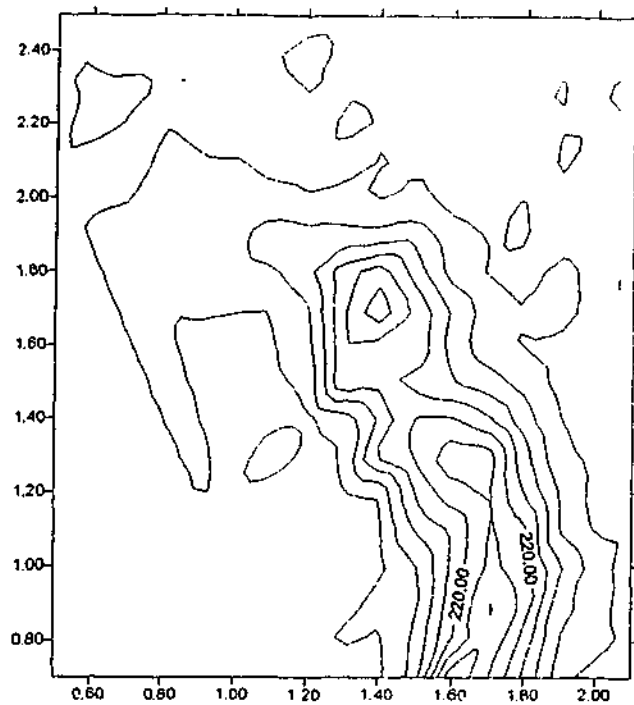
Figure 7.4 e - 7.4 f: Neutron diffuse scattering from the zero layer of the (1-10) plane e) at 650°C, f) at 700°C. The Bragg reflections have been masked out.
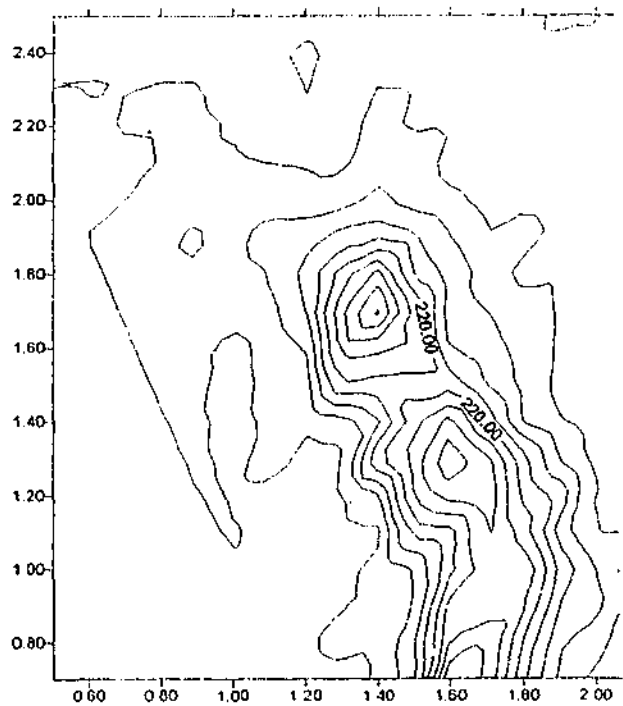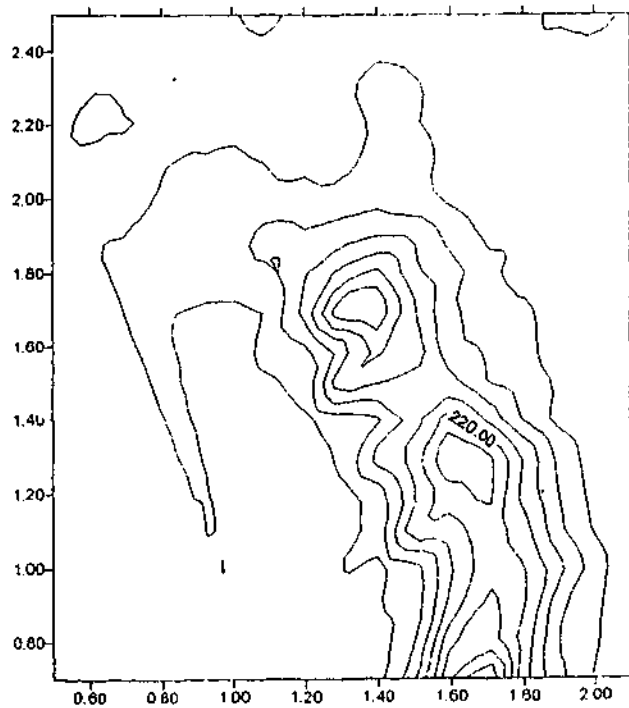
Figure 7.4 g - 7.4 h: Neutron diffuse scattering from the zero layer of the (1-10) plane g) at 750°C, h) at 800°C. The Bragg reflections have been masked out.
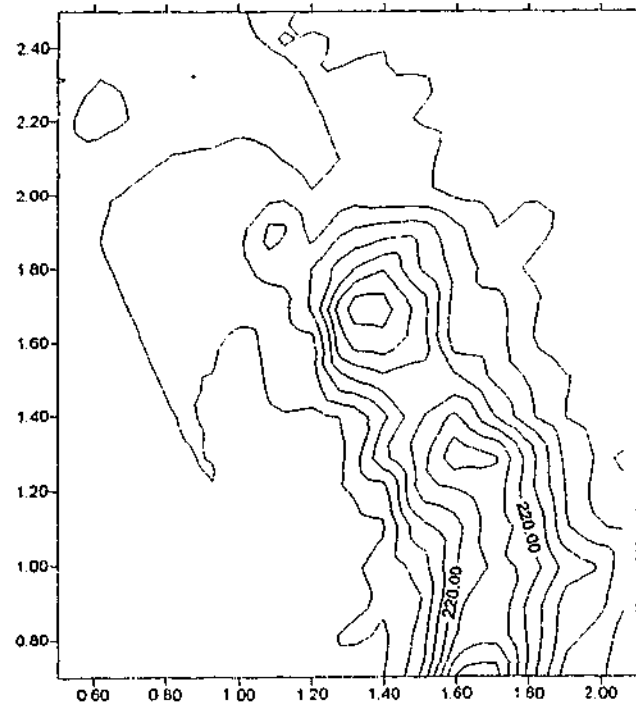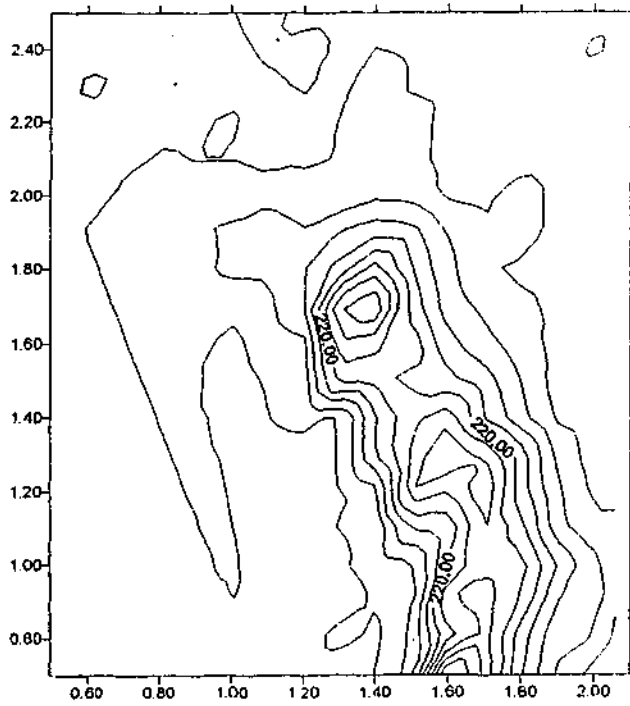
Figure 7.4 i - 7.4 j: Neutron diffuse scattering from the zero layer of the (1-10) plane i) at 850°C, j) at 900°C. The Bragg reflections have been masked out.

shows the scattering intensity at 1.6, 1.6, 0.7 and 1.7, 1.7, 0.7 as a function of temperature. It can be found that the diffuse intensities at these two points cross each other several times as temperature increases. Fig.7.6 shows the scattering intensity at 1.6, 1.6, 1.3 and 1.7, 1.7, 1.2 as a function of temperature. The diffuse intensity curves cross once at a temperature around 630°C.

Fig.7.7 shows the neutron diffuse scattering intensities at 1.4, 1.4, 1.7, and 1.6, 1.6, 1.3, and the intensity average over 1.6, 1.6, 0.7 and 1.7, 1.7, 0.7 as a function of temperature. It can be seen that all diffuse scattering intensities are low in the temperature range of 600°C to 750°C.

There is a significant amount of second-order contamination at the 112 Bragg position, so no forbidden reflection from tetragonal distortion could be claimed. Considering that the composition of our sample is not near the *c-t* phase boundary, any tetragonal reflection from tetragonal zirconia precipitates will be insignificant.

Diffuse scattering intensities of line scan in Q-space crossing over the diffuse maxima at 1.7,1.7,1.0, 1.4,1.4,1.7 and 0.6,0.6,3.7 were fitted with a Gaussian function. The FWHMs of the Gaussian fittings are taken as an indication of the microdomain sizes (Hackett, 1987). They are about 0.3 to 0.7 rlu (reciprocal lattice unit) corresponding to microdomain sizes of 2 to 3 lattice units in direct space (10 to 18 Å).

Results of quasi-elastic diffuse scattering are presented in the next section together with discussion.

7.5 Discussion

The data from several different types of neutron diffraction experiments conducted at various times will now be presented in graphical form.

7.5.1 Elastic diffuse scatter

As mentioned in section 7.2, Laue monotonic diffuse scattering is an average scattering independent of $\underline{Q}$. Apparently the diffuse scattering maxima shown in Fig.7.4 are localized. From the general theory mentioned in section 7.2, the diffuse scattering shown in Fig.7.4 must originate from static distortion.

As we discussed in chapter 6 that the defect structures in Y-CSZ could be described in terms of microdomains or nuclei of ordered γ-phase. These microdomains account for the neutron diffuse scattering maxima at vectors $\pm(0.4,0.4,\pm0.7)$. The Q-widths at 1.4, 1.4, 1.7 and 0.6, 0.6, 3.7 suggest that the microdomain sizes are about 2 to 3 lattice units (10 - 18 Å). We will briefly revisit the results reported by Hackett (1987), Hull et al (1988) and Proffen et al (1996) to show that Allpress-Rossell model is applicable and the microdomains are likely of γ-phase structure.

The elastic neutron diffuse scattering patterns reported by Hackett (1987), Hull et al. (1988), Proffen et al. (1996) are very similar to those in this thesis although they reported diffuse scattering maxima at $\underline{Q} = \tau_f \pm (0.4, 0.4, \pm 0.8)$ rather than $\underline{Q} = \tau_f \pm (0.4, 0.4, \pm 0.7)$ in some reason (Hackett, 1987). Hackett and Hull et al. attributed the "satellite" peaks to those aggregates embedded in the distorted cubic fluorite matrix. The size of the aggregates was estimated about three fluorite unit cells (~16 Å). They suggested that the structure of aggregates comprise "Bevan Clusters" in which vacancy pairs are separated by $\frac{1}{2},\frac{1}{2},\frac{1}{2}$ lattice vector across a cation.

"Bevan Cluster" is a feature of the ordered δ-phase, such as $Zr_3Sc_4O_{12}$ and γ-phase $Zr_5Sc_2O_{13}$ (Thornber, Bevan & Summerville, 1970). But stoichiometrically, see Ruh et al. (1977), the γ-phase (in the Sc-CSZ, 15 to 23 mole % Sc_2O_3) has a phase region closer to the composition range of YSZ samples in our experiments than the δ-phase (24 to 40 mole %).

Proffen et al. (1996) described the defect structure of Ca-CSZ in terms of two types of microdomains within the cubic matrix of CSZ, microdomains based on a single vacancy with relaxed neighbouring ions and microdomains based on oxygen vacancy pairs separated by $\frac{1}{2},\frac{1}{2},\frac{1}{2}$ lattice vector. Cations are ordered in the

microdomains in a way that all cations next to oxygen vacancy are zirconium, according to Proffen et al. (1996)

There is no radical difference between the defect structures proposed by Proffen et al.(1996) and Hackett (1987) except that the former used the name "defect aggregates" and the later took the name of "microdomains".

As we summarized in chapter 2, Literature Review, that for a given cation valence, say trivalent, the larger the radius difference between the dopant cation and the host cation is, the more difficult the formation of ordered intermediate phases in that system will be. We believe that such a difficulty results in smaller size of microdomains formed in the Y_2O_3-ZrO_2 system. For the Y_2O_3-ZrO_2, the ionic radius of Y is relatively larger than that of Zr, in comparison with Sc.

In Fig.7.5 the diffuse scatter at reciprocal space positions 1.6,1.6,0.7 (=1.6^2, 0.7) and 1.7,1.7,0.7 (=1.7^2, 0.7) are displayed as a function of temperature. Diffuse scatter in this region is believed to be due to the "single-vacancy" defect identified by Hull et al (1988). The overall intensity of the diffuse elastic scatter for both reflecting positions (1.6^2, 0.7) and (1.7^2, 0.7) is similar over our supercooling range between T_g and T_m . The two intensity curves, however, appear to be out of phase, crossing each other several times. This may mean that the oxygen lattice in which the vacancy defect resides may relax as a modulated structure whose wave vector changes with temperature. This is a somewhat speculative conclusion and has no direct consequences for the remainder of the work in this thesis.

The elastic diffuse scatter at the closely-spaced positions 1.6,1.6,1.3 and 1.7,1.7,1.2 are considered to arise from the microdomains or reorientable species (called "aggregates" by Hull et al (1988)). They are roughly the same shape and amplitude, with a strong dip it ... intensity centered on a temperature value of $\approx 650°C$. Though crossing twice in Fig. 7.6 this appears to suggest that the aggregates themselves soften when approaching the orientational glass transition from above and stiffen when in the mode-coupling regime below 650°C.

In Fig. 7.7, the elastically diffracted neutron intensities from two different "sources" are displayed. Diffuse peaks 1.4, 1.4,1.7 and 1.6, 1.6, 1.3 are believed by Hull et al to arise from the "aggregates". The third plot in Fig. 7.7 is an intensity average over 1.6,

Diffuse scattering at 1.6, 1.6, 0.7, and 1.7, 1.7, 0.7

Fig. 7.5
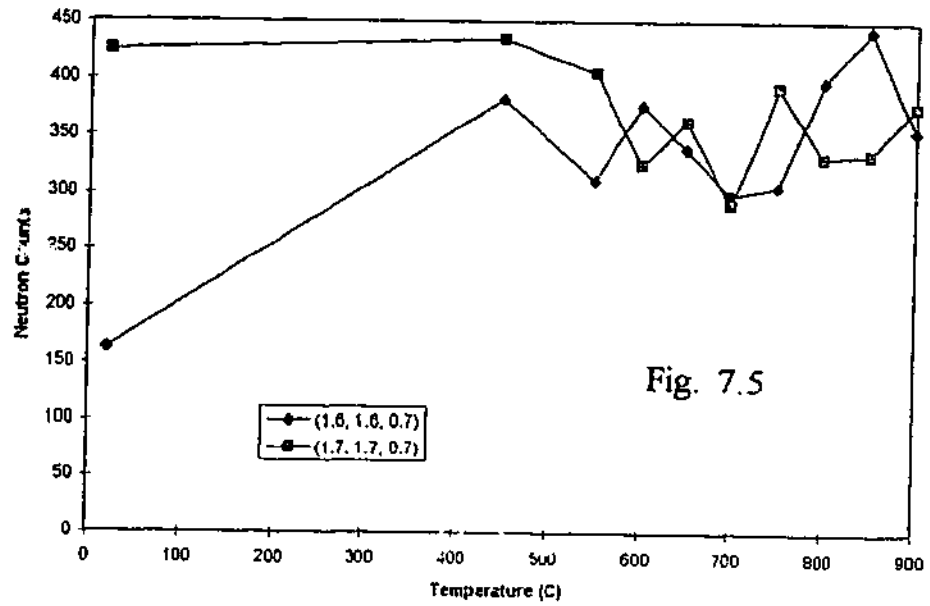
Neutron diffuse scattering at 1.6, 1.6, 1.3 and 1.7, 1.7, 1.2

Figure 7.6
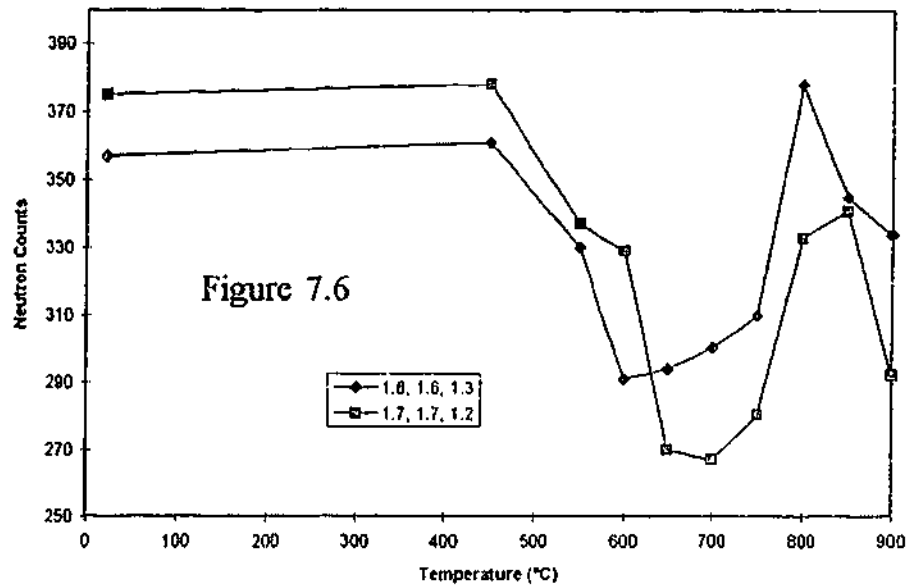
Neutron diffuse scattering intensities at 1.4, 1.4, 1.7   1.6, 1.6, 1.3
and intensity average over 1.6, 1.6, 0.7 and 1.7, 1.7, 0.7 —△—#

Figure 7.7

7-18
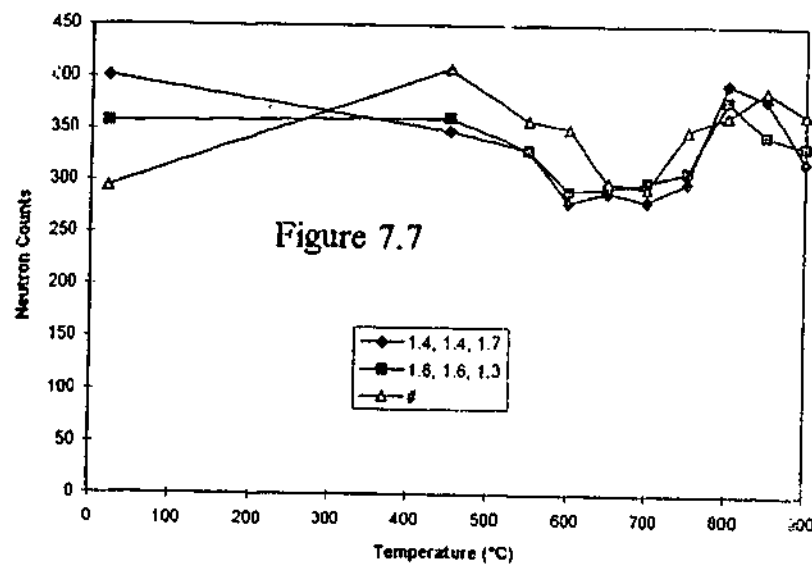
1.6, 0.7 and 1.7, 1.7, 0.7, which are believed to arise from the single oxygen vacancy defect, though with alternating intensity, as shown in Fig. 7.5. Although from two different sources, these four reflections have similar wave vectors and so would not furnish a test for the wave number (or wave length) independence hypothesis. It is clear however that above 450°C, they all behave similarly in the mode-coupling and T_m regions.

7.5.2   Quasi-elastic diffuse scattering

Examples of quasi-elastic diffuse scattering at 200°C are displayed in Fig. 7.8. Due to the limitation of resolution, the data can only be fitted with a Gaussian function. No energy-broadened Lorentzian scattering can be resolved. Results of intensity and full width at half maximum (FWHM) obtained in 1994 are shown in Fig. 7.9 and 7.10 as a function of temperature. Nonetheless, we have plotted Gaussian functions as approximations to the intensity and energy broadening as functions of temperature.

In Fig. 7.9 are plotted the quasi-elastic scattering intensity from diffuse diffraction corresponding to the three distinct sources identified by Hull et al (1988). Although the region of reciprocal space near the reflecting position 1.2, 1.2, 1.8 due to the tetragonally-distorted cubic matrix is contaminated by scatter from the alumina components of the furnace, on the assumption that alumina does not also exhibit sharp changes in quasi-elastic diffuse scatter due to phase transitions at the same temperatures as those we are studying in Y-CSZ, we take any sharp change observed to be due to the Y-CSZ.

With this proviso, Fig. 7.9 (a) appears to indicate that a "square root cusp" quasi-elastic intensity curve is visible in the region 700°C-450°C which is, as we claim, the mode-coupling region for Y-CSZ, i.e., the "bottom half" or so of the supercooling region. The quasi-elastic intensity peaks at a value near T_g (~420°C) in this material; although measurements are sparse in this range we take this behaviour to indicate that the intensity-temperature curve plotted in Fig. 7.9(a) from quasi-elastic scattering near 1.2, 1.2, 1.8 represents the Edwards-Anderson order parameter in the supercooling range of the MCT regime.

Quasi-elastic diffuse scattering at 1.7,1.7,1.0 at 200 °C
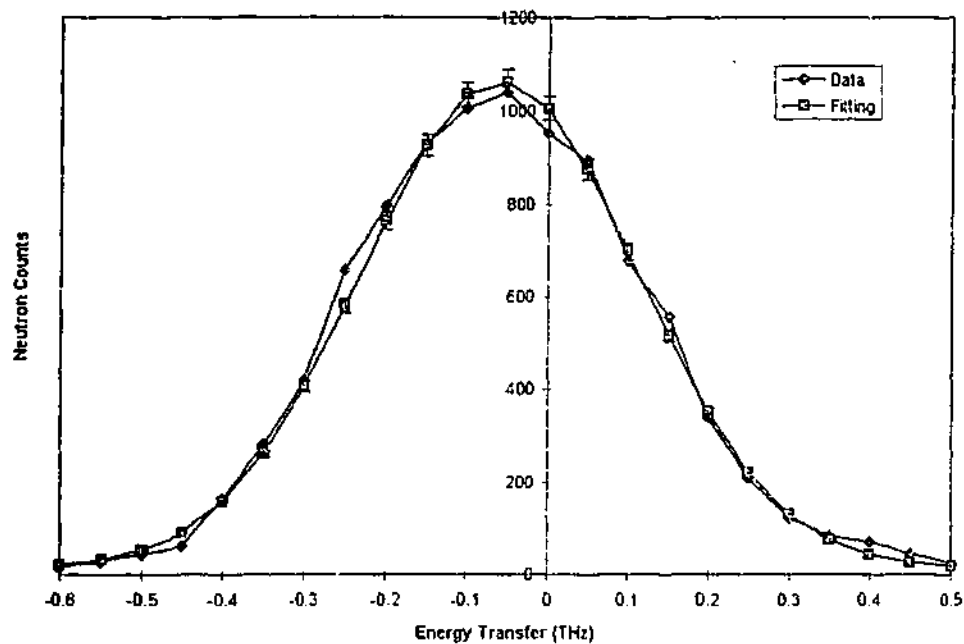
Quasi-elastic diffuse scattering at 1.4,1.4,1.7 at 200°C
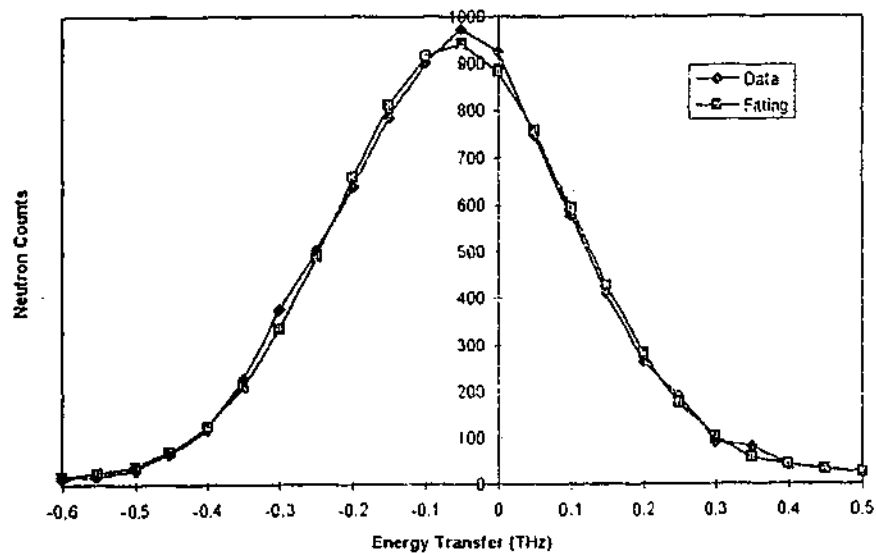
Quasi-elastic diffuse scattering at 1.4, 1.4, 3.7 at 200 °C

7-20
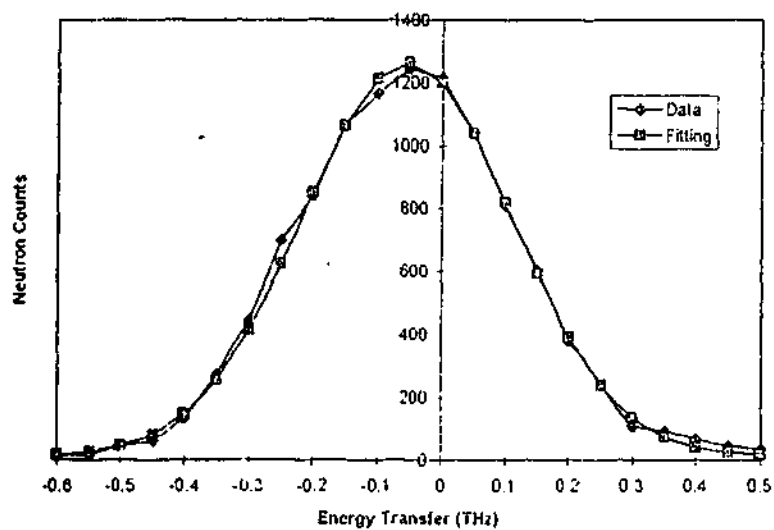
In Fig. 7.9 (b), the diffuse scatter which Hull et al (1988) associated with the "aggregates" (and which we associate with the reorientable rotating species, e.g., $CaZr_4O_9$ in the Ca-CSZ case) exhibits a peak in the range of the mode-coupling but no peak in the vicinity of T_g, in line with the idea that the calorimetric or dilatometric glass transition is a kinetic phenomenon in the "liquid" (rather than among the rotating species). Here, the "liquid" is taken to be the tetragonally-distorted cubic matrix (as outlined in chapter 3) or "domain wall" region, through which the vacancies and oxygen ions are considered to flow in support of ionic conduction.

Fig. 7.9(c) is quasi-elastic intensity at 1.6,1.6,1.0. It displays good evidence for the structural concept that the "single-vacancy" region of Hull et al (1988) and the tetragonally-distorted cubic regions between the rotator microdomains (i.e., the "domain wall" areas) are intimately related, or indeed that the "single-vacancy" region is actually contained in the tetragonally-distorted region, and that the two are essentially parts of the same entity. The 1.6,1.6,1.0 quasi-elastic intensity plot follows closely that of the "tetragonal" 1.2,1.2,1.8 Edwards-Anderson order parameter shown in Fig. 7.9(a), except that the vestiges of the square-root cusp in Fig. 7.9 (c) do not appear until about 600°C, about 50°C below the region of the Leutheusser temperature T_L, where the "aggregates" freeze into antiferroelastic "tees".

The full-widths at half maxima (FWHM) of the quasi-elastic scatter from Hull et al's (1988) three distinct regions are displayed in Fig. 7.10. As remarked earlier, we will use the same interpretation for the widths of the fitted Gaussian peaks as for Lorentzian peaks, i.e., that a widening of the distribution in energy corresponds to an increase in the self-diffusion coefficient and hence to a softening of the material.

Fig. 7.10(a) demonstrates that for the "single-vacancy" defect, the material softens between 800°C to about 600°C as the orientational glass (OG) transformation nears among the "aggregates", then re-hardens as the temperature falls between 600°C and 500°C.

Fig. 7.10(b), corresponding to the "aggregates" 1.4, 1.4, 1.7, shows their FWHM appearing to behave in the opposite way from Fig. 7.10(a). As in Fig. 7.9, such behavior is believed to be due principally to the various stages of structural arrest occurring at slightly different temperatures. The aggregates begin to stiffen from about 600°C. The orientational glass (OG) transition, it should be recalled, is the triggering

Quasi-elastic diffuse scattering

Fig. 7.9(a)

"tetragonal" 1.2,1.2,1.8 Edwards-Anderson order parameter

Fig. 7.9 (b)
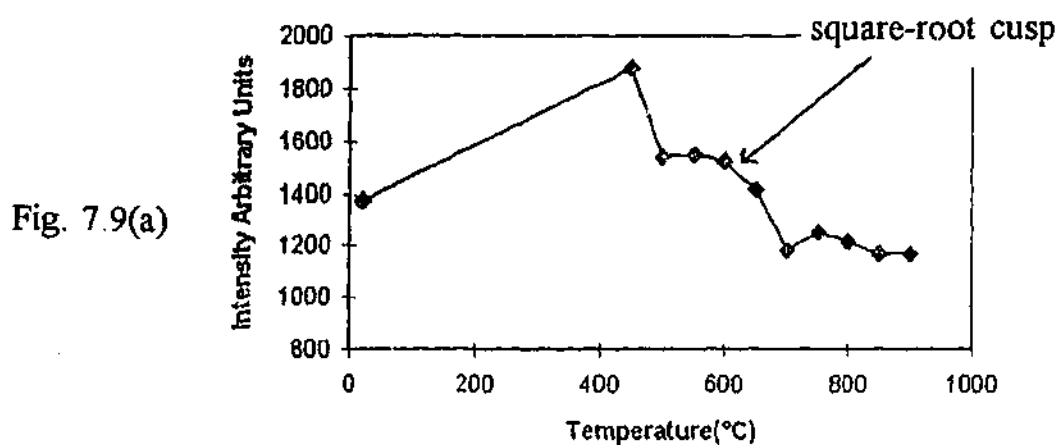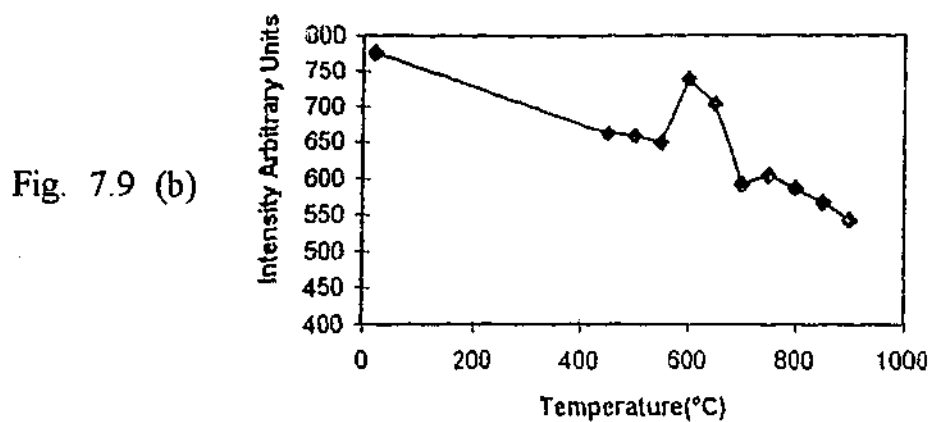
1.4, 1.4, 1.7,   "aggregates"

Fig. 7.9(c)
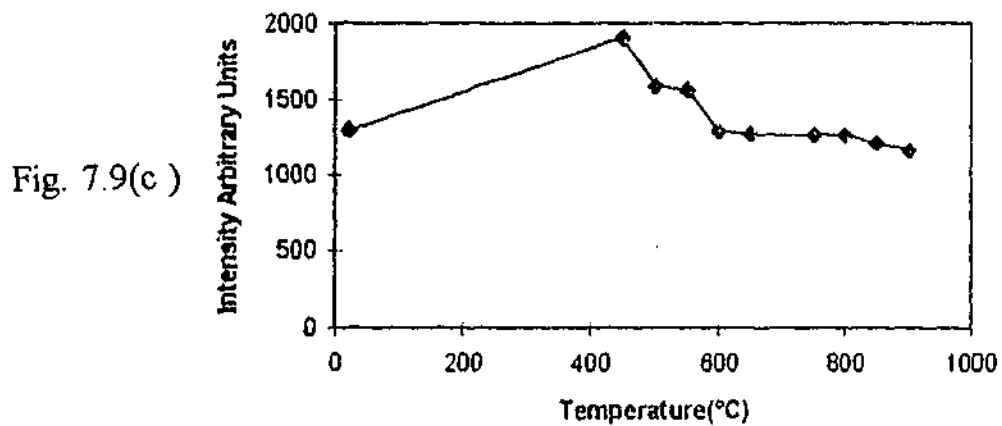
1.6,1.6,1.0   "single-vacancy" region

step (on cooling) for all the later events occurring at lower temperatures, recorded from the diffuse peaks corresponding to the structural arrest of the inter-microdomain tetragonally-distorted cubic zirconia matrix and of the "single-vacancy" conducting defect in its turn.

Within the error bars as shown, in Fig. 7.10 (c), the FWHM of the quasi-elastic scatter at 1.2, 1.2, 1.8 attributable to the tetragonally-distorted cubic matrix follows closely that of the "single-vacancy" defect shown in Fig. 7.10(a) in line with our earlier discussion of their interrelation. The re-stiffening on cooling occurs from about 700°C in the tetragonally-distorted cubic zirconia at the approximate temperature of the OG transition, while the arrest of the single-vacancy defect occurs about 50°C lower.

7.6   Conclusion

From the neutron diffraction experiments reported on in this chapter, it seems reasonable to make the following claims:

1. That neutron diffraction data was recorded from various reflecting positions in reciprocal space as a function of temperature, giving results which are in agreement with the high-temperature results of Hull et al (1988), i.e., the subdivision of the scattering into three separate types.

2. That one set of neutron diffraction data recorded in the present series was internally consistent with the mode-coupling hypothesis that the reorientable rotating species (Hull et al's "aggregates") undergo a phase transition near our proposed Leutheusser temperature T_L of ~650°C, which triggers a partial structure arrest of the tetragonally distorted cubic matrix material.

3. The structural arrest above, signalled by the "square-root" cusp behavior of the quasi-elastic intensity near 1.2,1.2,1.8 is symptomatic of non-ergodicity in the material, which ultimately causes the arrest of the mobile "single (oxygen) vacancy" defect as signalled by the similarity of the corresponding diffraction behavior at 1.6,1.6,1.0 to that of the cubic matrix. As the temperature falls toward T_g, the correlation length grows and the arrest becomes stronger. This scenario,

Fig. 7.10(a)
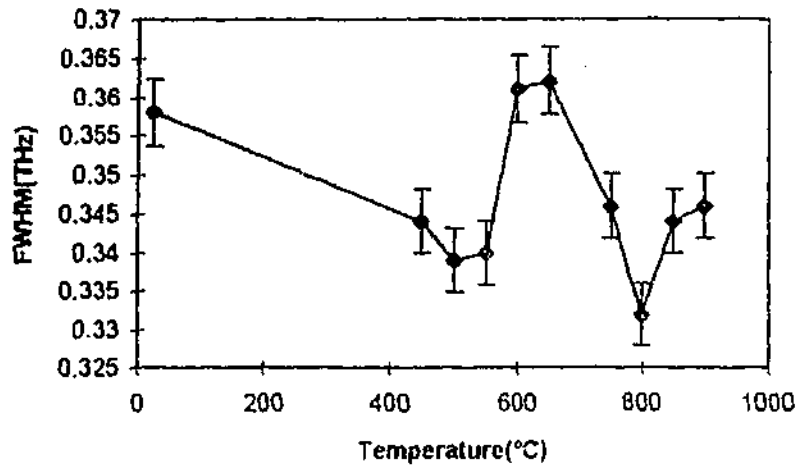
1.6,1.6,1.0.

Fig. 7.10(b)
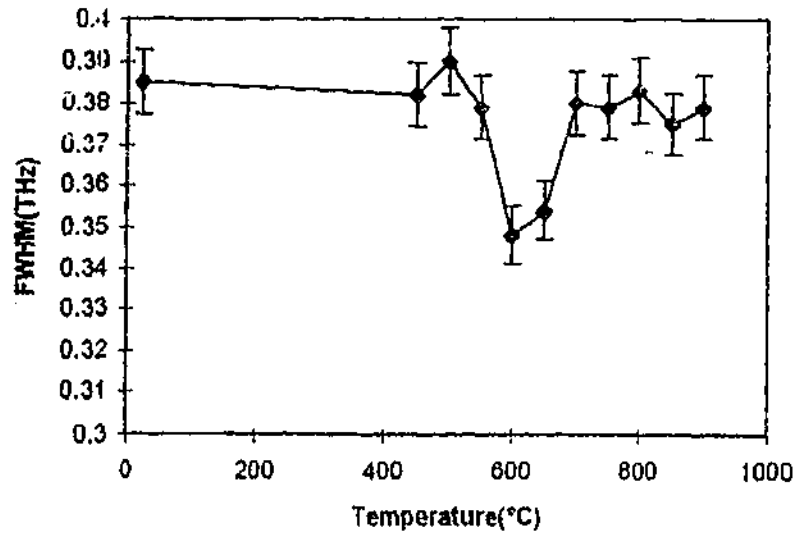
1.4, 1.4, 1.7,

Fig. 7.10 (c)

1.2, 1.2, 1.8

7-24
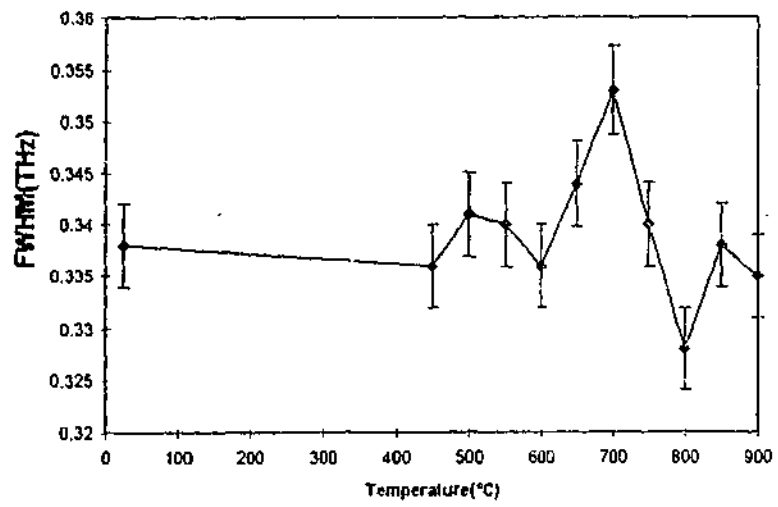
first put forward in chapter 3, appears to support our suggestion that the data furnishes a consistent, independent evidence for a glassy on-off ion conductivity mechanism.

It should be noted, however, that a self-consistent set of neutron diffraction data like the set described above in support of the MCT interpretation was not obtained from a similar large single crystal in experiments conducted one year later. Since each experiment is expensive and takes a long time, it was not possible in the time available to investigate the effect on the transition of long-range elastic fields due to the differing sizes and shapes of single crystals. For the present we have no explanation for the apparent irreproducibility.

CHAPTER 8

SUMMARY AND CONCLUSION

Since each of the preceding chapter has contained its own conclusions, a brief summary of the experimental results and their significance for the thesis that cubic stabilized zirconia can be looked upon as a glass is given here.

In chapter 4 we saw that simple dilatometric and calorimetric experiments conducted on CSZ indicate that a glass transition sets in at about 400°C and that near 650°C a hitherto undetected phase transition occurs, which accompanies sharp changes in transport properties. This was interpreted as the Leutheusser or mode-coupling onset temperature.

Of the diffraction experiments, one of the main results of chapter 5 is that, if the Allpress-Rossell model is valid for CaSZ and something similar is true for YSZ, then a simple concentration series of electron diffraction patterns should be able to identify with reasonable accuracy which diffraction features are due to dopant-rich and dopant-poor defects. It was found that the $1\bar{1}2$-type diffraction spots no longer appear beyond a Y_2O_3 molar doping of 12%; hence, they arise from the tetragonally-distorted cubic matrix between the microdomains which is likely to shrink in volume (relatively) on addition of dopant. As we have seen, these spots are not attributable to double diffraction effects but are directly related to the elastic stress due to the orientational glass-type coupling among the reorientable domains. Their disappearance at temperatures above T_m (~1000°C), when Bragg spots with wavenumber of similar magnitude are still strong, is evidence for a decoupling of the microdomains under an Edwards-Anderson interpretation of the elastic "spin" interactions: i.e., a highly mobile state for the oxygen ion vacancies since the rotors are now paraelastic.

The main powder X-ray diffraction results were of two kinds: one temperature series conducted using Cu radiation and another using Mo radiation. The Cu diffraction results demonstrated that if the Debye-Waller function for 12-YSZ were due to thermal effects only, it would appear to have the unusual property of not being a sensitive function of

temperature and wavevector since, considered experimentally as a function of temperature at constant wavevector, it appears to change little over a wide range of temperature and for three Bragg reflections. Under the mode-coupling hypothesis, this is the behaviour of a Debye-Waller factor due to static disorder which grows with the Edwards-Anderson order parameter as temperature falls, as outlined in chapter 3. The Mo radiation results demonstrate that symmetry breaking can be detected as the temperature falls below T_m and that the line phase identified by this method appeared to be similar to the γ-phase of the Sc-CSZ system. (Recall that for an OG-type theory to have any chance of working it was necessary that the line phase be able (in principle) to orient coherently in several equivalent directions on the average cubic lattice.)

The neutron diffraction results appeared to confirm that the diffuse diffraction features could be accounted for by the subdivision of defects into three separate types due to Hull et al. (1988), corresponding to the microdomains, the tetragonally-distorted matrix regions and the oxygen ion vacancy. A consistent set of experimental results was found which lend strong support to the mode-coupling hypothesis. i.e., that an antiferroelastic phase transformation occurs among the rotatable microdomain "cages" near 650°C, which then initiates the structural arrest or "locking" of the tetragonal matrix and, under the Allpress-Rossell scheme, the subsequent arrest of the mobile oxygen vacancies. This sequence of events is our picture for ionic conduction in CSZ. The key observation in these experiments is the appearance of the "square-root-cusp" in the Edwards-Anderson order parameter, here proportional to the intensity of the $1.2^2\ 1.8$ diffuse scatter from the tetragonally distorted cubic matrix.

While this thesis was being prepared for binding, an updated and extended version of Hull et al.'s 1988 paper on neutron diffraction from cubic stabilized zirconia appeared in print (Goff et al., *Phys. Rev. B*, June 1999). This extremely informative new paper, while making no mention of spin glasses etc., studies essentially the same range of Y_2O_3-doped single crystals as the ones described here in chapter 5, i.e. nominal dopant concentrations of 9, 12, 15, 18, 21 and 24 mole% Y_2O_3, with neutron and X-ray diffraction patterns recorded at room temperature, 900°C, 1280°C and 1530°C, i.e., far from the temperature ranges we considered to include the glass (T_g) and mode-coupling transitions. The new

8-2

results confirm Hull et al.'s 1988 deductions regarding the origin of the three different types of defect, i.e., the "aggregates", the tetragonally distorted regions and the single oxygen ion vacancies, upon which we have based our discussions in chapter 7.

Several new points are made as well. Goff et al agree that the vacancies "trapped" within the aggregates/microdomains contribute little to the oxygen ion conduction in agreement with the Allpress-Rossell model. It is also claimed that vacancy pairs may contribute to the conductivity as well as the single vacancies and that the diffuse scatter from the aggregates does not broaden in energy transfer at high temperatures, limiting the average measured period of paraelastic "spin-flip" for the aggregates to a period longer than 10^{-10} sec. It is stated in Goff et al that the aggregates/microdomains grow in size slightly as the amount of dopant rises, with a value of approximately 10 Å for a 15-YSZ specimen, in agreement with the Q-width measured for the microdomains in our neutron diffraction experiments, as judged by Gaussian fits to the elastic diffuse scatter. Goff et al also find that the amount of "aggregate" scattering increases and that from the tetragonal regions falls as the yttrium doping level increases, in agreement with the Allpress-Rossell model.

More interestingly, they claim that the aggregates/microdomains may be closely modelled by the structure of the Sc-CSZ line phase δ ($Zr_3Sc_4O_{12}$, S.G. $R\bar{3}$), rather than the γ-phase ($Zr_5Sc_2O_{13}$) determined from anomalous X-ray diffraction in chapter 6. Since both these phases (and the β-phase) are rhombohedral and hence reorientable type-B defects in the VKZ scheme, there is no conceptual difficulty here about "what is rotating" as long as the effective anisotropy in the CSZ is such as to yield a six-state orientational glass of VKZ-type C at criticality i.e. at the phase transition.

In any case, it may well be that any one of (or all of) the Sc-CSZ line phase analogues will be found coherently precipitated in YSZ at low temperature, depending metastably on the thermomechanical history of the sample.

Finally, Goff et al (1999) remark that the conduction mechanisms for Y-CSZ and Ca-CSZ must be very different, since the diffuse scatter from Ca-CSZ does not change significantly with temperature compared with Y-CSZ and shows no evidence for quasi-elastic broadening. In line with our assertion that the Allpress-Rossell model describes the structure of both systems well, we claim that the apparent discrepancy is due to the fact

that T_g for Ca-CSZ is approximately 900-1000°C (as remarked in several references mentioned in chapter 5) nearly 500°C above that for Y-CSZ, and that there is essentially no difference in conduction mechanism, only a difference in glass transition temperature.

REFERENCES

Abelard, P., and Baumard, J. F., (1982), *Phys. Rev.*, B26, 1005.

Ackerman, D. A., Moy, D., Potter, R. C., Anderson, A. C. and Lawless, W. N., (1986), *Phys. Rev. B*, 23 , 3886.

Allpress, J. G., Rossell, H. J., and Scott, H. G., (1975), *J. Solid State Chem.*, 14, 264.

Allpress, J. G., and Rossell, H. J., (1975), *J. Solid State Chem.*, 15, 68.

Angell, C.A., (1988), *J. Phys. Chem. Solids*, 49, 863.

Andersen, N. H., Clausen, K., Hackett, M. A., Hayes, W., Hutchings, M. T., Macdonald, J. E. and Osborn, R., (1986), *Physica*, 136B, 315.

Argyriou, D. N., (1994), *"Neutron Scattering From Zirconia And Zirconia Ceramics,"* Ph.D. Thesis, University of Technology, Sydney.

Badwal, S. P. S., and Swain, M. V. J., (1985), *Mater. Sci. Lett.*, 4, 487.

Baufeld, B., Bartsch, M., Messerschmidt, U., and Baither, D., (1995), *Acta Metall. Mater.*, 43, 1925.

Bengtzelius, U., Götze, W. and Sjolander, A., (1984), *J. Phys. C: Solid State Phys.*, 17, 5915.

Brandon, D. G., and Chaim, R., (1984), *Science and Technology of Zirconia II. Advances in Ceramics* Vol.12, Edited by N. Claussen, M. Ruhle and A. Heuer. The Amercan ceramics Society, pp 86-95.

Carter, R. E, and Roth, W. L., (1968), *EMF Measurement in High Temperature Systems*, Edited by C. B. Alcock. The Institute of Mining and Metallurgy, New York, pp 86-95.

Chen, Y., and Sellar, J. R., (1996), *Solid State Ionics*, 86-88 , 207.

Chung, D.D.L., De Haven, P.W., Arnold, H. and Ghosh, D., (1993), *X-ray Diffraction at Elevated Temperatures*, VCH (New York).

Cowley, J. M., (1981), *Diffraction Physics*, North-Holland Publishing Company, Amsterdam.

Cullity, B.D., (1978), *Elements of X-ray Diffraction*, 2nd Ed., Addison-Wesley, New York.

Dai, Z. R., Wang, Z. L., Chen, Y. R., Wu, H. Z., and Liu, W. X., (1996a), *Phil. Mag. A*, 73, 415.

Dai, Z. R., Wang, Z. L., and Liu, W. X., (1996b), *Phil. Mag. A*, 73, 1685.

Dwivedi, A., and Cormack, A. N., (1990), *Philos. Mag.*, A61, 51.

Donth, E., (1982), *J. Non-Cryst. Solids*, 53, 325.

Duclot, M., Vicat, J., and Deportes, C., (1970), *J. Solid State Chem.*, 2, 236.

Duran, P., Recio, P., and Rodriguez, J. M., (1987), *J. Mater. Sci.*, 22, 4348.

Edwards, S. F. and Anderson, P. W., (1975), *J. Phys. F: Metal Phys.*, 5, 965.

Etsell, T. H., and Flengas, S. N., (1970), *Chem. Rev.*, 70, 339.

Faber, Jr., J., Mueller, M. H. and Cooper, B. R., (1978), *Phys. Rev. B*, 17, 4884.

Fisher, K.H., and Hertz, J.A., (1991), *Spin Glasses*, Cambridge U.P.

Fischer, E. W., (1993), *Physica A*, 201, 183.

Franosch, T. and Götze, W., (1994), *J. Phys.: Condens. Matter*, 6, 4807.

Garvie, R. C., (1976), *J. Mater. Sci.*, 11, 1365.

Goff, J.P., Hayes, W., Hull, S., Hutchings, M.T. and Claussen, K.N., (1999), *Phys. Rev.B*, 59, 14203.

Goodman, C. H. L., (1975), *Nature*, 257, 370.

Götze, W., (1985), *Z. Phys. B: Condens. Matter*, 60, 195.

Götze, W. and Sjögren, L., (1992), *Rep.Prog.Phys.*, 55, 241.

Grannan, E. R., Randeria, M., and Sethna, J. P., (1988), *Phys. Rev. Lett.*, 61, 1402.

Grannan, E. R., Randeria, M., and Sethna, J. P., (1990), *Phys. Rev.*, B41, 7784.

Grimsditch, M., and Rivier, N., (1991), *Appl. Phys. Lett.*, 12, 1625.

Gross, D. J., Kanter, I. and Sompolinsky, H., (1985), *Phys. Rev. Lett.*, 55, 304.

Hahn, T., (ed.), (1989), *International Tables for Crystallography*, 2nd rev. ed. Vol. C, Published for The International Union of Crystallography by D. Reidel, Dordrecht, Holland, Boston, USA.

Hackett, M. A., (1987), *"Neutron Scattering Studies of Fluorite Compounds,"* PhD
Thesis, Oxford University.

Hellmann, J. R., and Stubican, V. S., (1983), *J. Am. Ceram. Soc.*, 66, 260.

Heuer, A. H., and Rühle, M., (1984), *Science and Technology of Zirconia II, Advances
in*
Ceramics Vol.12, Edited by N. Claussen, M. Ruhle and A. Heuer. The Amercan
ceramics Society, pp 1-13.

Hillert, M., (1991), *J. Am. Ceram. Soc.*, 74, 2005.

Höchli, V. T., Knor, K., and Loidl, A., (1990), *Adv. Phys.*, 39, 405.

Howard, C.J., Hill, R.J. and Reichert, B.E., (1988), *Acta Cryst.*, B44, 116.

Hudson, B., and Moseley, P. T., (1976), *J. Solid State Chem.*, 19, 383.

Hull, S., Farley, T. W. D., Hackett, M. A., Hayes, W., Osborn, R., Andersen, N. H.,
Clausen, K., Hutchings, M. T., and Stirling, W. G., (1988), *Solid State Ionics*,
28-30, 488.

Ingel R. P. and Lewis III, D., (1988), *J. Am. Ceram. Soc.* 71, 265.

Ingram, M. D., MacKenzie, M. A., Muller, W., and Torge, M., (1988), *Solid State Ionics*,
28-30, 677.

Kauzmann, W., (1948), *Chem. Rev.*, 43, 219.

Kandil, H. M., Greiner, J. D. and Smith, J. F., (1984), *J. Am. Ceram. Soc.*, 67, 341.

Kirkpatrick, T. R. and Wolynes, P. G., (1987), *Phys. Rev.*, B33, 8552.

Kirkpatrick, T. R., Thirumalai, D., and Wolynes, P. G., (1989), *Phys. Rev.*, A40, 1045.

Kirkpatrick, T. R., Thirumalai, D., (1988), *Phys. Rev.*, B37, 5342.

Kirkpatrick, T. R., Thirumalai, D., (1988), *Phys. Rev.*, A37, 4439.

Kivelson, D., Kivelson, S. A. and Zhao, X., (1995), *Physica A*, 219, 27.

Klein, M. W., Fischer, B., Anderson, A. C. and Anthony, P. J., (1978), *Phys. Rev.B*, 18,
5887.

Klug, H. P., and Alexander, L. E., (1974), X-ray Diffraction Procedures for
Polycrystalline and Amorphous Materials, 2nd Ed., Wiley-Interscience, New York.

Knorr, K., and Loidl, A., (1985), *Phys. Rev.*, B31, 5387.

Lawless W. N., (1980), *Phys. Rev. B*, 22, 3122.

Lefevre, J., (1963), *Ann. Chim.*, 8, 135.

Leutheusser, E., (1984), *J. Phys. A*, 29, 2765.

Li, P., Chen, I.W., and Penner-Hahn, J.E., (1993a), *Phys. Rev. B*, 48, 10063.

Li, P., Chen, I.W., and Penner-Hahn, J.E., (1993b), *Phys. Rev. B*, 48, 10074.

Li, P., Chen, I.W., and Penner-Hahn, J.E., (1993c), *Phys. Rev. B*, 48, 10082.

Li, X. Y. and Hafskjold, B., (1995), *J. Phys.: Condens. Matter*, 7, 1255.

Lin, M., and Sellar, J. R., (1994), *Micron*, 25, 505.

Loidl, A., Schrader, T., Knorr, K., Bohmer, R., Mertz, B., McIntyre, G. J., Vogt, T., Mutka, H., Mullner, M., Jex, H., and Haussuhl, S., (1989), *Z. Phys. B-Condensed Matter*, 75, 81.

Lovesey, S. W., (1984), *Theory of Neutron Scattering from Condensed Matter*, Clarendon Press, Oxford.

Manning, P.S., Sirman, J. D., DeSouza, R.A., and Kilner, J.A., (1997), *Solid State Ionics*, 100, 1.

Martin, U., Boysen, H., and Frey, F., (1993), *Acta Cryst.*, B49 , 403.

Marxreiter, H., Boysen, H., Frey, F. and Schulz, H., (1990), *Mat. Res. Bull.*, 25, 435.

McClellan, K. J., Xiao, S. Q., Lagerlof, K. P. D., and Heuer, A. H., (1994), *Phil. Mag.* A70, 185.

Michel, D., (1973), *Mater. Res. Bull.*, 8, 943.

Miida, R., Tanaka, M., Arashi, H. and Ishigame, M., (1994), *J. Appl. Cryst.*, 27 , 67.

Morinaga, M., Cohen, J. B., and Faber, J., (1979), *Acta Cryst.*, A35 , 789.

Morinaga, M., Cohen, J. B., and Faber, J., (1980), *Acta Cryst.*, A36 , 520.

Morscher, G. N., Pirouz, P., and Heuer, A. H., (1991), *J. Am. Ceram. Soc.*, 74, 491.

Neder, R. B., Frey, F., and Schulz, H., (1990), *Acta Cryst.*, A46 , 799.

Negita, K. (1989), *Acta Metall.*, 37, 313.

Nowick, A. S., and Heller, W. R., (1963), *Advances in Physics*, 12, 251.

Osborn, R., Andersen, N. H., Clausen, K., Hackett, M. A., Hayes, W., Hutchings, M. T., and MacDonald, J. E., (1986), *Mater. Sci. Forum*, 7, 55.

Ozawa, M., and Hasegawa, H., (1993), *J. Mater. Sci. Letts.*, 12, 1625.

Patkowski, A., Fischer, E. W., Glaser, H., Meier, G., Nilgens, H., and Steffen, W., (1993), *Prog. Colloid Polym. Sci.*, 91, 35.

Pauling, L., (1960), *Nature of the Chemical Bond*, 3d ed. Cornell University Press, Ithaca, N. Y.

Pascual, C., and Duran, P., (1983), *J. Am. Ceram. Soc.*, 66, 23.

Pfeuty, P. and Toulouse, G., (1975), *Introduction to the Renormalization Group and to Critical Phenomena*, Wiley (London).

Proffen, TH., Neder, R. B., Frey, F., Keen, D. A., and Zeyen, C. M. E., (1993), *Acta Cryst.*, B49, 605.

Proffen, TH., Neder, R. B. and Frey, F., (1996a), *Acta Cryst.*, B52, 59.

Proffen, TH., Neder, R. B. and Frey, F., (1996b), *J. Solid State Chem.*, 126, 33.

Rossell, H. J., (1984), *Science and Technology of Zirconia II. Advances in Ceramics Vol.12*, Edited by N. Claussen, M. Rühle and A. Heuer, The Amercan Ceramics Society, Inc., Westerville, OH., pp46-65.

Rossell, H. J., Sellar, J. R., and Wilson, I. J., (1991), *Acta Cryst.*, B47, 862.

Rowe, J. M., Rush, J. J., Hinks, D. G. and Susman, S., (1979), *Phys. Rev. Lett.*, 43, 1158.

Ruh, R., Garrett, H. J., (1967), *J. Am. Ceram. Soc.*, 50, 257.

Ruh, R., Garrett, H. J., Domagala, R. F., and Patel, V. A., (1977), *J. Am. Ceram. Soc.*, 60, 399.

Ruh, R., Mazdiyasni, K. S., Valentine, P. G., and Bielstein, H. O., (1984), *J. Am. Ceram. Soc.*, 67, C-190.

Rühle, M., Claussen, N. and Heuer, A.H., (1984), *Science and Technology of Zirconia II. Advances in Ceramics* Vol.12, Edited by N. Claussen, M. Rühle and A. Heuer, The Amercan Ceramics Society, Inc., Westerville, OH., pp352-370.

Sakka, S., and MacKenzie, J. D., (1971), *J. Non-Cryst. Solids*, 6, 145.

Sakuma, T., Yoshizawa, Y. I., and Suto, H., (1985), *J. Mater. Sci. Lett.*, 4, 29.

Sakuma, T., Suto, H., (1986), *J. Mater. Sci.*, 21, 4359.

Scott, H. G., (1975), *J. Mater. Sci.*, 10, 1527.

Scott, H. G., (1977), *Acta Cryst.*, B33, 281.

Shannon, R. D., and Prewitt, C. T., (1969), *Acta Cryst.*, B25, 925.

Smith, D. K., and Newkirk, H. W., (1965), *Acta Cryst.*, 18, 983.

Solier, J. D., Cachadina, I., and Dominguez-Rodriguez, A., (1993), *Phys. Rev. B*, 48, 2704.

Spiridonov, F. M., Popova, L. N., and Popil'skii, R. Y., (1970), *J. Solid State Chem.*, 2, 430.

Steele, D., and Fender, B. E. F., (1974), *J. Phys. C*, 7, 1.

Stillinger, F. H., (1988), *J. Chem. Phys.*, 89, 6461.

Stubican, V. S. and Ray, S. P., (1977), *J. Am. Ceram. Soc.*, 60, 534.

Stubican, V. S., Hink, R. C., and Ray, S. P., (1978), *J. Am. Ceram. Soc.*, 61, 17.

Stubican, V. S., (1988), *Science and Technology of Zirconia III. Advances in Ceramics Vol.24.* Edited by S. Somiya, N. Yamamoto and H. Yanagida, The Amercan ceramics Society, Inc., Westerville, OH., pp71-81.

Suzuki, S., Tanaka, M., and Ishigame, M., (1985), *J. Appl. Phys.*, 24, 401.

Suzuki, S., Tanaka, M., and Ishigame, M., (1987), *J. Phys. C*, 20, 2963.

Teufer, D., (1962), *Acta Cryst.*, 15, 1187.

Thornber, M. R., Bevan, D. J., and Graham, J., (1968), *Acta Cryst.*, B24, 1183.

Thornber, M. R., Bevan, D. J., and Summerville, E., (1970), *J. Solid State Chem.*, 1, 545.

Tien, T. Y., and Subbarao, E. C., (1963), *J. Chem. Phys.*, 39, 1041.

Toulouse, G., (1977), *Comm. on Phys.*, 2, 115.

Tuller, M. H., Dexpert-Ghys, J., and Lagarde, P., (1987), *J. Solid State Chem.*, 69, 153.

Vollmayr, H., Kree, R., and Zippelius, A., (1991), *Phys. Rev.*, F44, 12238.

Walker, F. J. and Anderson, A. C., (1984), *Phys. Rev. B*, 29, 5881.

Weiberry, T. R., and Butler, B. D., (1995), *Chem Rev.*, 95, 2369.

Welberry, T. R., Butler, B. D., Thompson, J. G., and Withers, R. L., (1993), *J. Solid State Chem.*, <u>106</u>, 461.

Welberry, T. R., Withers, R. L., Thompson, J. G., and Butler, B. D., (1992), *J. Solid State*
Chem., <u>100</u>, 71.

Welberry, T. R., Withers, R. L., and Mayo, S. C., (1995), *J. Solid State Chem.*, <u>115</u>, 43.

Wilson, A. J. C., (1963), *Mathematical Theory of X-ray Powder Diffraction*, Philips
Technical Library.

Withers, R. L., Thompson, J. G., and Barlow, P. J., (1991), *J. Solid State Chem.*, <u>94</u>, 89.

Withers, R. L., Thompson, J. G., and Barry, J.C., (1992), *J. Computer-Assisted Microscopy.*, <u>4</u>, 315.

Withers, R.L., Proffen, TH., and Welberry, T.R., (1999), *Philos. Mag.*, <u>A78</u>, 753

Yashima, M., Sasaki, Y., Kakihana, M., Yamaguchi, Y., Arashi, H., and Yoshimupa, M., (1994), *Acta Cryst.*, <u>B50</u>, 563.

Yashima, M., Ishizawa, N., and Yoshimura, M., (1993), *J. Am. Ceram. Soc.*, <u>76</u>, 641.

Yashima, M., Kakihana, M., and Yoshimura, M., (1996), *Solid State Ionics*, <u>86-88</u>, 1131.

Yashima, M., Ohtake, K., Arashi, H., Kakihana, M., and Yoshimura, M., (1993), *J. Appl. Phys.*, <u>74</u>, 7603.

Yu, C.C., (1992), *Phys. Rev. Lett.*, <u>69</u>, 2787.

Zhou, Y., Lei, T. C. and Sakuma, T., (1991), *J. Am. Ceram. Soc.*, 74, 633.

APPENDIX: RESPONSES TO REFEREE'S QUESTIONS

QUESTION 1

What is the source of the narrow extra powder diffraction peak observed near 13.7 degrees at an angle slightly higher than the Bragg 111 reflection under Molybdenum X-radiation, as seen in Figures 6.5 and 6.6? Why is it so narrow? Why does it vanish at 1000°C? Why is it not detected in diffraction patterns from 12-YSZ taken using electrons, neutrons or Copper X-radiation?

QUESTION 2

High-temperature X-ray diffraction is a difficult technique. Is the behaviour displayed in Figures 6.5 and 6.6 of the thesis reproducible?

Answer to - QUESTION 1

Based on the Allpress – Rossell model, a consistent picture of the X – ray diffraction from 12 – YSZ and how it differs from electron and neutron diffraction can be developed.

In brief , the solution to the difficulty regarding the apparently anomalous appearance of the narrow extra peak above the 111 reflection is essentially this: that while the atomic scattering factors for Zr (zirconium) and Y(yttrium) are very similar for the cases of electrons , neutrons and Cu ka1 X – radiation , the anomalous absorption of Mo ka1 X – radiation Bragg – scattered from yttrium atoms yields a very low value for the yttrium contribution to the f.c.c. – type Bragg reflections (111, 220 etc). The "lost" intensity is radiated isotropically as fluorescence radiation. In this (Mo) case, the absorption remedies the former occlusion of the sharper intensity contribution diffracted from large (~ 1000 Å – sized) Fischer – type domains by diffuse intensity at a slightly lower angle due to small (~ 15 Å) Allpress – Rossell microdomains.These larger domains were described by Fischer (1993) and by Patkowski et al (1993) and are believed to control the ultraslow relaxation of free volume in fragile glasses. These remarks are explained more fully below.

Throughout the thesis it has been emphasized that the microstructure of stabilized zirconia is based on the Allpress – Rossell model of coherently – intergrown superlattice microdomains in a matrix of pure distorted zirconia (ZrO_2). The model was initially suggested for Ca – CSZ , but a similar pattern emerges for other cubic stabilized varieties eg YSZ. The thesis reports a microdomain size of for YSZ of ~15 Å (Ch 7.5) , the same as that deduced by Goff et al (1999): These results were determined in both sets of experiments by reference to diffuse scatter near 1.4,1.4,1.8 etc. It has also been stressed that due to universality near critical points (Ch 8) , a six – state orientational glass would result at low temperature regardless of whether the local defect VKZ symmetry was of Type A , B or C and that at criticality it mattered little which analogue of the delta, gamma or beta phases played the role of the rotatable Allpress – Rossell microdomain species, since all were rhombohedral and the precise details of the phase assembly depend on thermomechanical history. On the basis of their extensive experiments Goff et al considered the delta phase to be the rotating species. Assuming for a moment that the delta phase is in fact the majority Allpress- Rossell microdomain constituent for 12 – YSZ (apart from pure ZrO_2) , the chief structural difference between the average fluorite subcell of delta and that of cubic zirconia is that its 111 planes are slightly further apart than those of pure ZrO_2 fluorite (the rhombohedral distortion). This means that its 111 powder X – ray line will be situated at a lower angle than that of the ZrO_2 matrix, while the other Bragg lines will overlap to a good approximation. Thus the higher 2 – theta line is attributable to the ZrO_2 matrix alone, which percolates throughout the 12 – YSZ grains. Since the delta phase is approximately 50:50 Zr:Y and occupies roughly one – half the cation sublattice , we assume that for radiation which does not distinguish between Zr and Y atoms (eg Cu Ka1), the total scattered intensity into Bragg

reflections is roughly equally shared between the upper and lower 111 powder lines. We also assume that the "tetragonal without tetragonality" oxygen ions contribute little scattered intensity into the powder lines compared to the much heavier metal ions.

Examining Fig 6.6 of the thesis, which shows the variation of the 111 reflection intensity of the 12YSZ sample under Mo radiation as a function of temperature, it seems clear that the broadened Bragg linewidth of the lower peak is due principally to the correlated delta microdomains, but also possibly contaminated by other fluorite – like phases with 111 reflections (baddeleyite and Y_2O_3 have been suggested, depending on specimen preparation eg Ishizawa et al Acta.Cryst, 1999, B55, 726).The lower (inner) peak is approximately as wide as the difference between its reflecting position and that of the narrower, outer peak, and would tend to occlude this higher-angle peak were it not for the operation of the anomalous absorption which reduces the total scattering of Mo radiation from the lower peak, roughly half of whose intensity is due to yttrium. The higher peak, as we have seen, contains no scattering contribution from yttrium atoms. For Cu radiation, though the room- temperature peak shape may be dependent to some extent on the cooling regime of the as-received large single crystals and their subsequent grinding to powder form, the diffraction patterns taken as a function of temperature reveal some small asymmetries unobscured by the truncation of the peak tops (Fig 6.3). More significant is the approximate halving of intensity above 1000°C corresponding to the uncoupling of the antiferroelastic "tees" and the consequent softening of the cubic matrix. This is near our T_m (the "glass melting" temperature) and signals the onset of high ionic conductivity in 12-YSZ. Thus the contribution to the closely-spaced and mutually overlapping 111 reflections from the partly melted ZrO_2 matrix is now approximately zero, and above 1000°C the formerly combined intensity is now roughly halved, as noted. This halving occurs for all three reflections and in the same temperature range(Fig 6.3).

To judge from the neutron scatter near 1.4,1.4,1.8 etc. the size of the rotating microdomains in 12YSZ is about 15 Å and that of the correlation length of the cations about 150 Å on average in the supercooling range. As A/Professor Drennan states, the width of the outer 111 reflection appears to be considerably narrow, indicating a correlation length of the order of several hundreds of Angstroms. The solution to this difficulty lies in the noisy free-volume fluctuations of the order of a micron in size, which have been noticed in fragile glass-formers by Patkowski et al and others, and mentioned in Chapter 4 of the thesis. These reorganizations of the free volume are held to be due to the cooperative ordering of "clusters" in the glass former(Fischer, (1993). These clusters (sometimes called Fischer clusters) are poorly characterized so far in such low-molecular-weight glasses as 1,1-di(4'-methoxy-5'-methyl-phenyl)-cyclohexane (BMMPC), but because of the large amounts of data already gathered on zirconia over the last 30 years yet not fully interpreted, we can identify a case where the corresponding clusters may be found (and, we believe, have already been found).

The relevant experiments carried out by Patkowski et al (1993) were conducted using static light scattering to probe the correlation length of the BMMPC clusters. For the data presented, the glass transition temperature T_g and the glass melting temperature T_m of BMMPC can be shown to be respectively near room temperature (where the correlation

length would be large) and near 130°C (where the correlation length would be small), as shown in Fig.3 of Patkowski et al (1993).. In the temperature range they examined, it is clear that the correlation length is of the order of approximately 600Å. At a temperature near Tm (~130°C) little correlation would be detected. In a similar way, in Fig 6.6 of the thesis, where the two 111 peaks are relatively clearly distinguished, the outer peak (corresponding to inter-microdomain ZrO_2 matrix material where the conducting vacancies travel), corresponds to an average "particle size" of about 600 Å, a value very similar to the measurements of Patkowski et al (1993), and, more importantly, in good agreement with the estimates of Carter and Roth (1968) of order-disorder "syntactic zones" of size 600 Å, which they describe as an interlocking network of coherently intergrown phases with differing ionic conductivities. This is a clear early description of the Allpress-Rossell model for cubic zirconia, now organized into regions of size approximately 600 Å. Carter and Roth were able to detect these "zones" in electron micrographs because of the different scattering power between the matrix and the calcium-rich microdomains.

To repeat, because of the anomalous absorption of Mo $K\alpha 1$ radiation by yttrium atoms, the x-ray diffraction of Mo radiation is able to distinguish the Fischer-type domains in yttria-stabilized zirconia while electrons, neutrons and Cu X-ray radiation are not. The Fischer-type domains are of size ~600 to 1000 Å, and give rise to sharp reflections under Mo $K\alpha 1$ radiation.

Answer to - QUESTION 2

The Mo radiation results are repeatable and genuine.

The justification is as follows:

A) The experiment was repeated and a similar effect appeared. The enclosed plots 1, 2 were taken on separate runs and it can be seen that the peak splitting appears on both plots although the peak shapes and 2θ positions are slightly different.

B) They are not likely to be due to contamination of the high temperature stage, such as the platinum sample holder and alumina shelter, since same experimental set-up was used with Cu X-radiation and no extra effects appeared in that case.

C) They are not due to $K_{\alpha 2}$ radiation. From $2d\sin\theta = \lambda$ we can have $\delta(2\theta) = \dfrac{\delta\lambda}{d\cos\theta} \cdot \dfrac{180}{\pi}$. For Mo radiation, $\lambda_{\alpha 1}$ =0.70926Å, $\lambda_{\alpha 2}$ =0.71354 Å, which gives $\delta\lambda = 0.00428$Å. Take d_{111}=2.9553Å and $2\theta = 13.81°$ based on our x-ray

diffraction results (the accuracy of d_{111} and 2θ is not important to our argument); $\lambda_{\alpha 1}$ and $\lambda_{\alpha 2}$ will cause 111 peak splitting of 0.084°. On plot 1, there are 3 peaks/peak clusters corresponding to 13.70°, 13.81°, and 13.89°. The 2θ difference between the two outer peaks is 0.19°, which is much greater than 0.084°. Using Trace software, the $K_{\alpha 2}$ contribution was stripped off and the treated trace is presented in plot 3.

D) They are not due to K_β radiation. Using the same approach as in point C, e.g., given $\lambda_{\beta 1}$ =0.632253 Å, the peak shift in 2θ caused by $\lambda_{\beta 1}$ is 1.59°, which is out of the range.